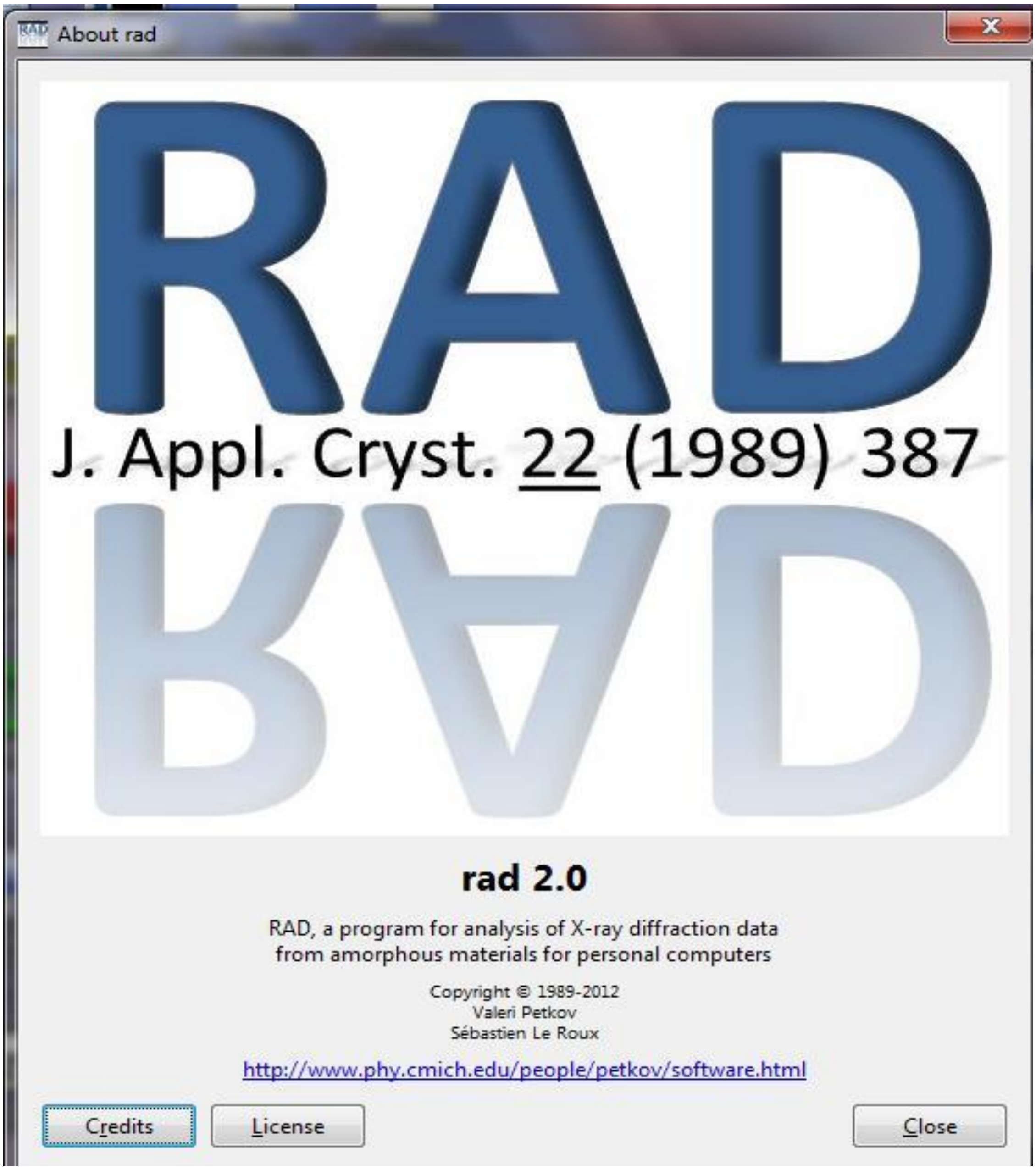

J. Appl. Cryst. 22 (1989) 387

rad 2.0

RAD, a program for analysis of X-ray diffraction data
from amorphous materials for personal computers

Copyright © 1989-2012
Valeri Petkov
Sébastien Le Roux

http://www.phy.cmich.edu/people/petkov/software.html

USER's Manual

written by Valeri Petkov

E-mail: petko1vg@cmich.edu
url: http://www.phy.cmich.edu/people/petkov/

Document created: April 2013

Disclaimer:

This version of RAD (hereafter called RAD_2 for convenience) is distributed on an "as is" basis without any warranty either expressed or implied as to its performance, quality or fitness for any particular purpose. The entire risk of running RAD_2 is with the user. In no event shall RAD_2 authors or anyone who has been involved in the creation and production of RAD_2 software be liable for indirect, special or consequential damages resulting from the use of it. Note, RAD_2 is copyrighted and all rights are reserved by the authors. Users of RAD_2 are allowed only to read the program from its medium into memory of a computer solely for the purposes of executing the program. Copying and duplicating (except for purpose of backup), selling or otherwise distributing RAD_2 without the prior written consent of the authors is not allowed. Upon request, academia users may obtain from the authors a free copy of RAD_2. That free copy should be used for scientific purposes only. Industrial users may be required to pay a RAD_2 license fee. If you do not agree with these terms, do not install and use RAD_2.

Acknowledging RAD:

Any publication and/or presentation of results obtained using RAD_2 should make clear that a version of the original RAD program has been used, and contain the following reference:

V. Petkov, "RAD, a program for analysis of X-ray diffraction data from amorphous materials for personal computers" *J. Appl. Crystallogr.* **22** (1989) 387-89.

(a copy of this paper is attached at the end of this User Manual).

Installing RAD:

RAD-GTK+ is a cross-platform program running under Linux, MacOSX and Windows(7) environments.

A license is required to run RAD. The license is linked to a piece of hardware on the computer RAD will be used, so the User needs to provide the RAD team with some rather particular hardware information. Based on this information a personal, custom made binary version of the RAD software will be prepared for the User. To help the USER provide this information a tool called ‘p-rad’ is delivered together with RAD (you will find it in a sub-folder “p-rad” in the “RAD” main folder created on your disk upon RAD_2 installation). We suggest to run this tool (note that you need to install GTK+ to run p-rad) to test your hardware so that you could send us the right hardware information. Below is how p-RAD works:

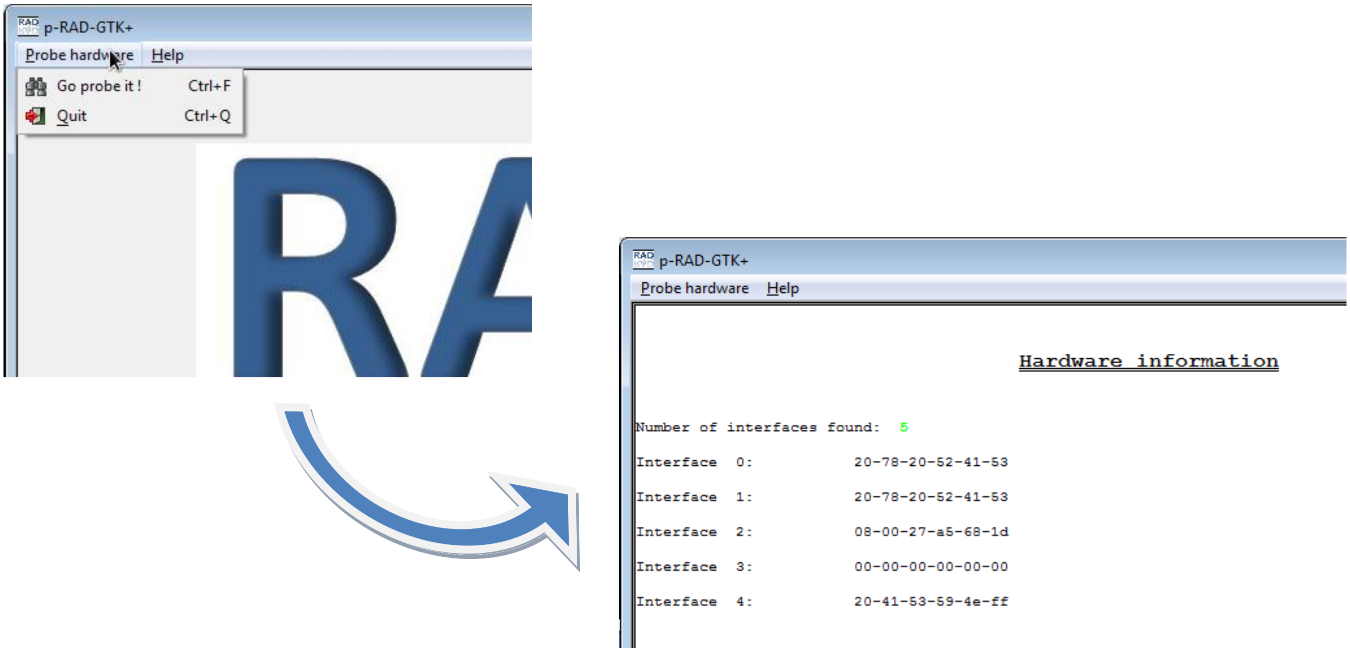

```
Hardware information

Number of interfaces found:  5

Interface  0:           20-78-20-52-41-53

Interface  1:           20-78-20-52-41-53

Interface  2:           08-00-27-a5-68-1d

Interface  3:           00-00-00-00-00-00

Interface  4:           20-41-53-59-4e-ff
```

To obtain your own personal copy of RAD simply send us a copy of the output of p-rad (text) file.

Linux Users:

Using the standard package installer (yum, apt …) of your Linux distribution you need to install the RAD package, ‘.deb’ or ‘.rpm’, depending on whether your distribution is ‘Debian’ (Debian, Ubuntu) or ‘Red-Hat’ (Red-Hat, Fedora, Mandriva, Suse …) based.

The installer will automatically find and install, if required, the appropriate dependencies to run RAD.

MacOSX Users:

Nothing to be done here, RAD is distributed in a bundled application that contains everything you need to run it !

WINDOWS Users:

Before installing RAD_2 always Un-install older versions of RAD if you have such on your computer. To do it go to “All Programs”, find Rad-Gtk+, select the Un-install option from the drop-down menu and click it as shown below.

Alternatively you can Un-install RAD in the Windows control panel using the Programs section.

Then simply use the provided by us RAD-GTK+ installer. For a first time installation remember to install all dependencies, such as the GTK+ and the XML2 libraries.

1. What is RAD ?

RAD takes x-ray diffraction (XRD) data and reduces it to an atomic pair/radial distribution function (PDF/RDF). It has been used by the author (VP) and many research groups all over the world for more than 20 years. It is based on rigorous XRD data reduction procedures established back when XRD was born. Yet RAD is under constant modification following the on-going development of XRD data collection procedures and instrumentation. **The author of this Manual thanks Sébastien Le Roux for the great job done in developing a user friendly (GTK-based) interface to RAD.**

2. What is GTK+?

GTK+ is a toolkit for creating graphical User interfaces. GTK+ is written in C but has bindings to many other popular programming languages such as C++, Python and others.

3. What is XRD and atomic PDF/RDF analysis ?

XRD is used to determine the atomic-scale structure of materials. The technique is based on the fact that the wavelength of x-rays is comparable in size to the distances between atoms in condensed matter. So when a material exhibiting a long-range (i.e. at least μm-range) periodic atomic order, such as a single crystal or polycrystalline powder, is irradiated with x-rays it acts as an extended periodic grating producing a diffraction pattern showing numerous sharp spots, called Bragg diffraction peaks. By measuring and analyzing the positions and intensities of the Bragg peaks it is possible to determine the spatial characteristics of the grating – i.e. to determine the three-dimensional (3D) atomic arrangement in the crystalline materials. This is the essence of the so-called "crystal structure" determination by XRD [1]. Over the years the technique has been perfected and applied successfully to a variety of crystalline materials – from simple metals to complex proteins. X-ray diffraction can also be applied to study the structure of materials where atoms are ordered only at short (1-2 nm range) to intermediate (tens of nm)-range distances such as liquids, glasses, nanosized powders, polymers, composites etc. When irradiated with x-rays these materials act as quite imperfect gratings producing XRD patterns that are very diffuse in nature. This renders traditional (Bragg-peaks based) crystallography very difficult to apply. A combination of higher-energy x-ray diffraction and atomic PDF/RDF data analysis [2] has proven to be very useful in such cases.

The frequently used reduced atomic PDF/RDF, G(r), gives the number of atoms in a spherical shell of unit thickness at a distance r from a reference atom as follows [2,3]:

$$G(r) = 4\pi r \rho_o \, [\rho(r)/\rho_o - 1] \qquad (1)$$

where $\rho(r)$ and ρ_o are the local and average atomic number densities, respectively and r is the radial distance. As defined, **the PDF/RDF G(r)** is a one-dimensional function that **oscillates around zero** showing positive peaks at distances separating pairs of atoms, i.e. where the local atomic density exceeds the average one. The valleys in the PDF/RDF G(r) correspond to real space vectors not having atoms at either of their ends. With this respect the atomic PDF resembles the so-called Patterson function that is widely used in traditional x-ray crystallography [1]. However, while the Paterson function peaks at interatomic distances within the unit cell of a crystal, the atomic PDF/RDF reflects all interatomic distances occurring in a material. This is a great advantage when studying materials whose structure is difficult to be described in terms of extended periodic lattices. The PDF G(r) is the Fourier transform of the experimentally observable total structure function, S(Q), i.e.

$$G(r) = (2/\pi) \int_{q=o}^{q_{\max}} q[S(q)-1]\sin(qr)\,dq, \qquad (2)$$

where q is the magnitude of the wave vector ($q=4\pi\sin\theta/\lambda$), 2θ is the angle between the incoming and outgoing x-rays and λ is the wavelength of the x-rays used. X-ray diffraction usually employs the so-called Faber-Ziman type structure function, S(q), related to **only (!) the coherent** part of the diffraction pattern, $I^{coh.}(q)$, as follows [2,3]:

$$S(q) = 1 + \left[I^{coh.}(q) - \sum c_i \left| f_i \ (q) \right|^2 \right] / \left| \sum c_i f_i(q) \right|^2, \qquad (3)$$

where c_i and $f_i(q)$ are the atomic concentration and x-ray scattering factor respectively for the atomic species of type i. Note $f(q)$ is a function both of x-rays energy (E) and wave vector q, i.e. $f(q) = f_o(q) + f'(q, E) + if''(q, E)$ where f' and f'' are the so-called anomalous dispersion correction terms [1,2]. Also note**, as defined, S(q) oscillates around one while q[S(q)-1] – around zero.** It should also be noted that for a material comprising *n* atomic species a single diffraction experiment yields a PDF/RDF that is a weighted sum of *n(n+1)/2* partial PDFs/RDFs, $G(r_{ij})$, i.e.

$$G(r) = \sum_{i,j} w_{ij} G_{ij}(r) \qquad (4).$$

Here w_{ij} are weighting factors depending on the concentration and scattering power of the atomic species as follows:

$$w_{ij} = c_i c_j f_i(q) f_j(q) / [\sum c_i f_i(q)]^2 \qquad (5).$$

For practical purposes w_{ij}'s are often evaluated for q=0 [2,3]. For User's convenience a review article from the Wiley's book "Characterization of Materials' devoted to atomic PDF/RDF analysis is attached to this Manual.

4. How XRD data suitable for atomic PDF/RDF analysis are collected ?

Source of radiation: The Fourier transformation (*see Eq. 2*) should not be terminated too early i.e. q_{max} should be at least 15-20 Å^{-1}. Diffraction data at such high wave vectors can be obtained using x-rays of a shorter wavelength, i.e. of higher energy. X-rays of higher (than usual) energy can be delivered by synchrotron sources. In house XRD instruments operated with sealed x-ray tubes/rotating anodes with Mo (energy ~ 17 keV) or Ag (energy ~ 22 keV) anodes/targets can also be used for atomic PDF/RDF studies. Note the energy of Cu Ka radiation is only about 8 keV and, hence, q_{max} may not get higher than 7-8 Å^{-1} or so. Therefore, **Cu Ka radiation is completely not suitable** for higher-energy XRD aimed at atomic PDF/RDF data analysis.

XRD data statistics and collection time: Whatever source of higher-energy x-rays is used the XRD data should be collected with a very good statistical accuracy. That may mean having at least 10,000 counts collected at any data point/diffraction angle [4]. To achieve it XRD data may need to be collected much longer than in the case of more traditional applications such as Rietveld analysis. Thus when a sealed x-ray tube source and a single point (e.g. scintillation) detector are employed the data collection may take tens of hours. More powerful sources of x-rays (rotating anode generators and synchrotrons) and/or large area detectors may reduce the XRD data collection time to minutes [5].

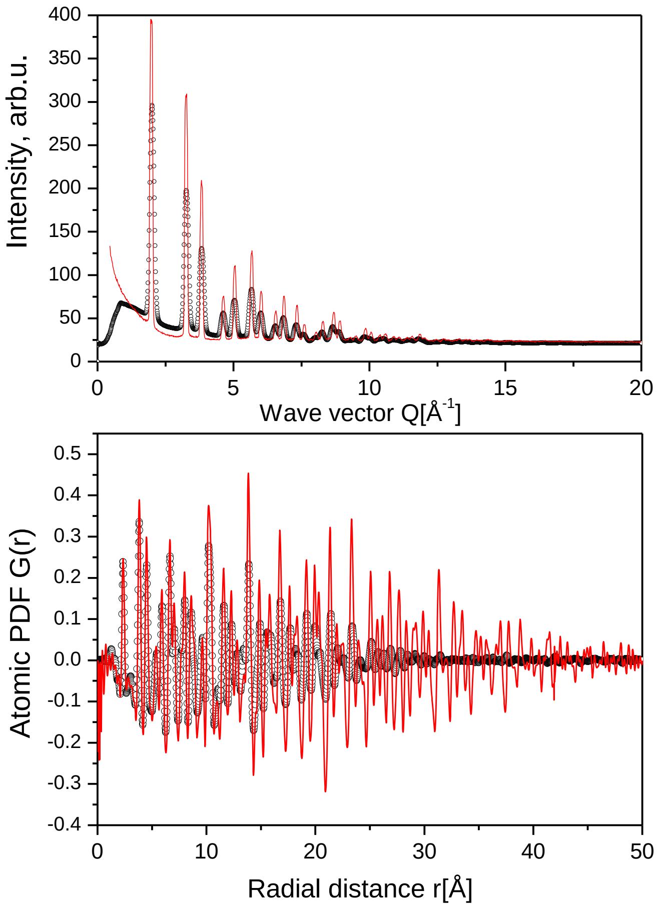

Figure 1. Experimental XRD patterns for Si polycrystalline powder collected with a point (solid line in red) and area Image Plate/mar345 (symbols) detectors while the rest of the experimental set-up has been kept unchanged. The corresponding atomic PDFs are shown in the lower part of the plot. Note that obtained from low-q resolution/image plate XRD data decays unphysically to zero at very short interatomic distances while that obtained from XRD data with better q-space resolution/point detector – does not.

Experimental set-up (q-space) resolution: In general, structure studies on poorly- or completely non-periodic materials do not require experimental set-ups of very high reciprocal (*q-space*) space resolution because of the inherently diffuse nature of the respective XRD patterns. However, the reciprocal space resolution of the experimental set up, including that of the detector, should not be too low either. As an example XRD patterns for polycrystalline Si (NIST powder standard) collected with two different types of detectors, a single point detector and a large area (Image Plate based mar345) detector are shown in Fig. 1. The lower resolution of the XRD data collected with a large area detector leads to an extra broadening of the peaks in the XRD pattern. This results in a loss of information in the higher-r region of the corresponding atomic PDF. This loss **may be critical or not** depending on the degree of periodicity/crystallinity of the material studied and of the goals of the particular PDF study.

Background scattering treatment: Air, sample holder etc. background-type scattering should be kept to a minimum since atomic PDFs are based on **only (!)** the coherent/elastic component of the XRD data (*see Eq. 3*)**. Remember: weaker background signal is much easier to correct for !**

Sample related but "unwanted"scatterting: X-rays are both scattered from and absorbed inside materials via various processes [1, 2]. The absorption of higher-energy x-rays is relatively low and usually does not pose much of a problem in the XRD data reduction process. The same is true for multiple scattering [2] of higher-energy x-rays. Inelastic (Compton) scattering, however, may be very strong, especially at high wave vectors [2]. If possible it should be eliminated from the experimental XRD data during data collection by using energy-sensitive detectors [6]. **Note the analytical procedures for computing Compton scattering and subtracting it** from experimental XRD data are, inevitably, based on various approximations and, therefore, **may or may not work** well for every material. Fluorescent scattering from the sample should also be kept to a minimum. This could be achieved either by using an energy-sensitive detector and/or by employing x-rays of energy below the absorption edge of the most strongly scattering atomic species in the material under study.

In summary, a successful atomic PDF/RDF study requires an XRD experiment done with a due care. Software like RAD can reduce virtually any XRD data set to an atomic PDF/RDF but whether this "PDF/RDF" is a physically meaningful representation of the atomic-scale structure of the material studied very much depends on the quality of experimental XRD data !

5. Using RAD_2 :

Click on the RAD_2 icon. The following 2 program windows will open (see below). One (labeled *RAD* in the upper left corner) is used to run/test RAD_2 in an "expert mode", display system/program error messages etc. (see below).

Usually this window has a limited usage and so may be “collapsed/minimized in size” (but definitely has to be kept active !) when RAD_2 is running.

The second window (labeled *RAD-Gtk* in the upper left corner, see below) is the RAD’s main actions control window. It too should be kept active while RAD_2 is running.

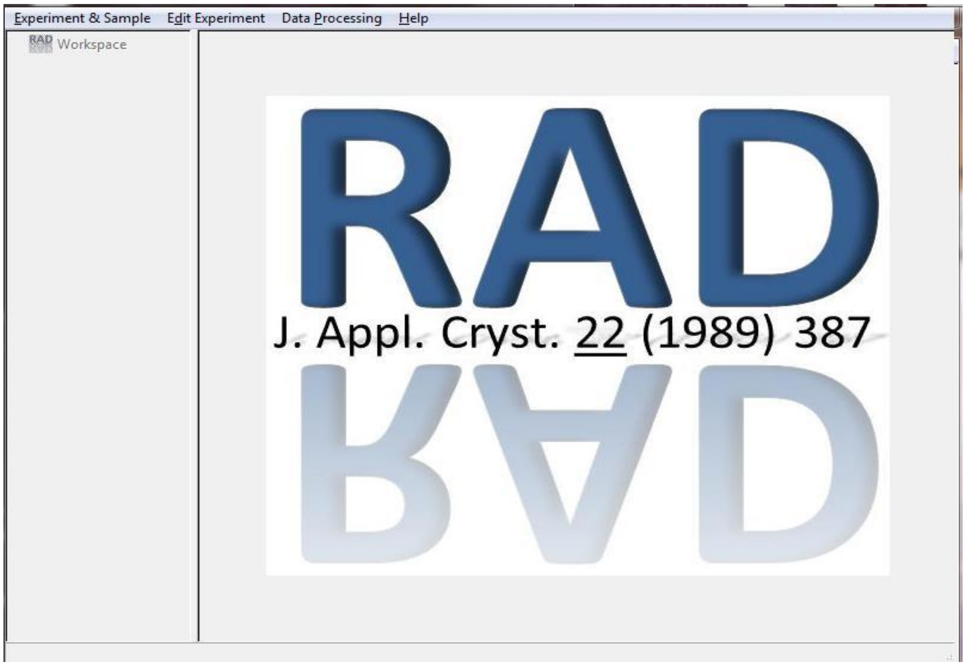

This window allows the user to get access to the following three actions/options (activated by clicking on them):

i) Entry/Input/Export/Save of RAD projects and workspaces:

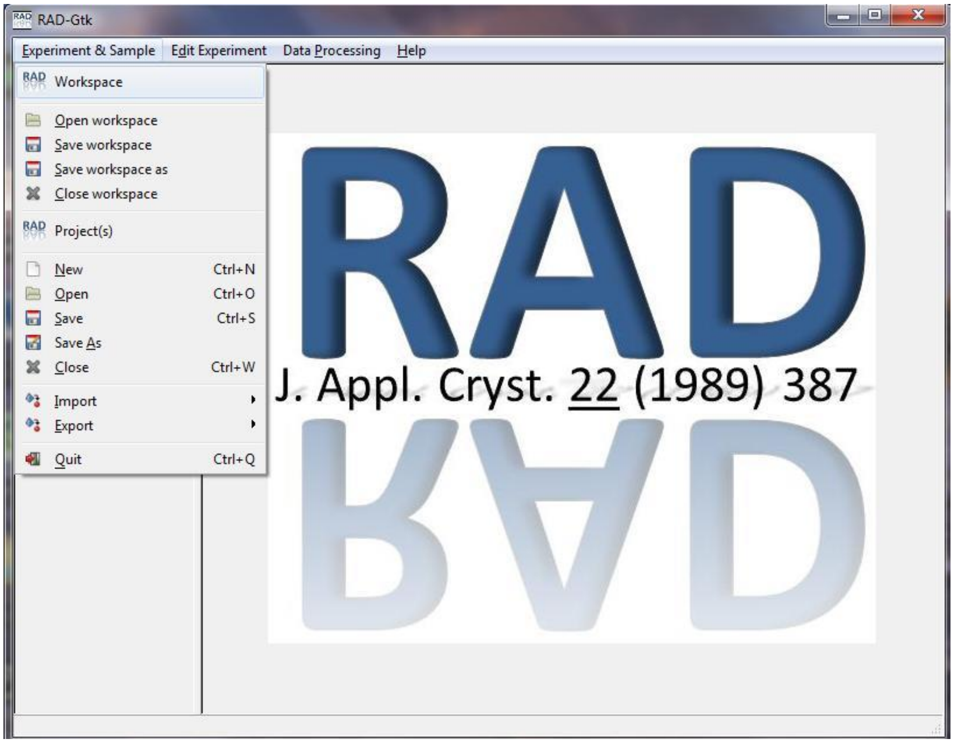

ii) Editing of XRD Experiment & Sample Info:

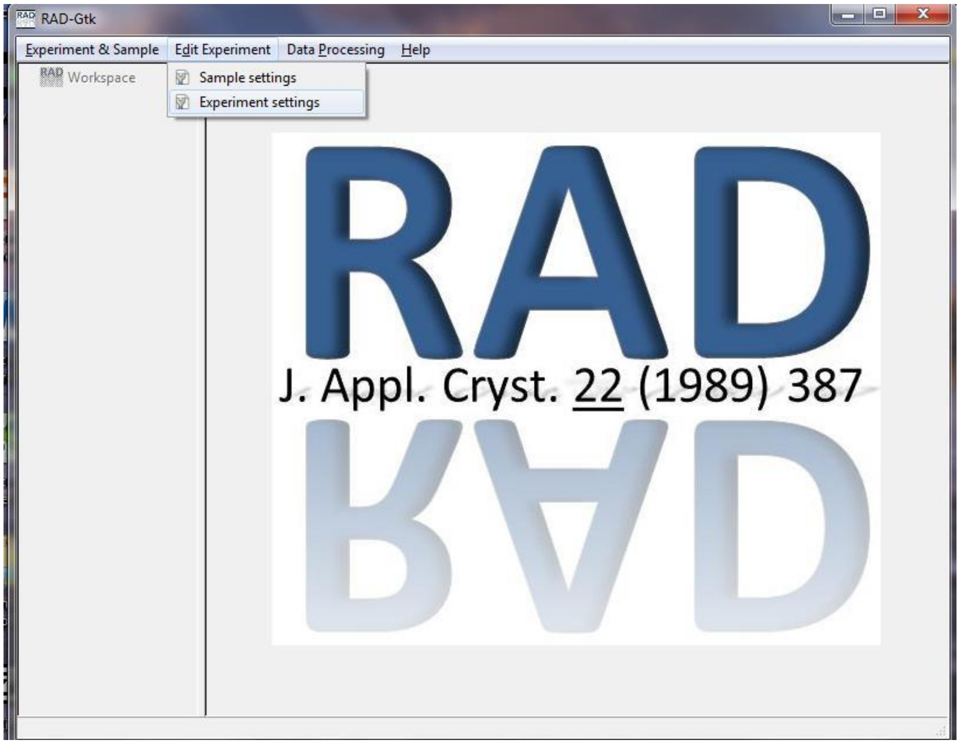

iii) XRD Data Processing into atomic PDFs:

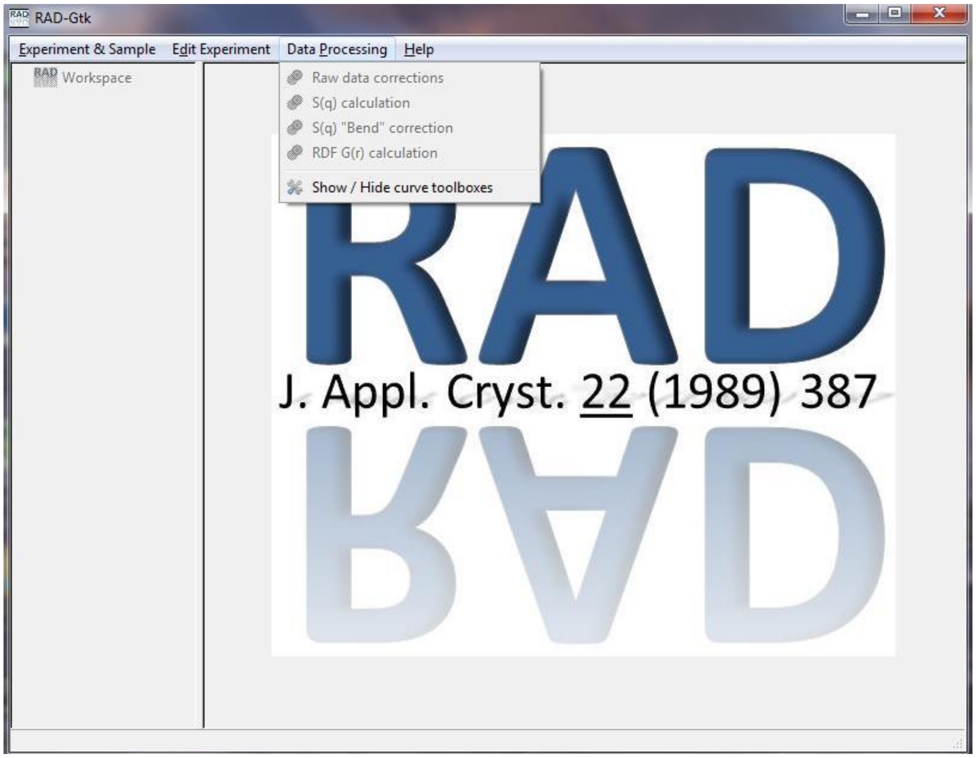

Below we explain each of these three options:

i) Entry/Input/Export/Save/Load of RAD projects and workspaces:

When activated this option allows the User to start a new, open an existing or save a current RAD_2 project or workspace. When the RAD_2 project is in text (“xml”) format it should be saved with an extension “rpf”. These text files/projects may be opened and viewed with any text editor. RAD_2 “rpf” files contain information about the studied sample and the experimental set-up that has been used to collect the XRD data. The information is needed to run the option *XRD Data Processing*. Information about the sample include: the number of distinct chemical species (up to 10), the atomic number, Z, of each of the species (from Z=1(H) to Z=98(Cf)), the species relative concentration, the anomalous dispersion corrections (f’ and f”) for that species, and the wavelength of the radiation used. An example of *Sample Description* entry is given below. **For User’s convenience all examples considered in this Manual are stored in a folder “Examples” upon RAD_2 installation.** The example features one of the first applications of RAD on in-house (Mo Ka) XRD data for Gd_4Al_3 metallic glass. Results from this study are published in: V. Petkov et al. "Radial distribution functions for RE$_4$Al$_3$ metallic glasses (RE=Pr, Gd, Tb, Dy)", *J. Non- Cryst. Sol*. 108 (1989) 75 (a copy of the paper is attached to this Manual).

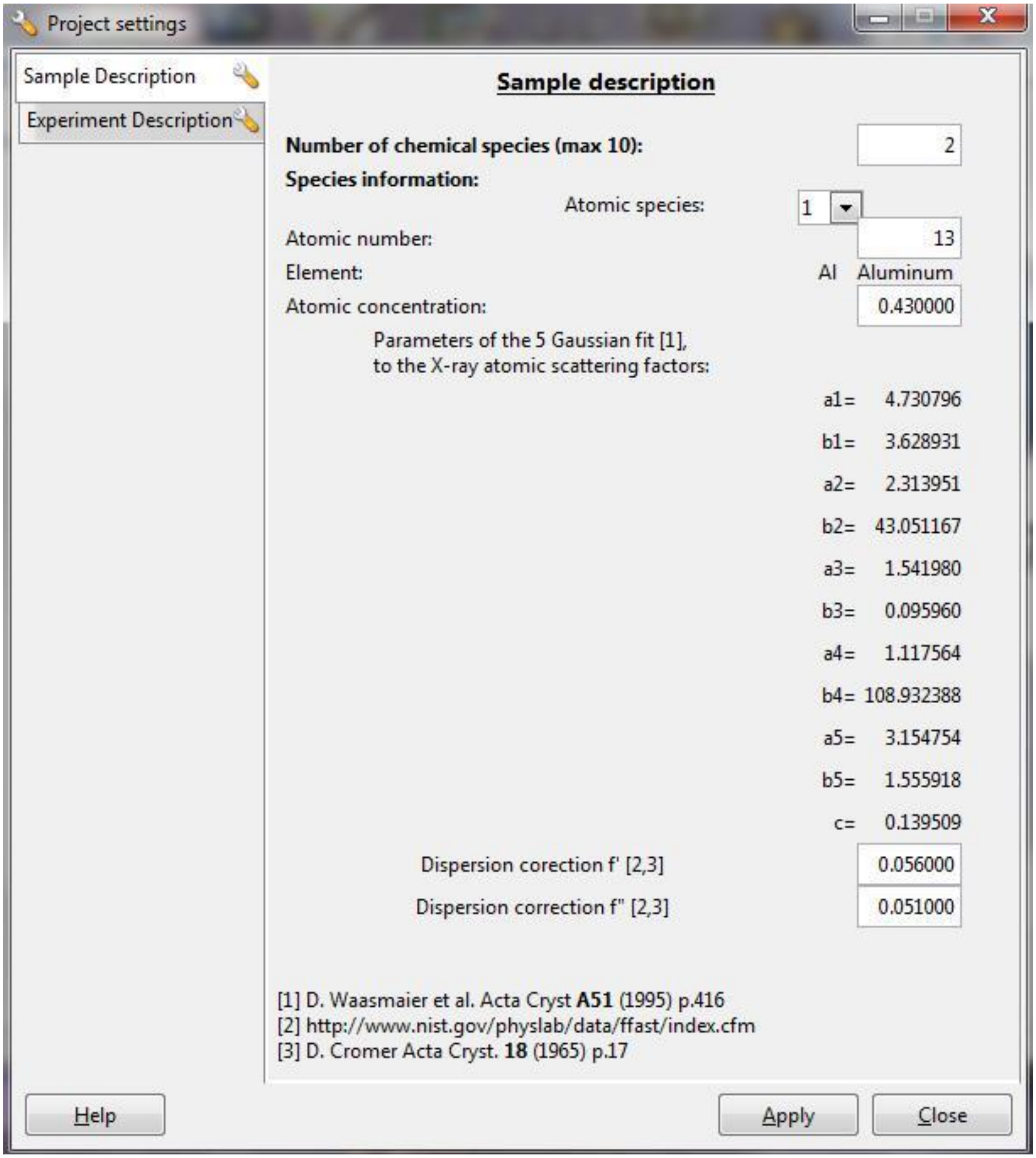

Sample description

Number of chemical species (max 10): 2

Species information:

Atomic species: 1

Atomic number: 13

Element: Al Aluminum

Atomic concentration: 0.430000

Parameters of the 5 Gaussian fit [1],
to the X-ray atomic scattering factors:

a1= 4.730796
b1= 3.628931
a2= 2.313951
b2= 43.051167
a3= 1.541980
b3= 0.095960
a4= 1.117564
b4= 108.932388
a5= 3.154754
b5= 1.555918
c= 0.139509

Dispersion corection f' [2,3] 0.056000

Dispersion correction f" [2,3] 0.051000

[1] D. Waasmaier et al. Acta Cryst **A51** (1995) p.416
[2] http://www.nist.gov/physlab/data/ffast/index.cfm
[3] D. Cromer Acta Cryst. **18** (1965) p.17

In this example (see above) we first enter the number of chemical species (**2** in this case) in the “Number of chemical species” data field (upper right corner; see above) and **hit Enter** ! This is the only time the user should hit the Enter key ! This tells RAD_2 to open a “drop down list” menu button (second line from the top in the example window shown above) that lists (consecutively) the chemical species in the sample studied. Then we enter the atomic number, Z, for species “**1**” – it is **13** for Al (see **Appendix 1**), and the atomic concentration of Al – 0.43. Note the chemical composition of the metallic glass from this example could be entered as: Gd_4Al_3, $Gd_{57}Al_{43}$, $Gd_{0.57}Al_{0.43}$ etc. Here we opt for the last chemical formula. The others would have been equally good. Users, however, should be aware that depending on the choice of the chemical formula unit the computed q[S(q)-1] and PDF/RDF G(r) would differ times a constant factor which scales with the total number of atoms in the respective chemical formula unit used [2,3]. **RAD_2 users: be consistent in your choices of the chemical formula unit for the sample you study! Stick to the same formula unit (e.g. $Gd_{0.57}Al_{0.43}$) when you use the respective PDF/RDF data to extract atomic coordination numbers and/or fit/compare experimental PDF/RDFs with structure models.**

In this example we/the User should also supply information about the dispersion correction terms to the x-ray scattering factor of Al (f’=0.056) and (f”=0.051) consistent with the respective, in our case Mo Ka, radiation used. Information for the dispersion correction terms f’ and f” may be obtained from the National Institute of Standards & Technology www site:

http://www.nist.gov/physlab/data/xray_gammaray.cfm

or from literature sources. For RAD_2 User’s convenience the f’ and f” values for Mo and Ag Ka radiation, as computed by D. Cromer, are given in **Appendix 2** of this Manual. Information about the atomic scattering factors $f_o(q)$ for atomic species with Z=1 to Z=98 comes with RAD_2 so the User should not worry about it. Here is the place to note that RAD_2 can handle XRD data sets from materials composed of **up to 10** atomic species with atomic numbers, **Z, from 1 to 98.** Selecting “*Atomic Species*” **2** from the drop down list allows the user to supply information about Gd, as exemplified below:

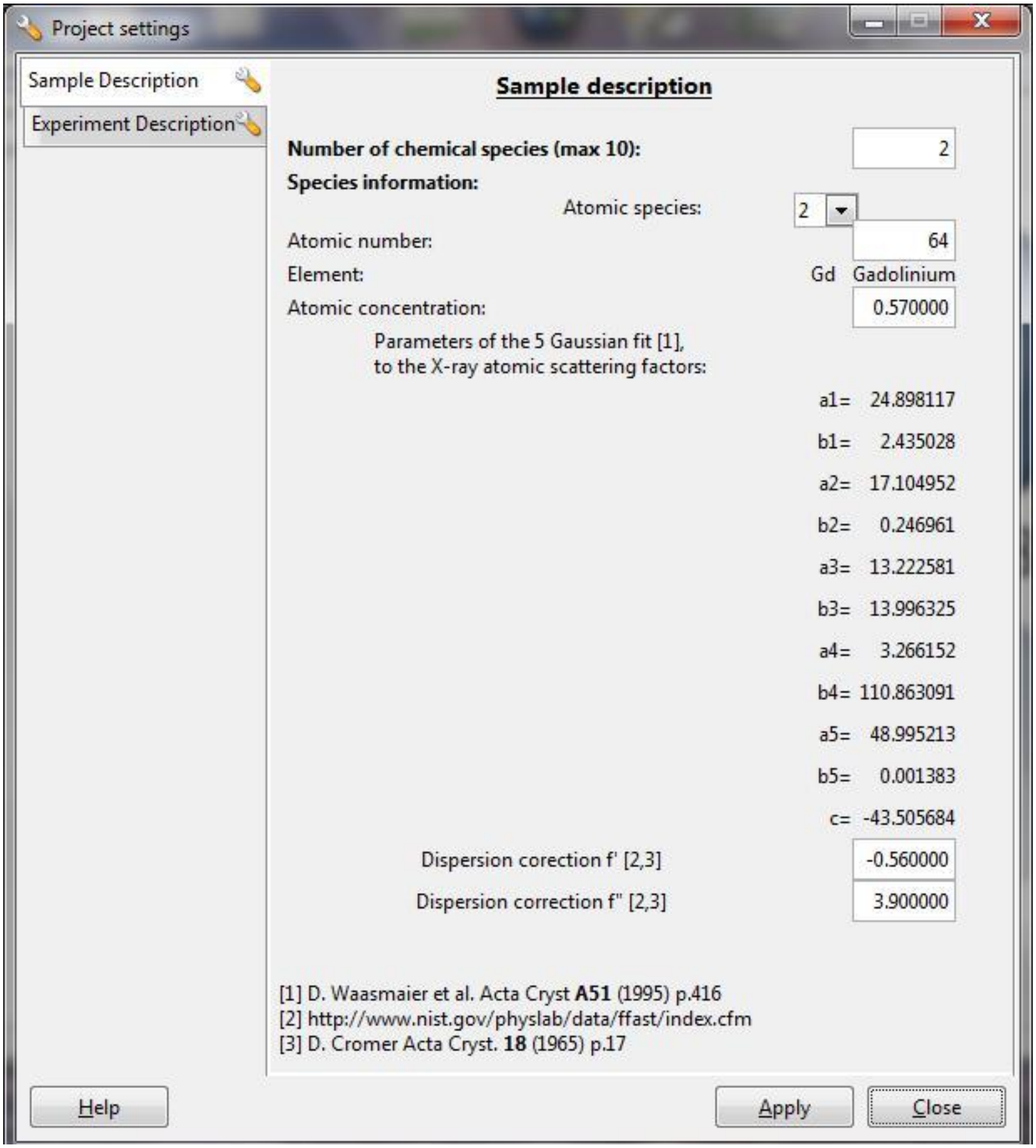

Sample description

Number of chemical species (max 10): 2
Species information:
Atomic species: 2
Atomic number: 64
Element: Gd Gadolinium
Atomic concentration: 0.570000
Parameters of the 5 Gaussian fit [1],
to the X-ray atomic scattering factors:
a1= 24.898117
b1= 2.435028
a2= 17.104952
b2= 0.246961
a3= 13.222581
b3= 13.996325
a4= 3.266152
b4= 110.863091
a5= 48.995213
b5= 0.001383
c= -43.505684
Dispersion corection f' [2,3] -0.560000
Dispersion correction f" [2,3] 3.900000

[1] D. Waasmaier et al. Acta Cryst **A51** (1995) p.416
[2] http://www.nist.gov/physlab/data/ffast/index.cfm
[3] D. Cromer Acta Cryst. **18** (1965) p.17

Next, by clicking on the "*Experiment Description*" button (left upper corner) the User is allowed to supply information about the particular XRD experiment/set up used, as shown below:

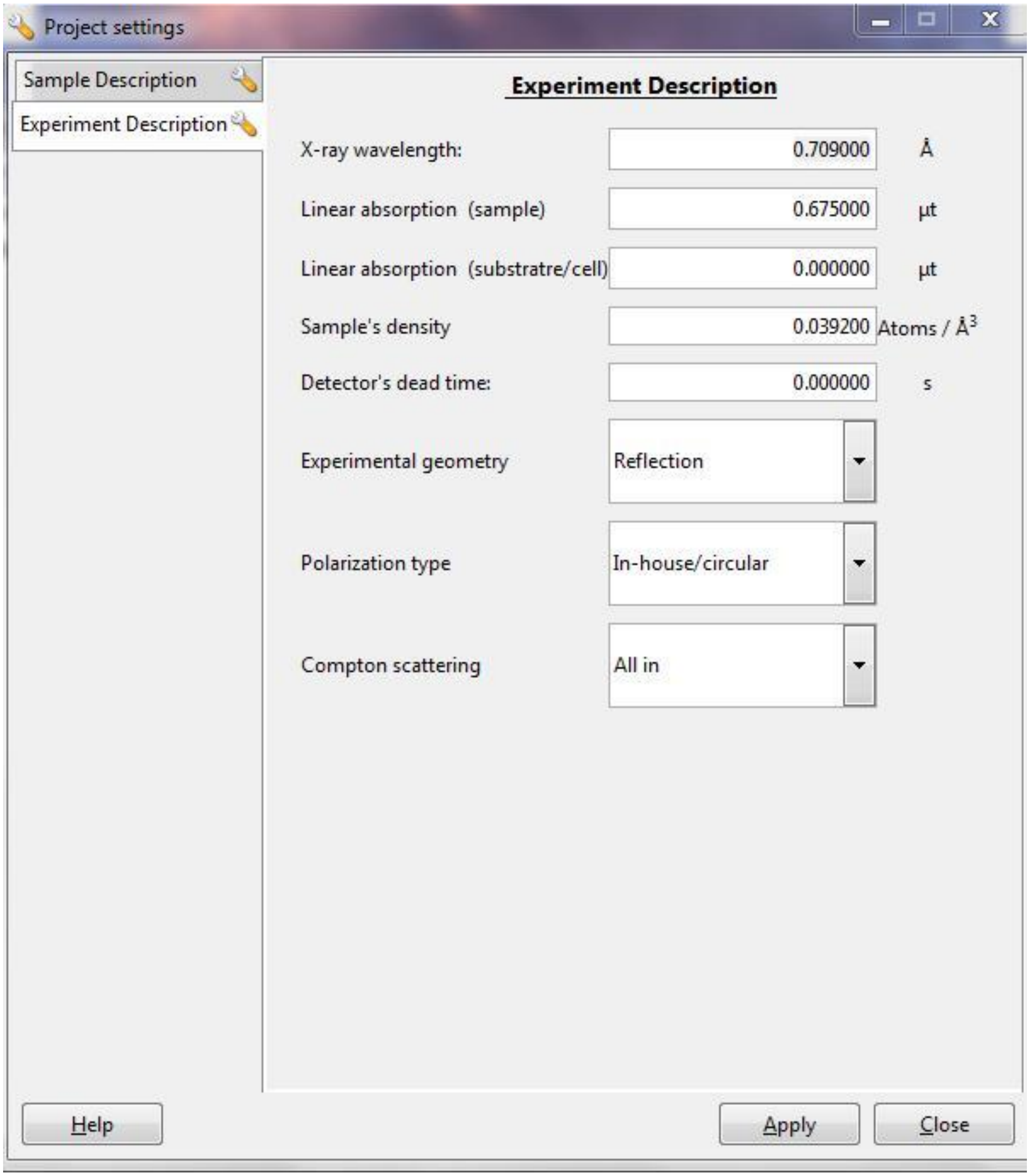

Experiment Description

X-ray wavelength: 0.709000 Å
Linear absorption (sample) 0.675000 μt
Linear absorption (substratre/cell) 0.000000 μt
Sample's density 0.039200 Atoms / Å^3
Detector's dead time: 0.000000 s
Experimental geometry Reflection
Polarization type In-house/circular
Compton scattering All in

Here we specify that x-rays with a wavelength λ=0.709 Å (i.e. Mo Ka) have been used; the sample has been measured in flat plate reflection geometry; the detector has been fast enough for the signal coming from the sample (i.e. 0.2 μs dead time), and the x-ray radiation has been circularly polarized (which is typical for sealed x-ray tube sources). There has been no x-ray energy discrimination during the XRD data collection and, hence, the XRD data contain a contribution coming from Compton/inelastic scattering (i.e. Compton scattering is "*All in*" the collected XRD data). The liner absorption factor μt for the particular $Gd_{0.57}Al_{0.43}$ sample has turned out to be 0.675. Note μt can be measured (more precise approach; see Appendix 4) or estimated [1, 2] from the material's mass absorption coefficient μ/ρ, density ρ and thickness (less precise approach). Also, here we supply information about the material's atom number density ρ_o (in this case = 0.0392 atoms/Å^3). No sample cell/substrate has been used and so the data entry for substrate's μt is zero. Note RAD_2 can also process data collected in flat plate transmission geometry or when the sample has been inside a capillary. Also, x-rays could have been completely linearly polarized (as with synchrotron sources) and Compton scattering could have been eliminated during data collection (option Compton scattering "*All out*"). The User can select between those options by clicking on the respective "drop down menus" in the "*Experiment description*" window. When all the necessary sample and experiment related information has been entered, the User should click the "*Apply*" button. RAD_2 will perform some checks on the consistency of the *Sample & Experiment Info* provided by the user and may issue a warning message if a problem has been identified. Users are advised to pay full attention to RAD's warning/error messages. *Experiment & Sample Info* that has been entered and found error free is considered "validated" and so can be exported, i.e. saved as a "**R**AD **p**roject **f**ile" (in xml format) with an extension "**.rpf**". To export/save a project file in text/xml format the user should select the option "Export" from the "Experiment & Sample*"* drop down menu (see below).

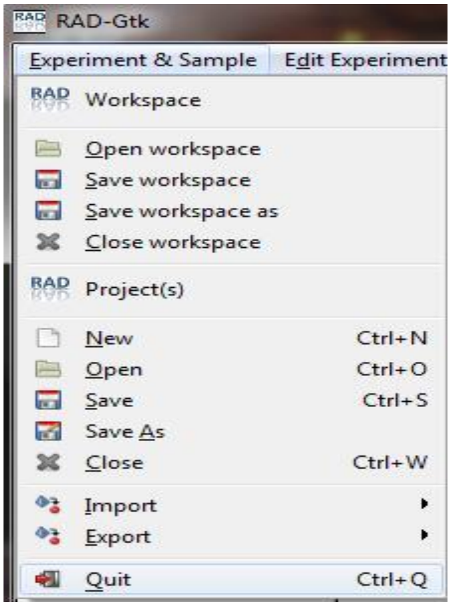

Again, RAD_2 project files exported in xml format are text files; once saved on disk they may be opened/viewed with any text editor. As an example, below is a print-out of the RAD_2 project file (in xml format) for $Gd_{0.57}Al_{0.43}$ we are discussing here:

```
<?xml version="1.0" encoding="UTF-8"?>
<!-- RadGTK v1.0 XML file -->
<rad-xml>
 <!-- Chemistry information -->
 <chemistry>
  <species number="2">
   <Z id="0">13</Z>
   <Z id="1">64</Z>
  </species>
  <element symbol="Al">
   <name>Aluminum      </name>
   <z>13</z>
   <concentration>0.430000</concentration>
   <fp>0.056000</fp>
   <fpp>0.051000</fpp>
  </element>
  <element symbol="Gd">
   <name>Gadolinium    </name>
   <z>64</z>
   <concentration>0.570000</concentration>
   <fp>-0.560000</fp>
   <fpp>3.900000</fpp>
  </element>
 </chemistry>
 <!-- Experiment information -->
 <experiment>
  <wavelength>0.709000</wavelength>
  <absorption-sample>0.675000</absorption-sample>
  <absorption-substrate>0.000000</absorption-substrate>
  <density>0.039200</density>
  <deadtime>0.0000002</deadtime>
  <geometry>Reflection </geometry>
  <monochromator>In-house/circular</monochromator>
  <compton>All in</compton>
 </experiment>
 <!-- Apply project -->
 <project>TRUE</project>
</rad-xml>
```

Experiment & Sample Info that has been entered by the user or imported from an old/existing project file can be modified by selecting the "*Edit Experiment*" option of the RAD_2 main action window.

In addition to saving only the *Experiment and Sample* related info in "xml"\text format, RAD_2 can save all steps of a particular run in a **binary project file** with an extension "**npr**". To do it the respective option from the "*Experiment & Sample"* drop down menu has to be selected. A binary project file contains not only *the Experiment and Sample* related info but also all details/steps of a particular processing of a given experimental XRD data set, including the raw experimental XRD data and the resulted PDF data. **A saved binary project "npr" file can be opened/loaded into RAD_2 allowing a particular program run to be easily reproduced and/or modified depending on the User's needs.** Pieces of information stored and then retrieved from a binary "**npr**" file are shown below:

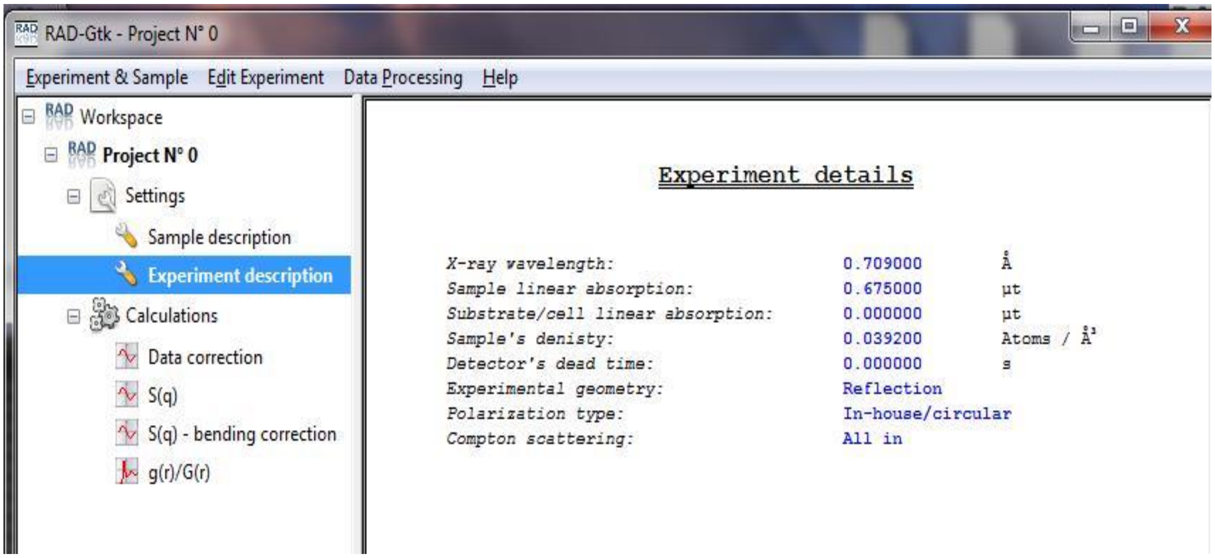

Experiment details

X-ray wavelength: 0.709000 Å
Sample linear absorption: 0.675000 µt
Substrate/cell linear absorption: 0.000000 µt
Sample's denisty: 0.039200 Atoms / Å^3
Detector's dead time: 0.000000 s
Experimental geometry: Reflection
Polarization type: In-house/circular
Compton scattering: All in

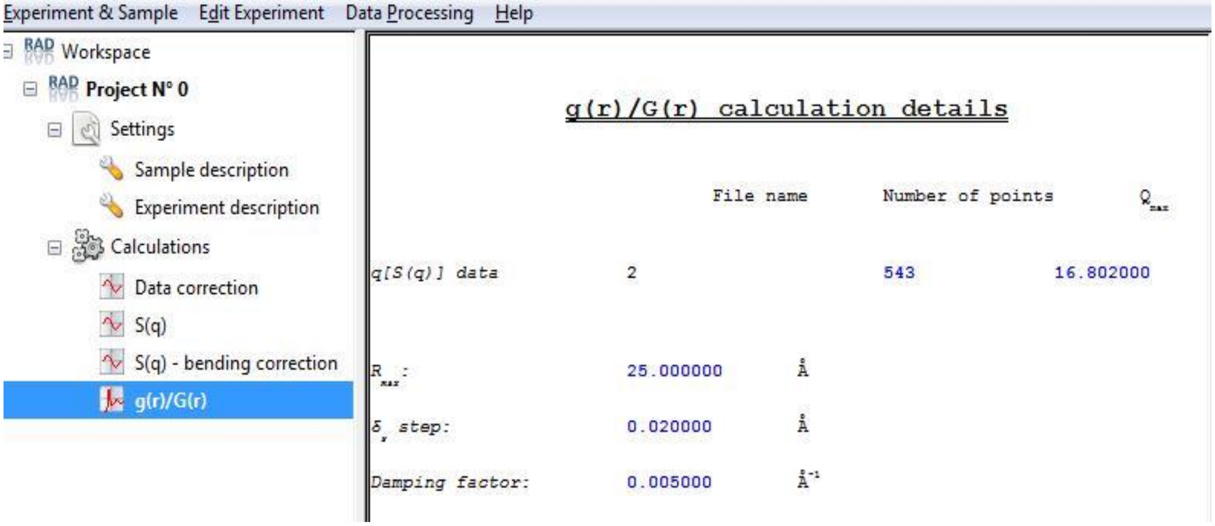

g(r)/G(r) calculation details

	File name	Number of points	Q_{max}
q[S(q)] data	2	543	16.802000

R_{max}: 25.000000 Å
δ_r step: 0.020000 Å
Damping factor: 0.005000 Å^{-1}

Another new feature implemented in RAD_2 is the so-called **Workspace**. It allows to save/open more than one RAD_2 projects at a time, and to compare the data/results in them.

ii) Edit Experiment option of RAD_2:

If the user starts from scratch (i.e. a completely new RAD_2 run) he/she should select Option "**New**" from the "*Experiment & Sample"* drop down menu list and then go to "*Edit Experiment Menu*" (see below) to enter the sample and experiment Info. Alternatively, if the user had imported an existing RAD_2 project file, he/she may use the "*Edit Experiment*" menu to walk through the "*Experiment & Sample Info"* forms, make changes, validate and eventually export/save the modified "*Experiment and Sample Info"* as a, for example, RAD_2 "rpf" project.

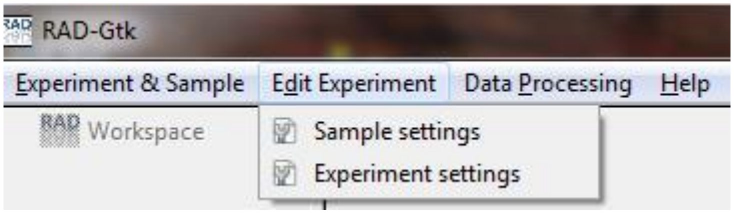

Note changes in the "*Experiment & Sample Info"* are accepted and taken into account in the XRD data processing/PDF calculations only after the "*Apply*" button has been hit and the validation procedures completed with success (i.e. no RAD_2 error/warning messages have been issued).

iii) Data Processing options of RAD_2:

This option (see below) can be activated only if a "RAD project file" has been created from scratch, imported (in the case of "**rpf**" format) or opened (in the case of "**npr**" format), and validated.

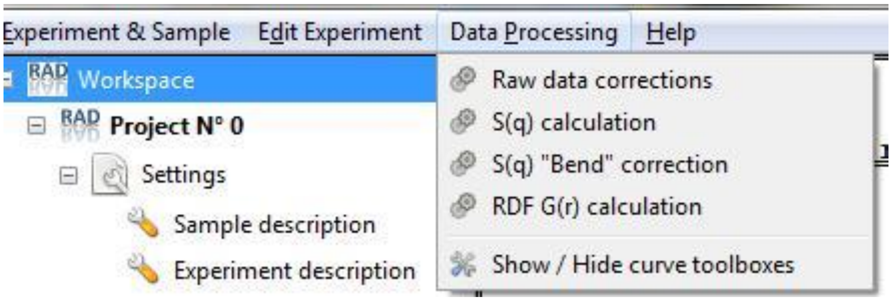

The option "*Raw data corrections*" allows the user to:

1) Correct an experimental XRD data set for background (e.g. air) & sample cell (e.g. empty capillary) scattering, absorption and polarization, smooth the data (if necessary), extend/extrapolate it (linearly) to $q=0$ wave vectors and put it in equidistant Δq steps. The

so corrected XRD data can be saved as a (x,y) file in ascii format or directly used in the next step of the data processing, that is "S(q) calculation". To do the experimental corrections the User activates the step "*Raw data corrections"* from the **Data processing RAD_2** option and gives the names of the files containing the XRD intensities scattered from the sample (file **GdAl.th** in our example, see below) and the background/air (file **Backgr_GdAl.th** in our example, see below). Note, in this example, the sample has been free standing, i.e. no sample support/holder scattering has been hitting the detector.

Data correction

Data correction

Data format: 2θ vs. Intensity

Sample scattering data file name: GdAl.th — 429 2θ points, $2\theta_{max}$ = 143.000000

☑ Background correction: Backgr_GdAl.th — 429 2θ points, $2\theta_{max}$ = 143.000000

☐ Substrate / cell scattering: (None)

☑ Data smoothing: Slight

☑ show / hide curves toolbox

Also, in this example we have decided to smooth the XRD data *("slightly").* When the "*Apply*" button is hit (lower right corner; see above) RAD_2 reads the experimental XRD data files and reports the number of data points in them (429 in the consider example) as well as the value of the Bragg angle/wave vector for the last XRD data point collected. When the experimental XRD data sets are read and corrections on them done without any problem (RAD notices some problems and reports about them), a separate pop-up window labeled "*Tool boxes*" in the upper left corner appears; see below. It allows the User to view the raw sample & background XRD data sets, the corrected XRD data, and save the latter.

Note, occasionally this, and other smaller-size RAD_2 program windows, may become hidden behind the main RAD_2 program window and so remain out of User's sight. Users: feel free to shift RAD_2 windows around the computer screen to be able to see/access them in the most convenient (for you) way.

By checking the box "*Raw data*" (see below)

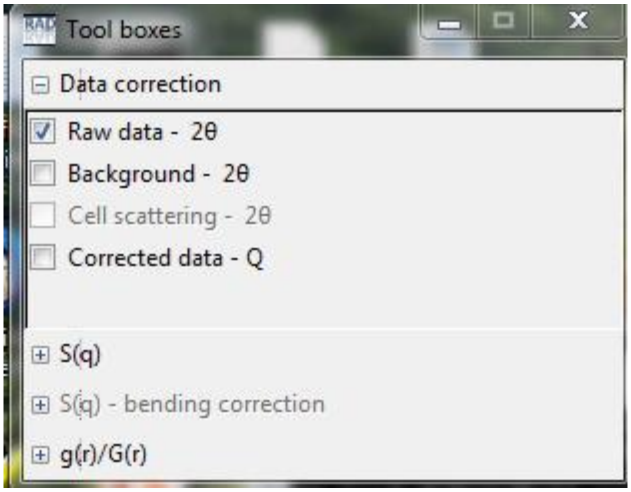

☑ Raw data - 2θ
☐ Background - 2θ
☐ Cell scattering - 2θ
☐ Corrected data - Q

the User can plot/view the raw experimental data he/she is analyzing. They appear in yet another "*Data plotting window"* (see below).

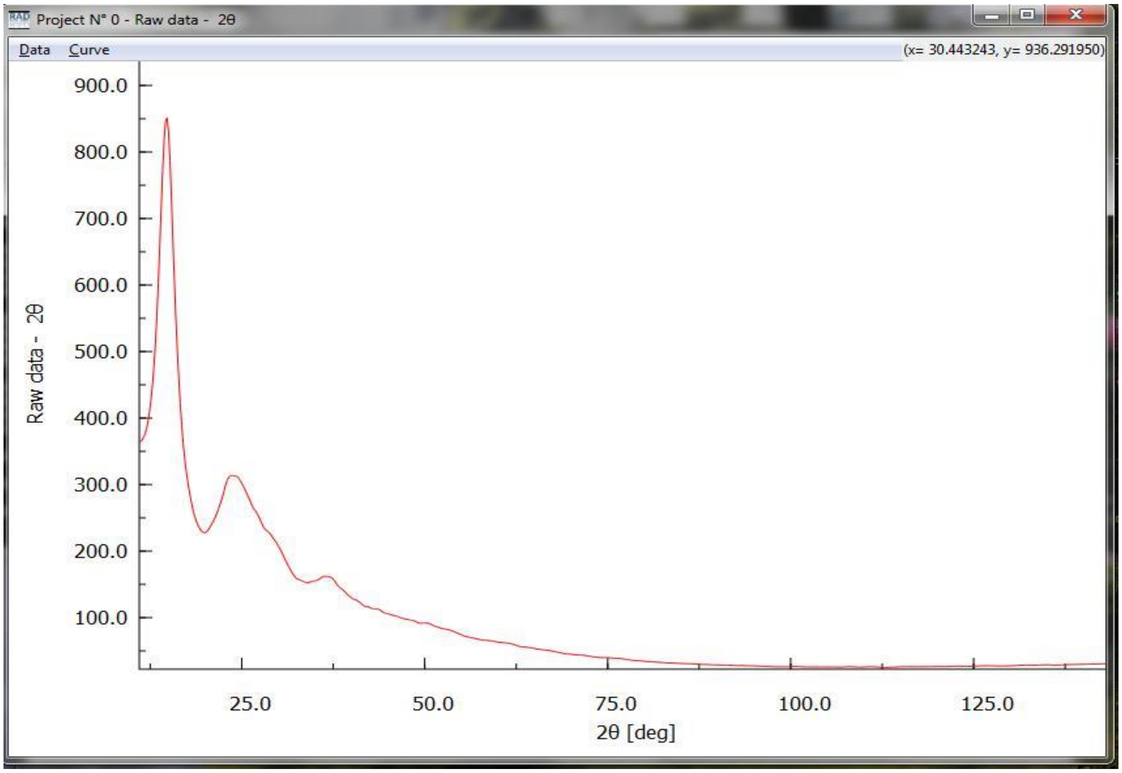

If the User checks the "*Corrected data*" box (see below)

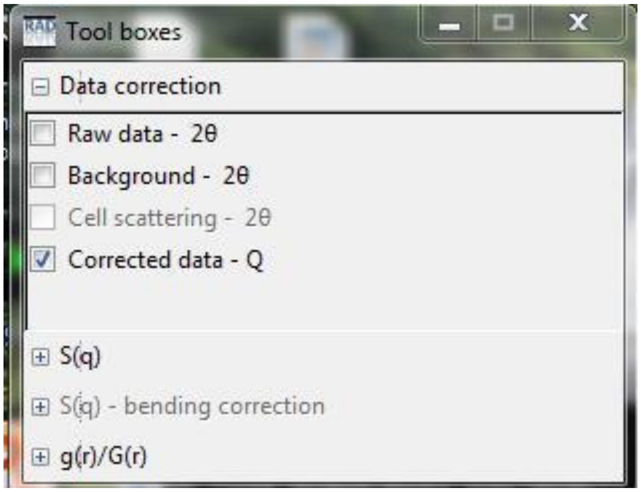

Tool boxes

⊟ Data correction

☐ Raw data - 2θ

☐ Background - 2θ

☐ Cell scattering - 2θ

☑ Corrected data - Q

⊞ S(q)

⊞ S(q) - bending correction

⊞ g(r)/G(r)

he/she can plot/view the corrected and extrapolated to q=0 XRD data; see below.

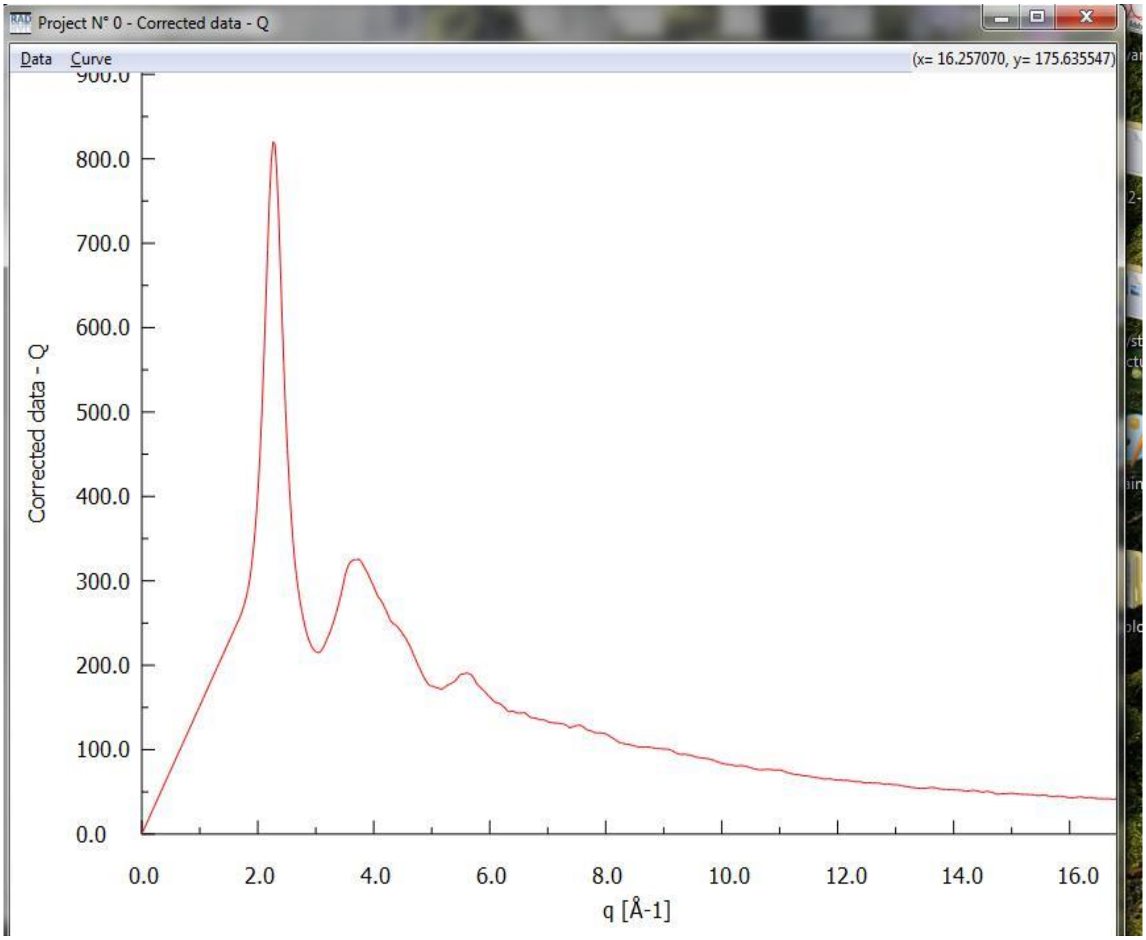

If the user is satisfied with the experimental XRD data corrections and would like to save the data, he/she will have to check the "*Data*" option in the upper left corner of the "*Data plot window*" (see below).

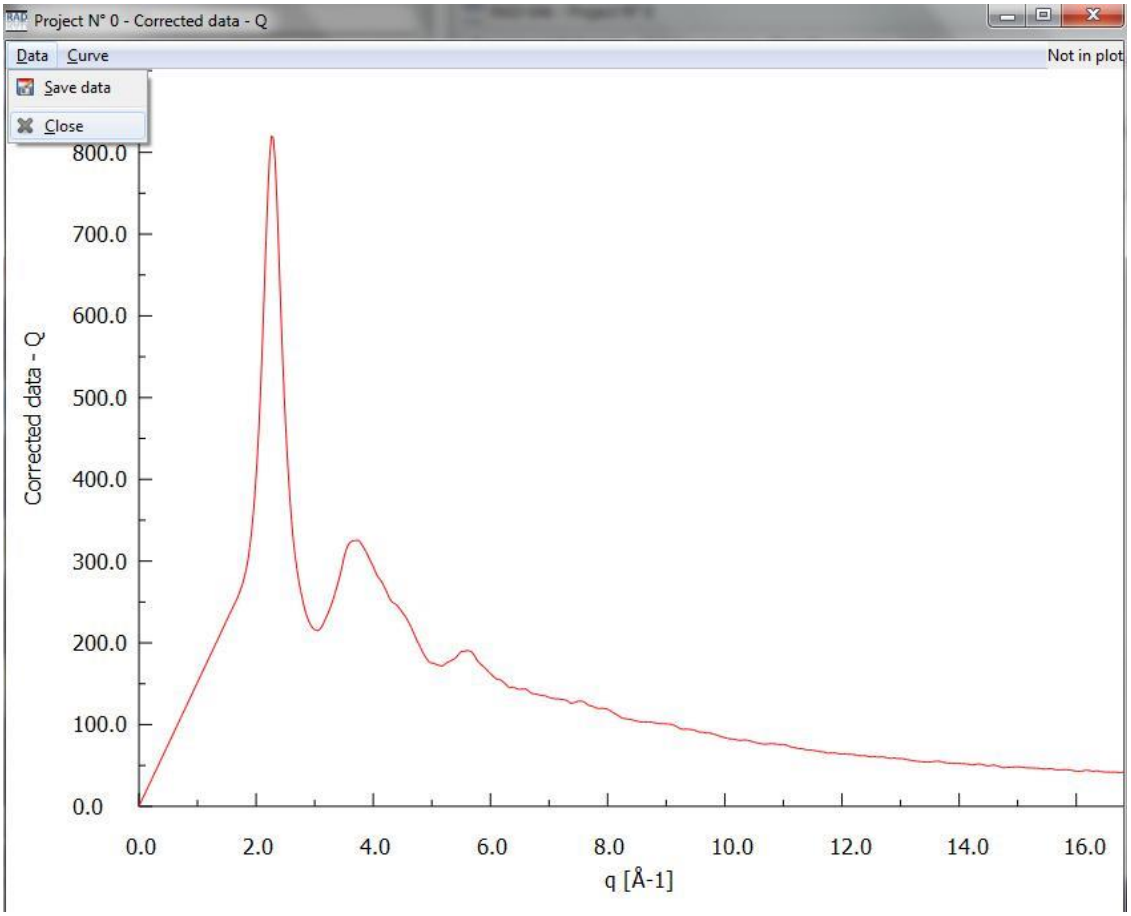

A drop-down menu (see above) will appear allowing the user to save the corrected XRD data or close the data plot window. If the "*Save data*" option is selected a new window appears (see below). It allows the user to save the corrected XRD data either in two column **(x,y)** ASCII or in four column **(x,y,0=zero,1.=one)** ASCII format. XmGrace output format is for those who like using this (Linux) plotting software; see below). **Note (x,y) ASCII data format has been chosen to be the working format in the examples of RAD_2 shown here. Indeed, (x,y) ASCII has been chosen to be the format of the data saved/read by RAD_2.** In this example we save the corrected XRD data in a file – "*GdAl.cor*". The user is free to select any file name/extension and folder where the corrected XRD data will be saved. Again, RAD_2 users should **always** save their results in **two column** (**x,y**) **ASCII format** when those results are to be used in other calculations performed by RAD_2. Use the **four column (x,y,0,1) ascii format** if RAD_2 output is to be ported to DISCUS (http://discus.sourceforge.net/) or PDFgui (http://www.diffpy.org/) program suits.

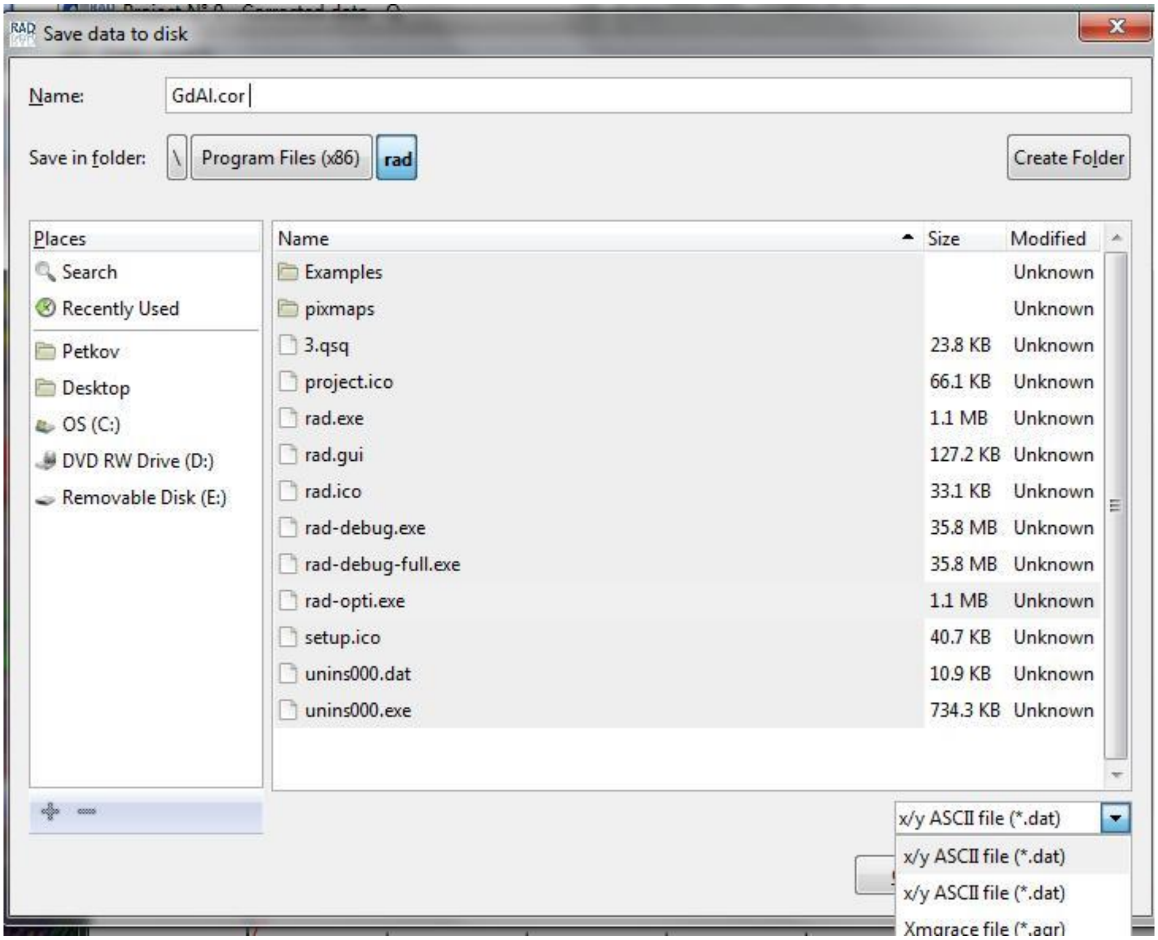

Name: GdAl.cor

Save in folder: \ Program Files (x86) rad

Name	Size	Modified
Examples		Unknown
pixmaps		Unknown
3.qsq	23.8 KB	Unknown
project.ico	66.1 KB	Unknown
rad.exe	1.1 MB	Unknown
rad.gui	127.2 KB	Unknown
rad.ico	33.1 KB	Unknown
rad-debug.exe	35.8 MB	Unknown
rad-debug-full.exe	35.8 MB	Unknown
rad-opti.exe	1.1 MB	Unknown
setup.ico	40.7 KB	Unknown
unins000.dat	10.9 KB	Unknown
unins000.exe	734.3 KB	Unknown

If the "*Curve*" option in the "*Data plot window*" is selected the user can

i) edit the way data is shown in the "*Data Plot window*" (e.g. rescale axis, change colors, show/hide legend etc); see below:

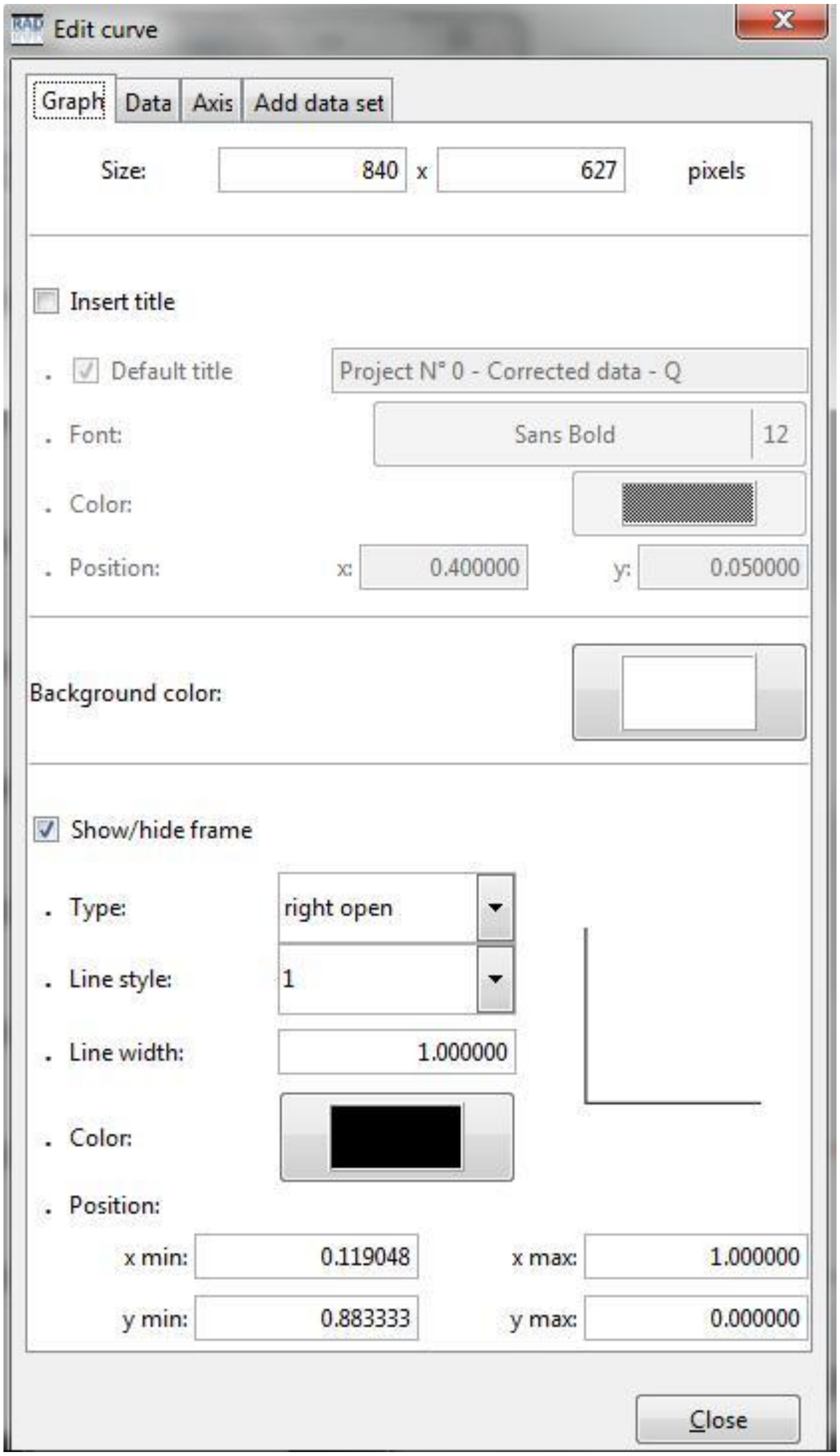

Size: 840 x 627 pixels

☐ Insert title

☑ Default title: Project N° 0 - Corrected data - Q

Font: Sans Bold 12

Color: ▩

Position: x: 0.400000 y: 0.050000

Background color: ☐

☑ Show/hide frame

Type: right open

Line style: 1

Line width: 1.000000

Color: ■

Position:

x min: 0.119048 x max: 1.000000

y min: 0.883333 y max: 0.000000

and

ii) export the "*Data Plot Window*" in PNG, PDF or SVG graphics formats (see below):

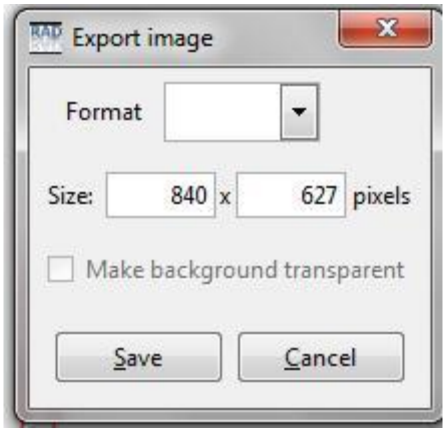

Size: 840 x 627 pixels

Experimental XRD data format: RAD_2 assumes (see files “GdAl.th” and “Backgr_GdAl.th” for example) that the experimental XRD data is presented in two columns (2θ or q values vs XRD intensity) in ASCII format. RAD saves and uses the computed corrected XRD data, reduced structure factor q[S(q)-1] data and atomic PDF/RDF data in the same two column **(x,y) ascii** format. As an example, below is what “GdAl.th” looks like when opened/viewed with a text editor: just two columns of numbers. The first is the Bragg angle (in 2θ), the second – the experimental XRD intensities (in counts per second).

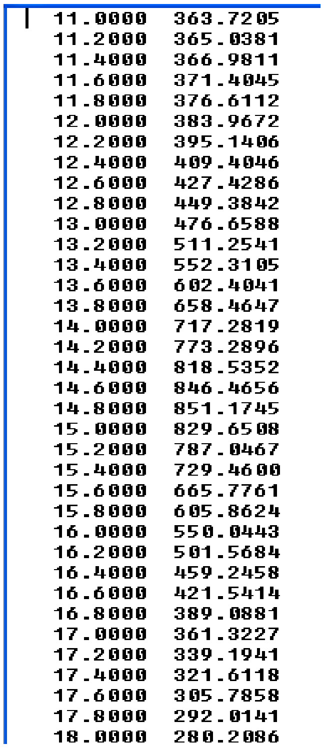

```
11.0000  363.7205
11.2000  365.0381
11.4000  366.9811
11.6000  371.4045
11.8000  376.6112
12.0000  383.9672
12.2000  395.1406
12.4000  409.4046
12.6000  427.4286
12.8000  449.3842
13.0000  476.6588
13.2000  511.2541
13.4000  552.3105
13.6000  602.4041
13.8000  658.4647
14.0000  717.2819
14.2000  773.2896
14.4000  818.5352
14.6000  846.4656
14.8000  851.1745
15.0000  829.6508
15.2000  787.0467
15.4000  729.4600
15.6000  665.7761
15.8000  605.8624
16.0000  550.0443
16.2000  501.5684
16.4000  459.2458
16.6000  421.5414
16.8000  389.0881
17.0000  361.3227
17.2000  339.1941
17.4000  321.6118
17.6000  305.7858
17.8000  292.0141
18.0000  280.2086
```

The number of data points (per file), experimental or RAD computed, **may not be larger than 30,000**. Also, a single experimental XRD intensity value and, therefore, computed S(q) and G(r) values **should not be larger than 10^6**. Users, please, try not to exceed count rates of 10^6 cps (per single detector), do not saturate the detector(s) and so go in the non-linear detector dead time correction regime ! Keep the number of data points (per pattern) below 30,000 and normalize the XRD intensities in your XRD patterns per second/per the number of detectors/per the number of angular sectors of integration (if using an area detector) etc, i.e**. take care that no single intensity data point in the experimental XRD files has a value greater than 10^6 cps.** Then the XRD data corrections implemented in RAD_2 may work. Indeed why such limitations ? Users: RAD_2 is just like a…. car. A car is designed to tow a particular load, carry a particular number of passengers, run with a particular maximum speed etc. Attempts to run a car beyond its build-in capabilities will blow its engine out. The same will happen to RAD_2. No good for anybody.

Also, the author (VP), after some careful thoughts, decided that, for now, it does not worth the effort to propagate "experimental/counting/statistical etc" errors from the raw XRD data to S(q) and finally to PDF/RDF G(r). Error propagation via a Fourier transformation is tricky. Instead the author suggests RAD_2 users consider that all data points of the derived S(q)s and G(r)s are with the same "random-type" (+/-) error, **i.e. assume/use uniform errors/weights in all S(Q)/PDF/RDF data.** By the way, studies [7] showed that this assumption is quite appropriate. Within this assumption each **S(Q)/PDF/RDF data** point is assigned an uniform (i.e.="**1**") error. The **S(Q)/PDF/RDF data** then can be saved in the (**x,y,0,1 ascii format)** and directly used by PDFgui and DUSCUS in structure refinements. The standard deviations of the structural parameters resulted from those refinements will be based on the uniform "**one unit**" error in each of the **S(Q)/PDF/RDF data points** against which the structure model is tested/refined.

Here is may be the place to introduce the User to the very special features of RAD_2 plotting window:

i) Upon positioning the mouse on the plot window and “left click” a selected portion of the shown data can be “zoomed in”. To revert the action click “Autoscale’ in the small size ‘pop up” window that appears in parallel with the “left click”.

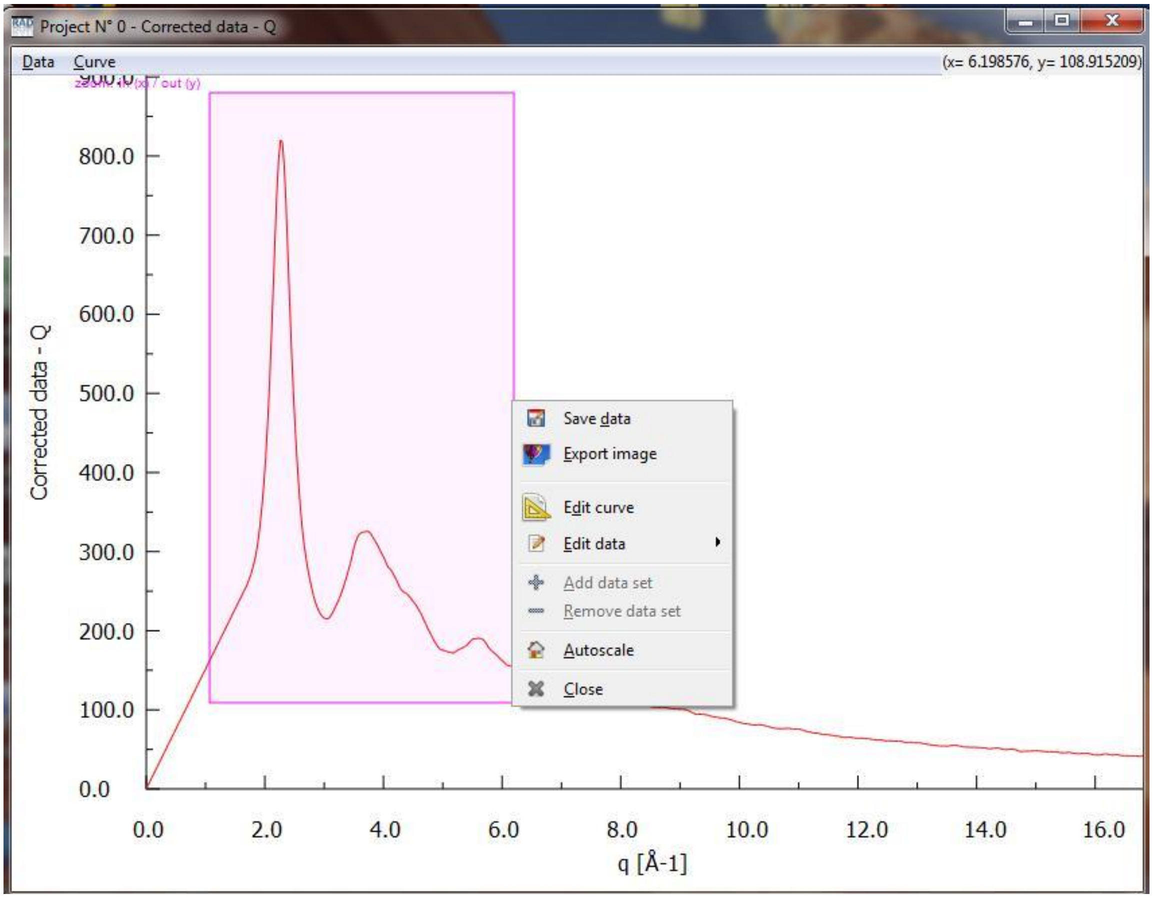

ii) Upon positioning the mouse on the plot window and “right click” a small size “pop-up” window appears (see below). It allows to “Save” the data shown in the plot in ascii format, “Export” the plot in some graphics format, “Edit the Curve/Plot” attributes such as axis labels, tick marks, fonts etc, and numerically “**EDIT**” the data. The latter option is illustrated in the example below. In the plot below the corrected I(q) data for $Gd_{0.57}Al_{0.43}$ are shown. By clicking on “EDIT” and following the horizontal banner, the Corrected I(q) data is chosen for “Editing”.

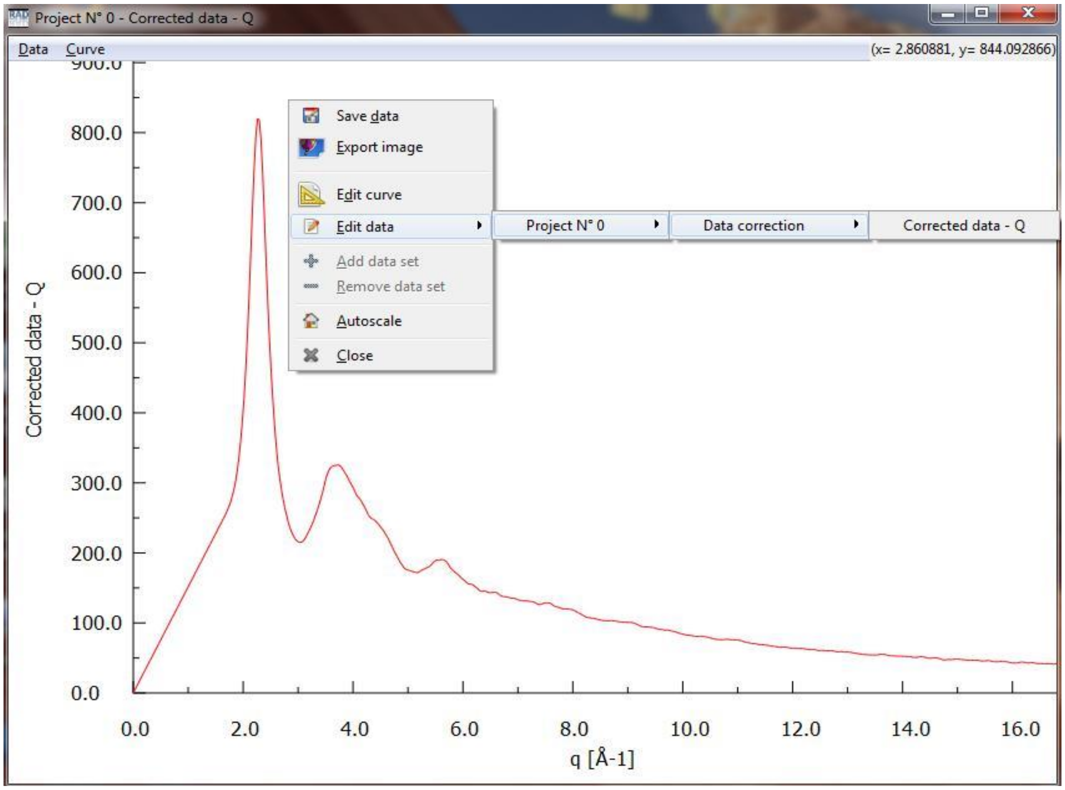

Once the I(q) data set is chosen an “Excel” type of 2 column Table appears showing the numerical values of the data presented in the plot. A “right click” on the Table opens an “action window for “Cell/Table” based operations (see below). In particular:

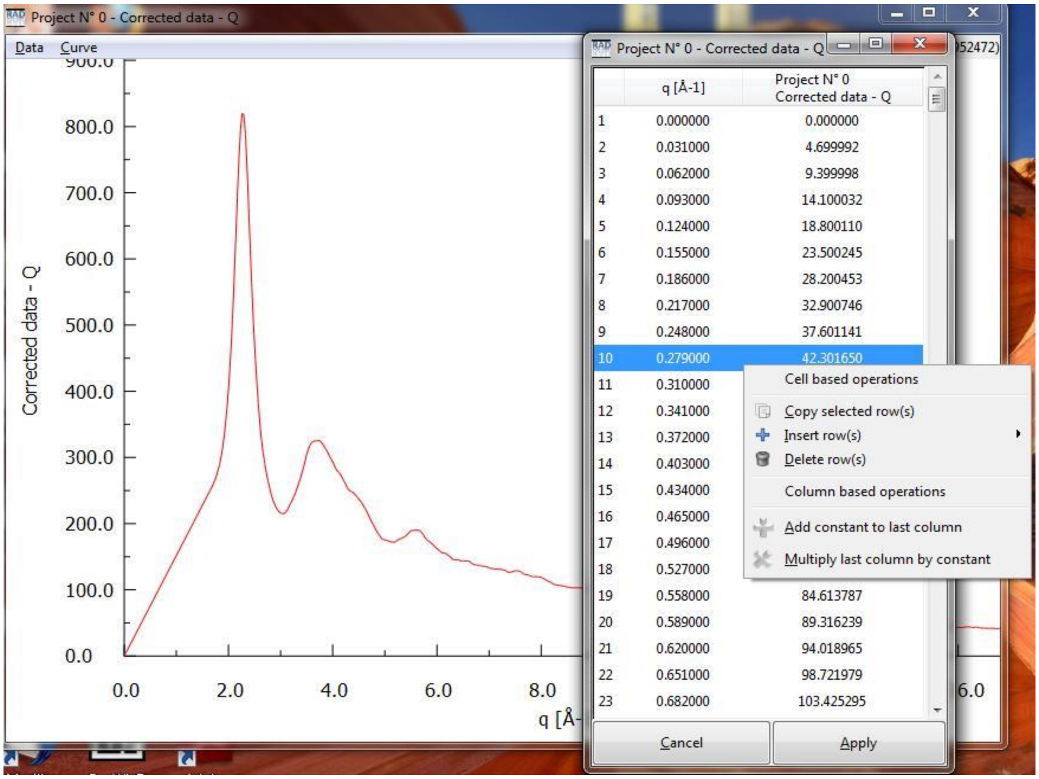

	q [Å-1]	Project N° 0 Corrected data - Q
1	0.000000	0.000000
2	0.031000	4.699992
3	0.062000	9.399998
4	0.093000	14.100032
5	0.124000	18.800110
6	0.155000	23.500245
7	0.186000	28.200453
8	0.217000	32.900746
9	0.248000	37.601141
10	0.279000	42.301650
11	0.310000	
12	0.341000	
13	0.372000	
14	0.403000	
15	0.434000	
16	0.465000	
17	0.496000	
18	0.527000	
19	0.558000	84.613787
20	0.589000	89.316239
21	0.620000	94.018965
22	0.651000	98.721979
23	0.682000	103.425295

Selected rows from the Table can be deleted, new rows can be inserted, the value of a particular data point/cell in the Table can be modified, and the whole “second/last” column in the Table can be multiplied/divided by a number. Also, a number could be added/subtracted from the “last/second” column in the Table. The last two features can be very useful when a User sees that a particular data set needs to be edited numerically (e.g. background signal happens to be way too strong so we need to “make it weaker” by dividing by 2 for example). After performing the numerical “Editing” the User should click the “Apply” button at the bottom of the Table (see above). The so Edited data then become available for repeating a particular step in the XRD data reduction process. To do it, close all Plot windows, go back to the particular step in the data analysis, repeat it, and see if the outcome is better. Sure a data set/file can be saved on disc, “Edited” as described above by some other piece of software, loaded back into RAD_2 and used for repeating some step in the XRD data analysis. It is up to the User to decide how to “Edit” a particular data set: by using RAD_2 as described above or by some other means.

2) The option “*S(q) calculation*” allows the User to derive structure factor S(q) and reduced structure factor q[S(q)-1] data from corrected XRD data.

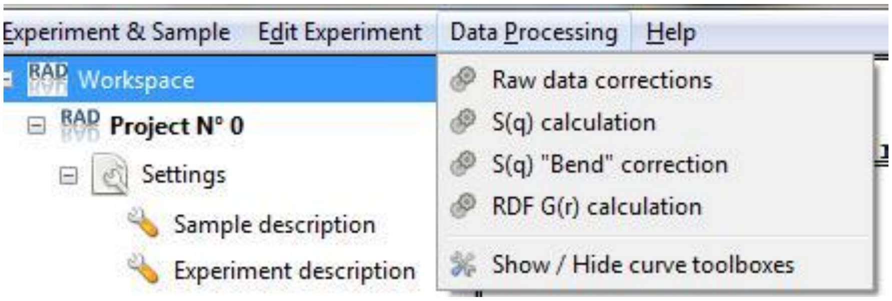

To do it the User should activate the option “*S(q) calculation*” from the drop-down menu list of “*Data processing*” main RAD_2 window (see above). The User may selects the option “Read corrected Q data from file” (see below) and enter the name of the file with corrected XRD data that has been saved on disc (file “GdAl.cor” in our example). Alternatively, the User may decide to directly use the I(q) data corrected in the previous step in the XRD data analysis (option “Use corrected Q data”) since I(q) is still in the computer memory. RAD_2 either reads the corrected I(q) data from a saved on disc file or directly uses I(q) data resulted from the just performed step “Raw data correction”.

Either way, in our example, the corrected I(q) data points are 543 in number and with Qmax of 16.8 Å^{-1}. Since Compton scattering is present in the XRD data (because no x-ray energy sensitive detector has been used during data collection) the former has to be computed and subtracted from the latter. Here the User should decide about the value for the so-called Breit-Dirac recoil factor [2]. RAD offers values of 1, 2 or 3.

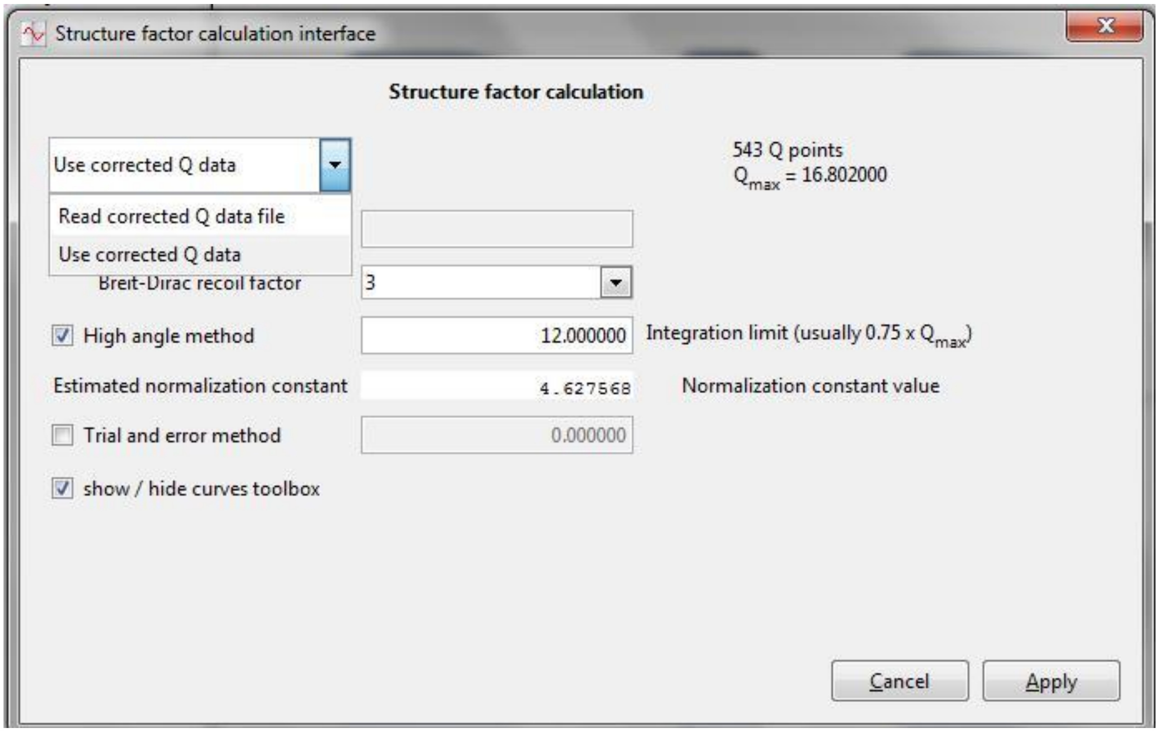

Use corrected Q data

543 Q points
Q_{max} = 16.802000

Breit-Dirac recoil factor: 3

☑ High angle method: 12.000000 Integration limit (usually 0.75 x Q_{max})

Estimated normalization constant: 4.627568 Normalization constant value

☐ Trial and error method: 0.000000

☑ show / hide curves toolbox

Also, the User selects the way the corrected XRD data is to be normalized into absolute/electron units. At first the so-called “High-angle method” may be selected (by checking the relevant box, see above) and a value for the “limit of integration” - provided (12 Å^{-1} in our example). The User hits “*Apply*”, RAD_2 computes a normalization constant (4.627 in the example above), converts the corrected XRD data in absolute units, subtracts the computed Compton scattering and computes the structure factor S(q) and the so-called reduced structure factor q[S(q)-1] [2,3] (the the *J. Apll. Crystallog.* paper attached to this manual; it gives a description of the normalization process and S(q) derivation in some more detail). From the “*Tool box*” window (see below) we select to plot/view the so-called reduced structure function q[S(q)-1] data.

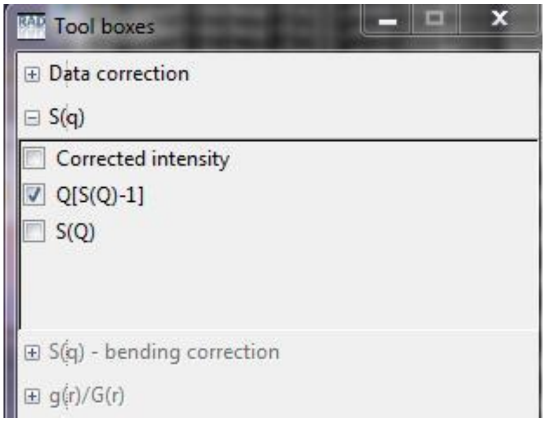

Tool boxes

⊞ Data correction

⊟ S(q)

☐ Corrected intensity

☑ Q[S(Q)-1]

☐ S(Q)

⊞ S(q) - bending correction

⊞ g(r)/G(r)

The resulted q[S(q)-1] data is shown below, and it looks relatively good.

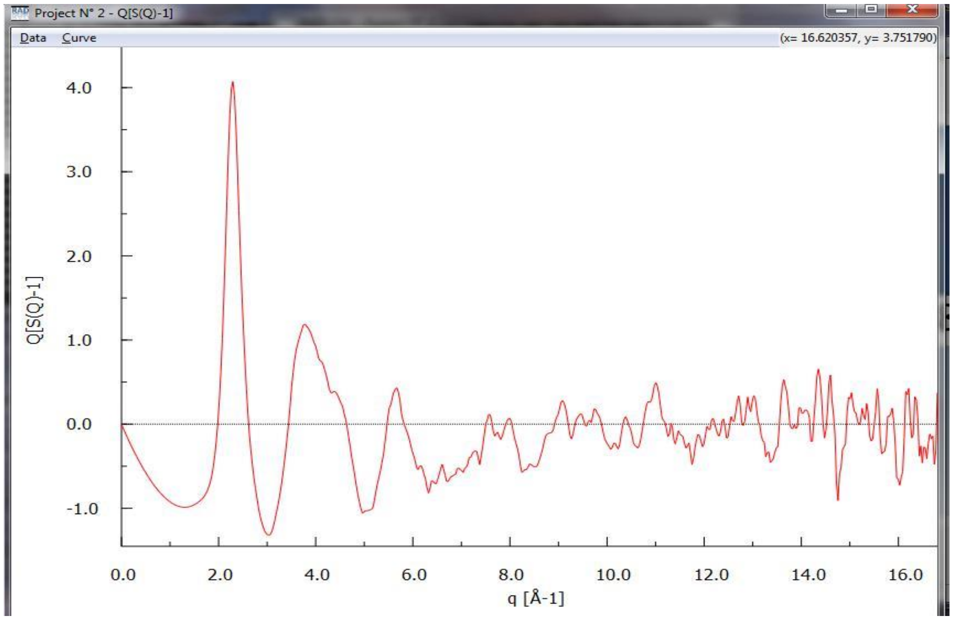

Occasionally, as shown below, the computed q[S(q)-1] may exhibit a "peculiar, non-physical" behavior, i.e. not to oscillate about zero over the range of q values covered by the experiment under consideration.

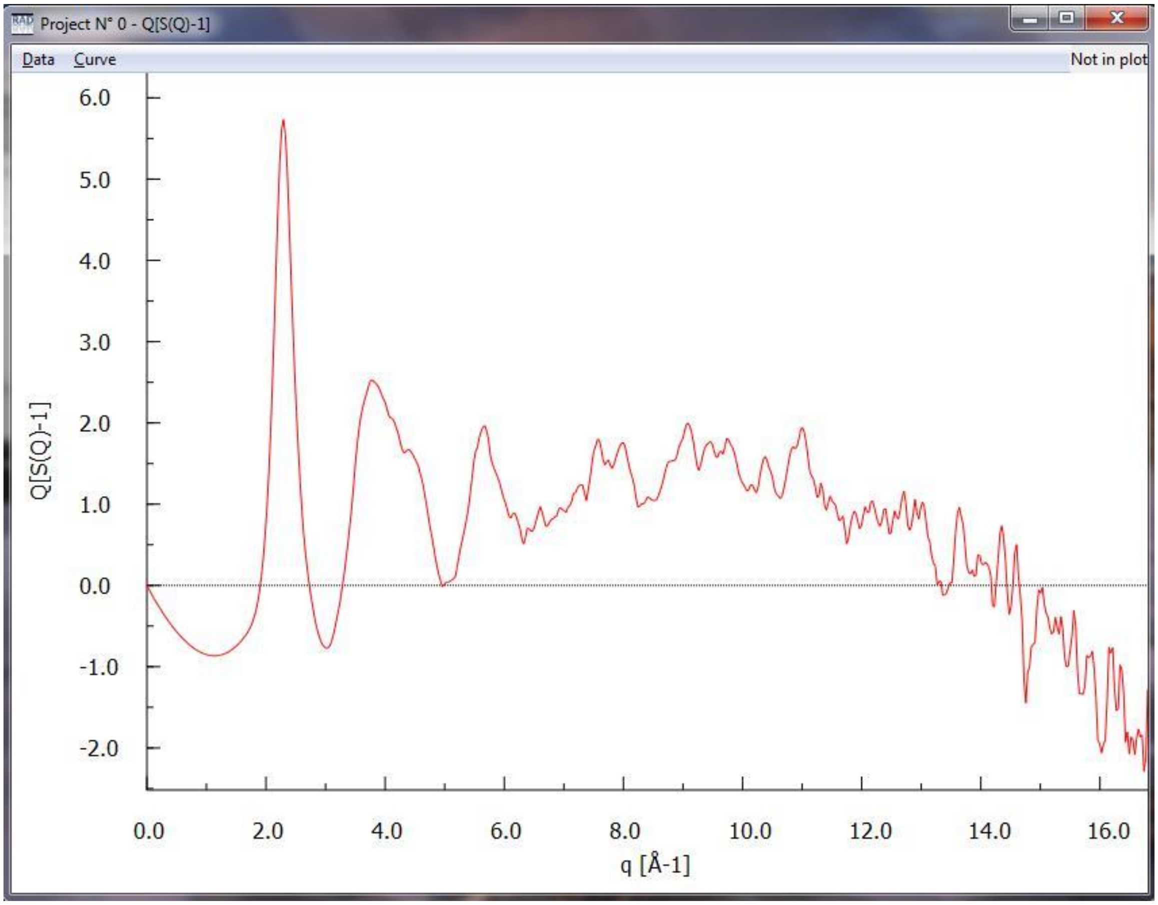

This may be due to some problems with the raw data (e.g. incorrectly collected background signal) and/or inconsistencies in the step "Raw data correction" (e.g. incorrect value for the linear absorption factor μt) and/or problems in the step "S(q) calculation" where the I(q) data is normalized in absolute/electron units (e.g. incorrectly estimated Compton scattering). RAD_2 provides an option to "correct" for some small errors in q[S(q)-1] by adding/subtracting a constant to the corrected I(q)/XRD data (a constant of 0.5 in the example below).

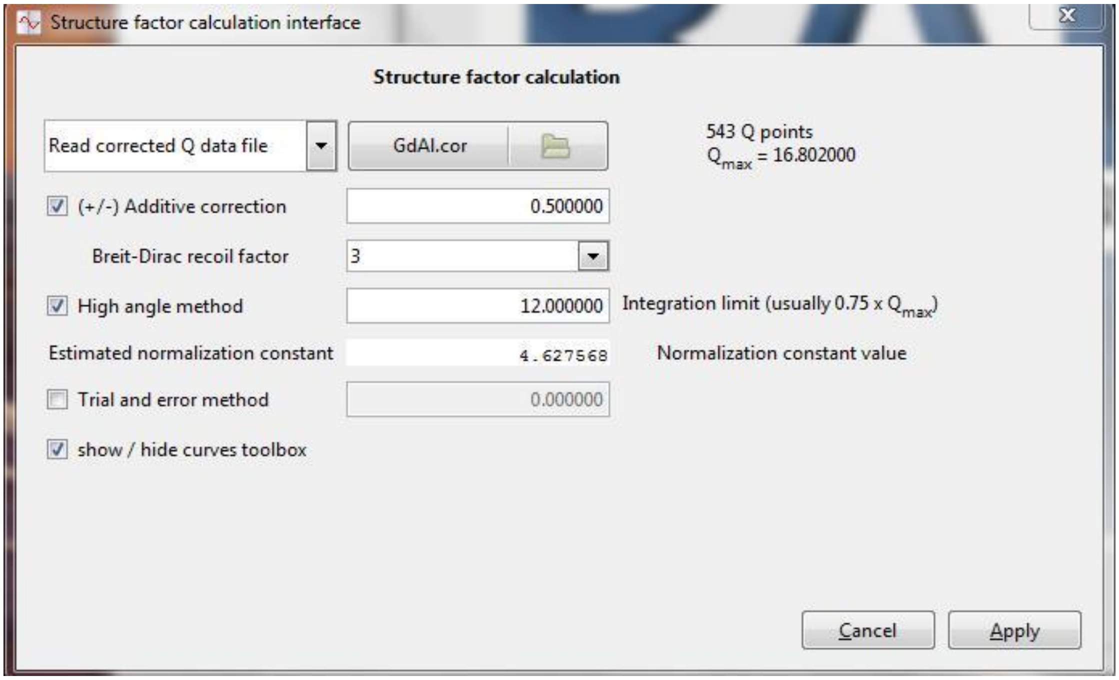

Structure factor calculation

Read corrected Q data file ▾ GdAl.cor

543 Q points
Q_{max} = 16.802000

☑ (+/-) Additive correction 0.500000

Breit-Dirac recoil factor 3 ▾

☑ High angle method 12.000000 Integration limit (usually 0.75 x Q_{max})

Estimated normalization constant 4.627568 Normalization constant value

☐ Trial and error method 0.000000

☑ show / hide curves toolbox

By “trial and error” (yes, human judgment may still be important in PDF/RDF data analysis) we “decide” to add a small number (0.5) to the originally corrected I(q)/XRD data, and repeat the normalization. Adding/subtraction a constant to I(q) can be done in the step S(q) derivation (by checking the option “+/- Additive correction”; see above) or in the “Plot window” using the “EDIT data” option. Occasionally, small additive correction to I(q) may help q[S(q)-1] exhibit a more “physical” behavior (compare the “curved” q[S(q)-1] with the “good looking” q[S(q)-1] shown in the plot below).

When we are satisfied with the q[S(q)-1] data we may save it. To do it we have to check

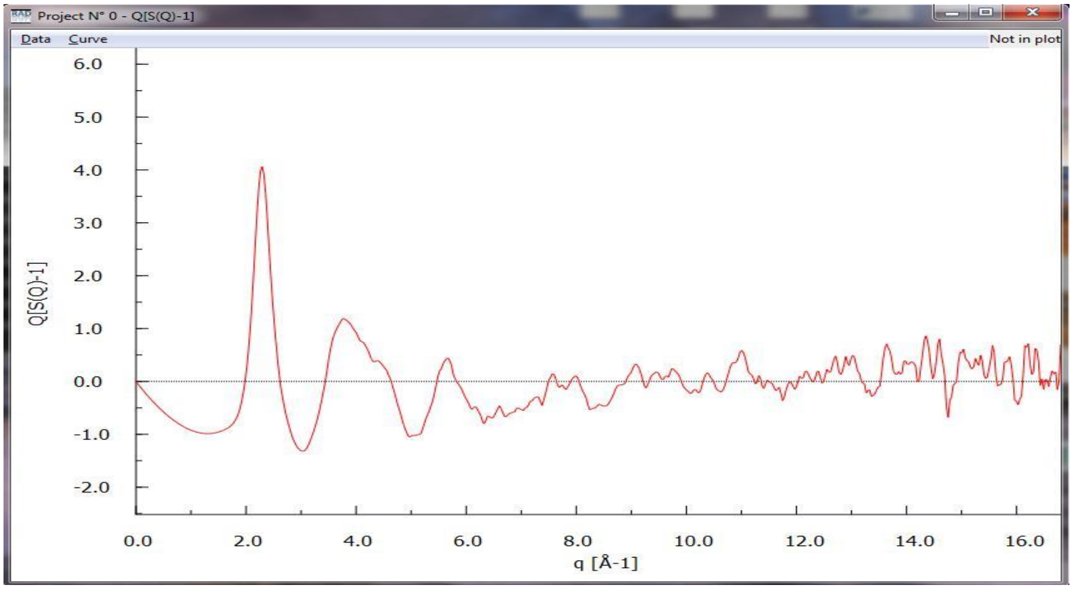

the "*Data*" option in the *"Data plot window*", pick a file name and folder where the q[S(q)-1] data will be saved. The User is free to select any file name/extension for the q[S(q)-1] data. We saved it under the name "*GdAl.qsq"* in two column (x,y) ascii format.

Note, the author maintains the point of view that having the structure function S(q) and atomic PDF/RDF function normalized in absolute/electron units is a great ADVANTAGE of the atomic PDF analysis technique. This allows data sets to be directly compared to each other when looking for fine structural changes, quantitative phase analysis to be performed on a rigorous basis, atomic coordination numbers to be computed precisely etc. Accordingly, RAD_2 is designed to always perform such normalization. Also, RAD_2 output is deliberately designed not to be automatic but to require some judgment/approval on behalf of the User doing the calculations. Blindly accepting results from experimental XRD data analysis aimed at atomic PDFs/RDFs derivation by using a computer program in an automated, "black-box" mode may result in unpredictably wrong results. Sure, the User-oriented approach of RAD_2 may require some more time to process an XRD data set into atomic PDF/RDF but QUALITY is PRICELESS. It is the PDFs/RDFs QUALITY and NOT quantity RAD_2 is primarily aiming at yet keeping the XRD data processing protocol as simple and User-friendly as possible.

The option "*RDF G(r) calculation*" allows the User to compute an atomic PDF/RDF from a set of reduced factor q[S(q) -1] data.

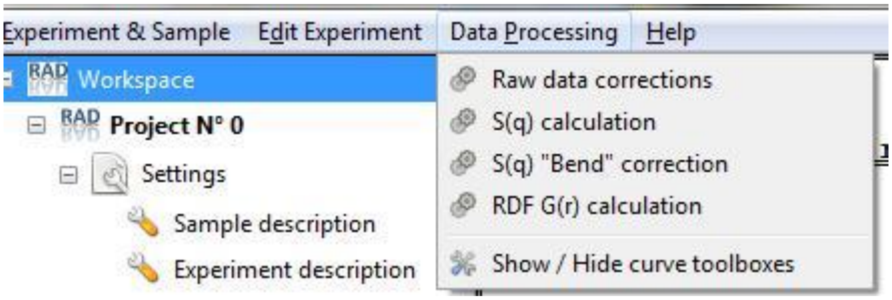

To do it the user should activate the option “*RDF G(r) calculation*” from the drop-down menu list of “*Data processing*” RAD_2 main window (see above) and enter the name of the file containing q[S(q) -1] data: (file *GdAl.qsq* in our example, see below). Alternatively, the User may decide to directly use the q[S(q)-1] data computed in the previous step “S(q) calculation” (by selecting option “Use calculated q[S(q)-1] data”; see below) since that q[S(q)-1] is still in the computer memory. RAD_2 either reads the q[S(q)-1] data from a saved on disc file or directly uses q[S(q)-1] data resulted from

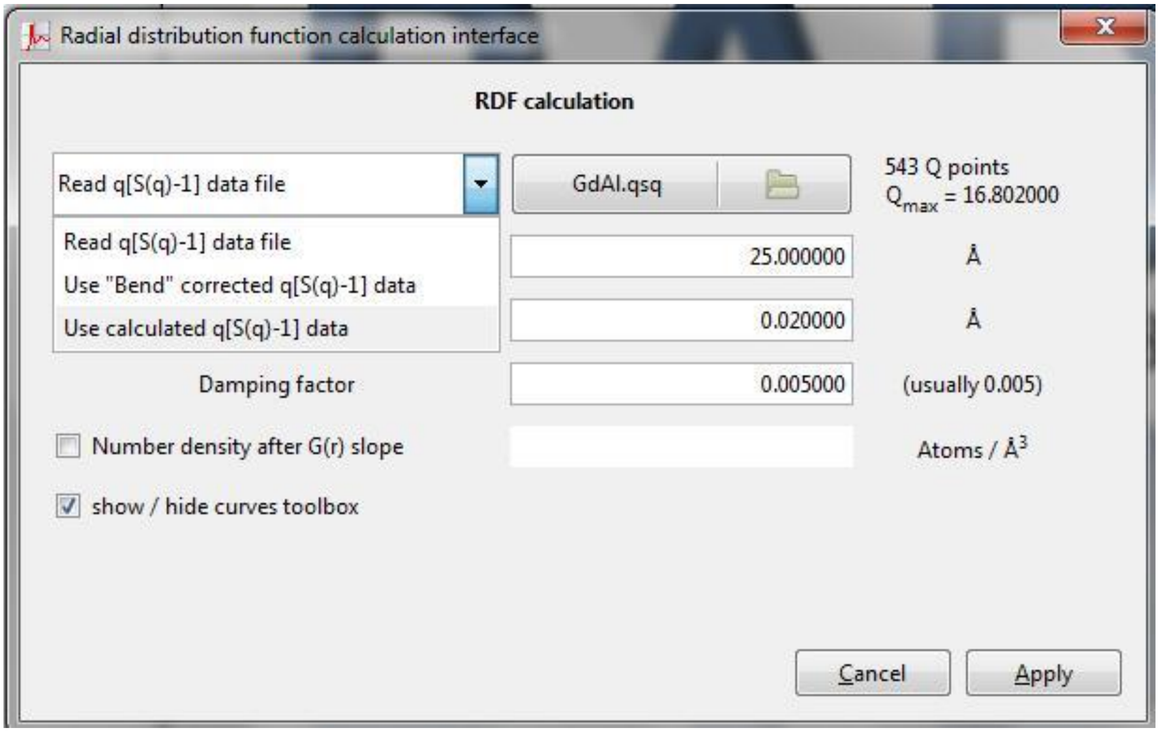

Radial distribution function calculation interface

RDF calculation

Read q[S(q)-1] data file: GdAl.qsq

543 Q points

Q_{max} = 16.802000

25.000000 Å

0.020000 Å

Damping factor: 0.005000 (usually 0.005)

☐ Number density after G(r) slope — Atoms / $Å^3$

☑ show / hide curves toolbox

The just performed steps “S(q) calculation” or “Bend corrected q[S(q)-1] data”. The “Bend” correction is explained later on in this manual. In the example here RAD_2 reads the q[S(q)-1] data and reports that it has 543 data points, the last one being at Q_{max} = 16.802 $Å^{-1}$ (see above). Then the User instructs RAD_2 to compute G(r) up to 25 Å in steps of 0.02 Å using a moderate damping factor (0.005) to outweigh higher-q data points since those are (very often) somewhat noisy. Then the User hit(s) “*Apply*” and the atomic PDF/RDF is computed. To view it the User selects “G(r)” option from the “*Tool box*” window (see below).

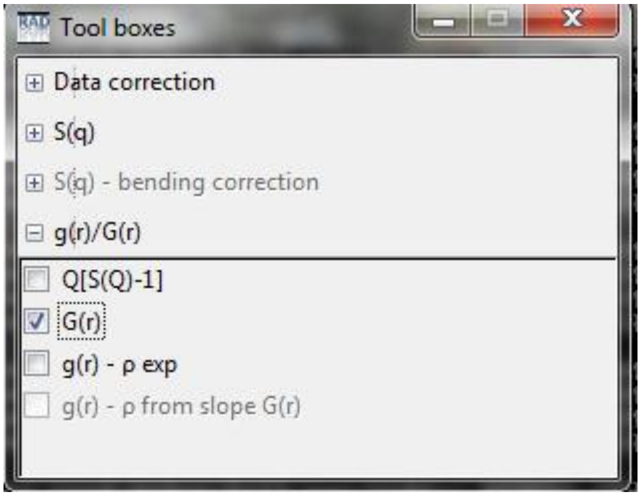

☐ Q[S(Q)-1]
☑ G(r)
☐ g(r) - ρ exp
☐ g(r) - ρ from slope G(r)

The so derived PDF/RDF G(r) data appear on the screen as shown below.

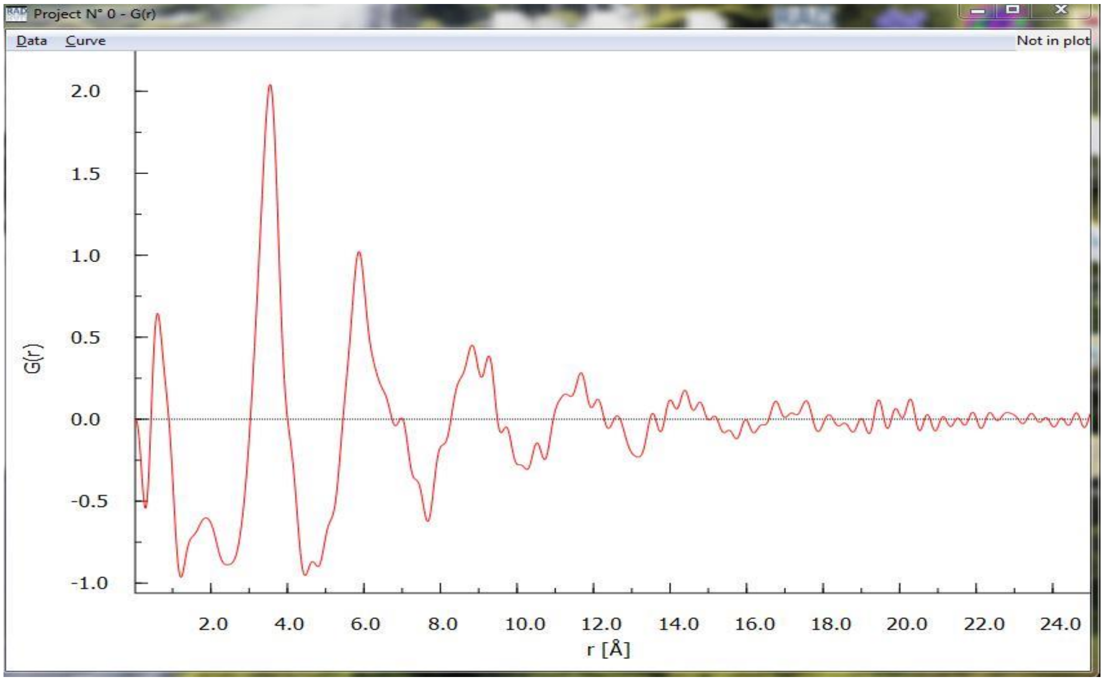

This PDF/RDF G(r) shows a strong unphysical ripple close to r ~ 0 Å but, in general, is of pretty good quality for a PDF/RDF obtained on an in-house XRD equipment back in 1988 ! The G(r) has its first physically sensible peak positioned at about 3.54 Å (Gd-Gd first atomic neighbor distance) and shows physical oscillations up to about 15-20 Å. This real-space distance may be viewed as a length of structural coherence in the bulk metallic glasses studied in this example. The high-frequency ripples above 20 Å are data noise.

Here the User has an option to compute the so-called pair correlation function g(r) as well. He/she may use either the "experimental" value for the atomic number density ρ_o stored in the “*RAD project file*” (usually a more correct approach) or use an estimate for ρ_o computed after the low-r slope of G(r) [2,3]. The latter option is activated by checking the corresponding box in the “*RDF calculation”* window. The correlation function g(r) computed using the experimental value of ρ_o = 0.03920 atoms/Å we entered in the *RAD project file* is shown below.

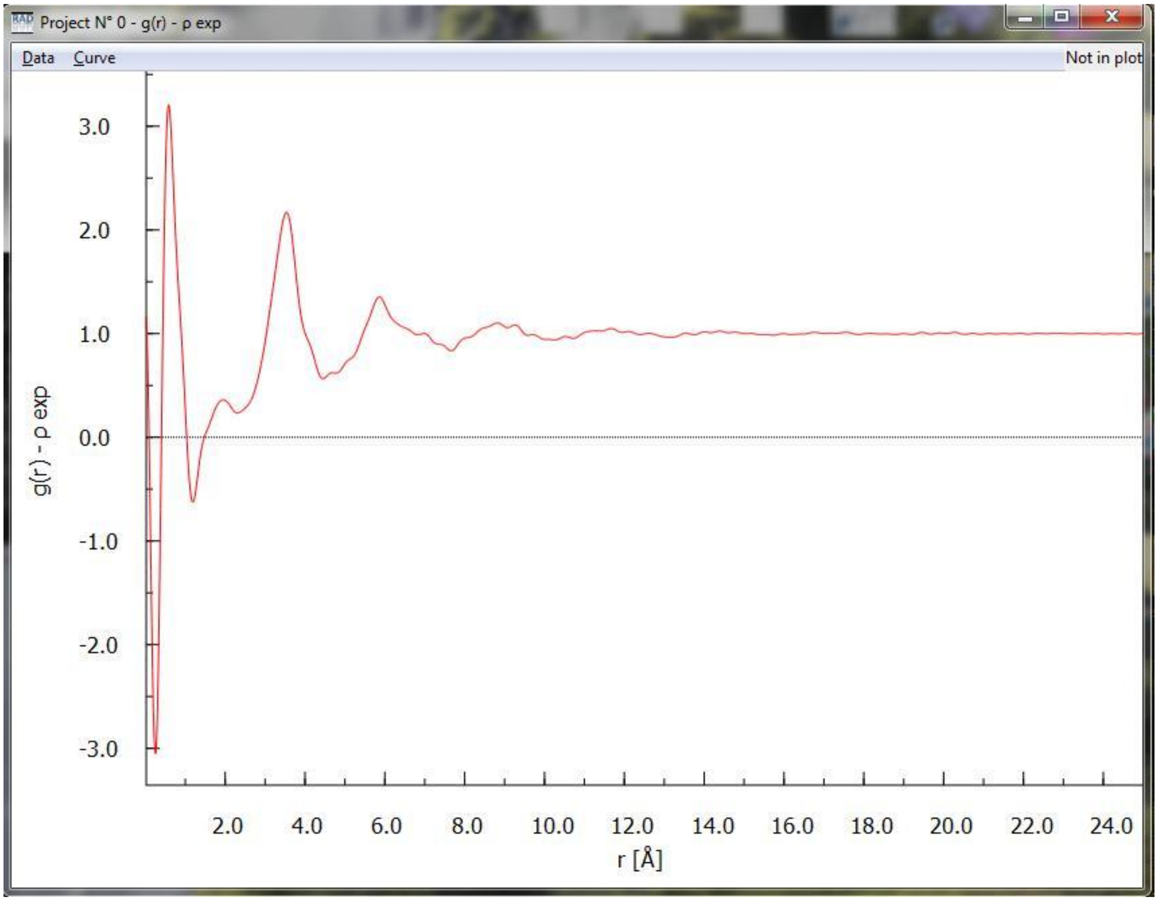

This g(r) shows a strong unphysical peak at distances below 1 Å but, otherwise, is of pretty good quality. Note, **as it should be, g(r) oscillates around one while the corresponding G(r) – around zero** (see below).

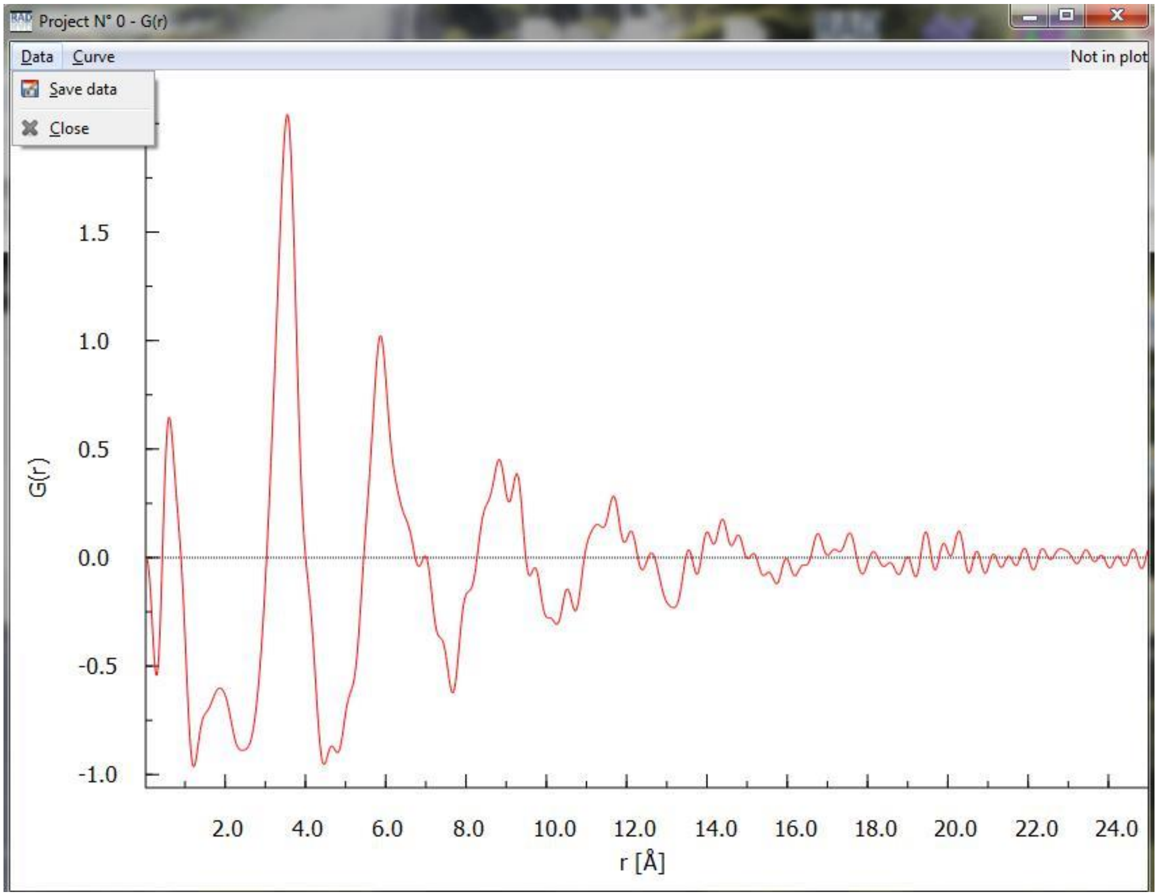

By checking the "*Data*" option in the upper left corner in the "*Data plotting window*" (see above) the User can save the G(r) data shown in this window in (x,y) ascii or (x,y,0,1) ascii format. We saved the G(r) data in a file named GdAl.rdf. **Note, the only way to save RAD's computed quantities (i.e. corrected XRD data, S(q), q[S(q)-1], G(r) or g(r) data) is i) first to display the respective data set in the "*Data plotting window*", ii) view it iii) and, if satisfied, save it using the "*Save Data*" option. RAD_2 will NOT save anything unless it is "told" to do so.**

Help option of RAD_2:

Provides general and contact info about RAD_2 and its authors (see below):

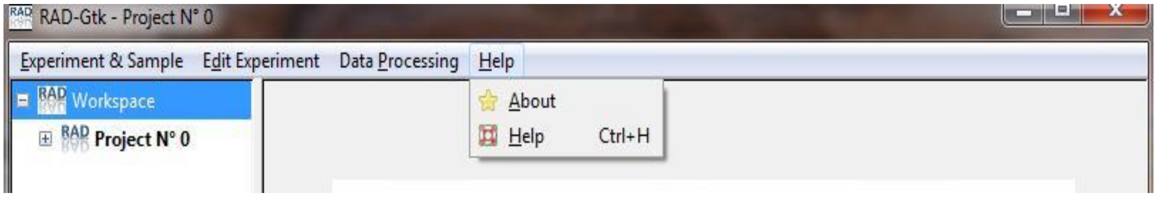

Analyzing multiple data sets (i.e. temperature, pressure etc. series):

Once a "*RAD project file*" is created/loaded users may process, one after another, several data sets from the same sample re-using the RAD_2 control (i.e. *Data processing*) parameters they entered/used for the first data set. Any subsequent data set (be it raw XRD data, corrected XRD data or q[S(q)-1] data), however, should have the same number of data points, including the same starting and ending 2θ/q values and Δq steps as the very first data set. If not RAD_2 may behave unpredictably.

More examples of RAD_2 usage:

The current RAD_2 version comes with two more examples. One describes processing of synchrotron XRD data for $In_{0.33}Ga_{0.67}As$ semiconductor. The study has been published in Petkov et al. *PRL* 83 (1999) p. 4089 (a copy of the paper is attached to this Manual). Here we provide the raw experimental data: "InGaAs.th", the RAD project file (in xml format) "InGaAs.rpf", the corrected XRD data: "InGaAs.cor", the reduced structure function data: "InGaAs.qsq" and the computed G(r): "InGaAs.rdf". An energy sensitive (Ge solid state) detector has been used in this study which had resulted in negligible background scattering – so no data for background/air scattering is provided. Also, thanks to the usage of a solid state Ge detector the Compton scattering has been eliminated from the XRD data during data collection (see below that the option to be selected in such cases is Compton "*All out*").

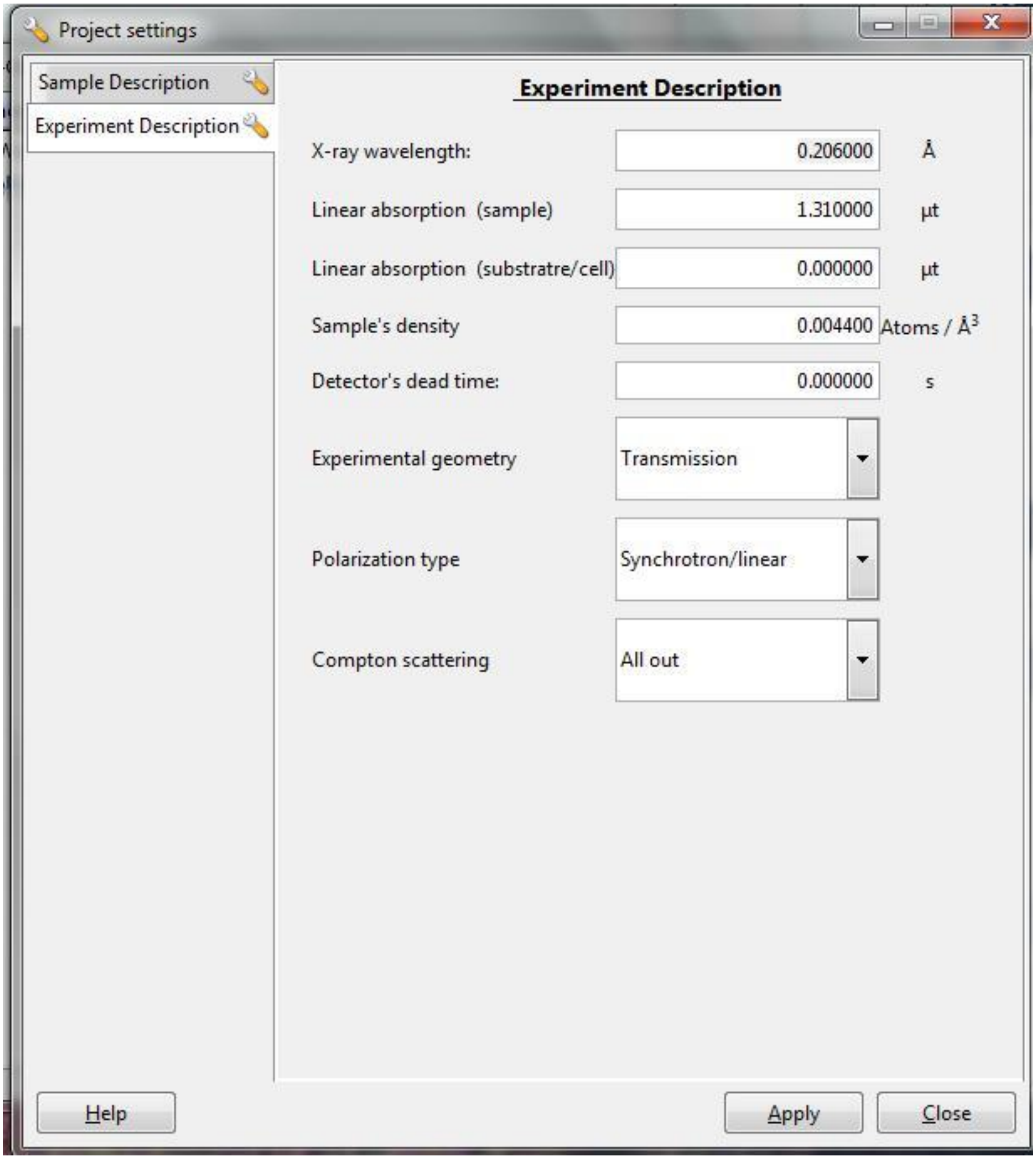

Experiment Description

X-ray wavelength:	0.206000	Å
Linear absorption (sample)	1.310000	μt
Linear absorption (substratre/cell)	0.000000	μt
Sample's density	0.004400	Atoms / Å^3
Detector's dead time:	0.000000	s
Experimental geometry	Transmission	
Polarization type	Synchrotron/linear	
Compton scattering	All out	

Users may start RAD_2, import the existing project (xml) file: "InGaAs.rpf", and look over the sample/experimental set-up information provided in it. Some of this info is shown above. In this example the step "*Raw data corrections*" is trivial and we skip it. Here we will demonstrate the next step - the derivation of [S(q)-1]; see below. RAD_2 reads the corrected data: "InGaAs.cor" from file or, alternatively, may use the just computed in step “Raw data correction” I(q) data set sine it is still in the computer memory (Option “Use corrected Q data”; see below). User then hits “*Apply*”.

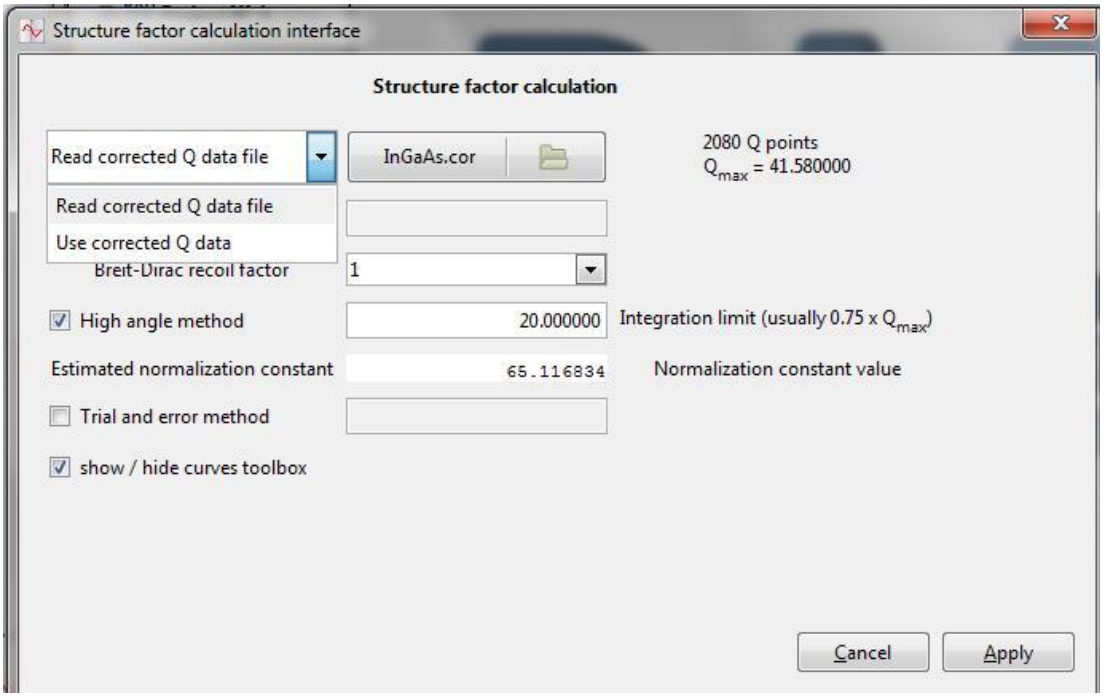

Read corrected Q data file
- Read corrected Q data file
- Use corrected Q data

InGaAs.cor

2080 Q points
Q_{max} = 41.580000

Breit-Dirac recoil factor: 1

☑ High angle method: 20.000000 Integration limit (usually 0.75 x Q_{max})

Estimated normalization constant: 65.116834 Normalization constant value

☐ Trial and error method

☑ show / hide curves toolbox

The corresponding [(S(q)-1] looks quite good to very high wave vectors of about 40 Å^{-1}; (see below) and we save it in a file “InGaS.qsq”.

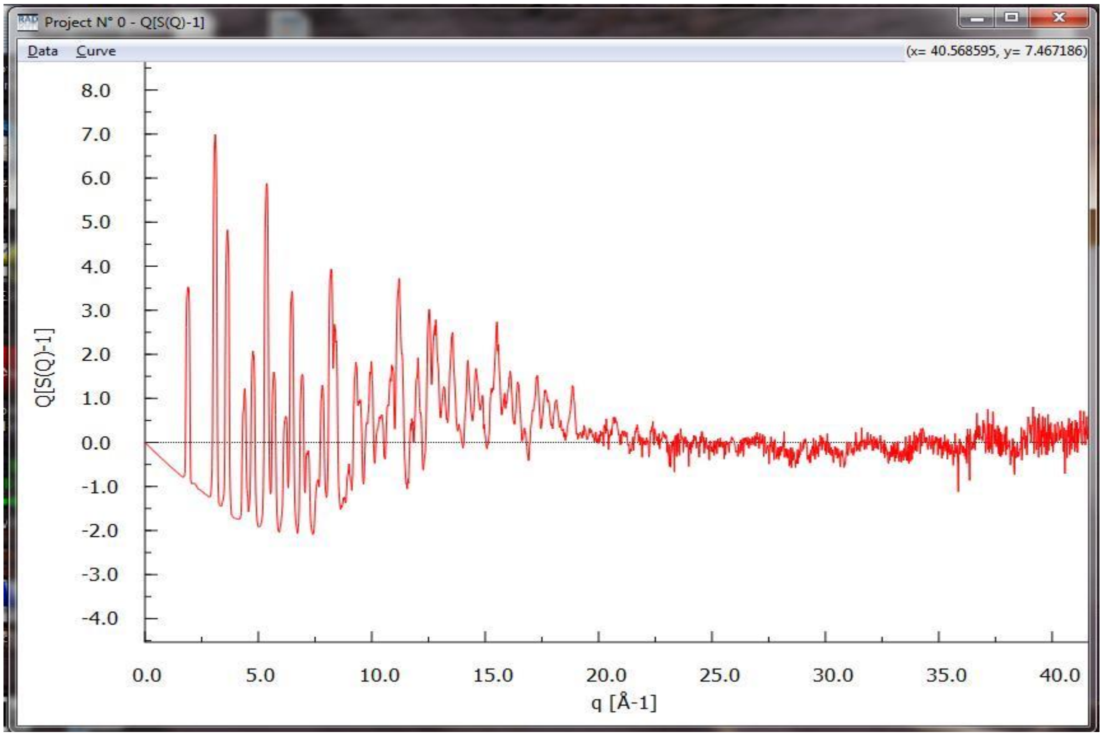

Then anatomic PDF/RDF can be computed from it in the way shown below:

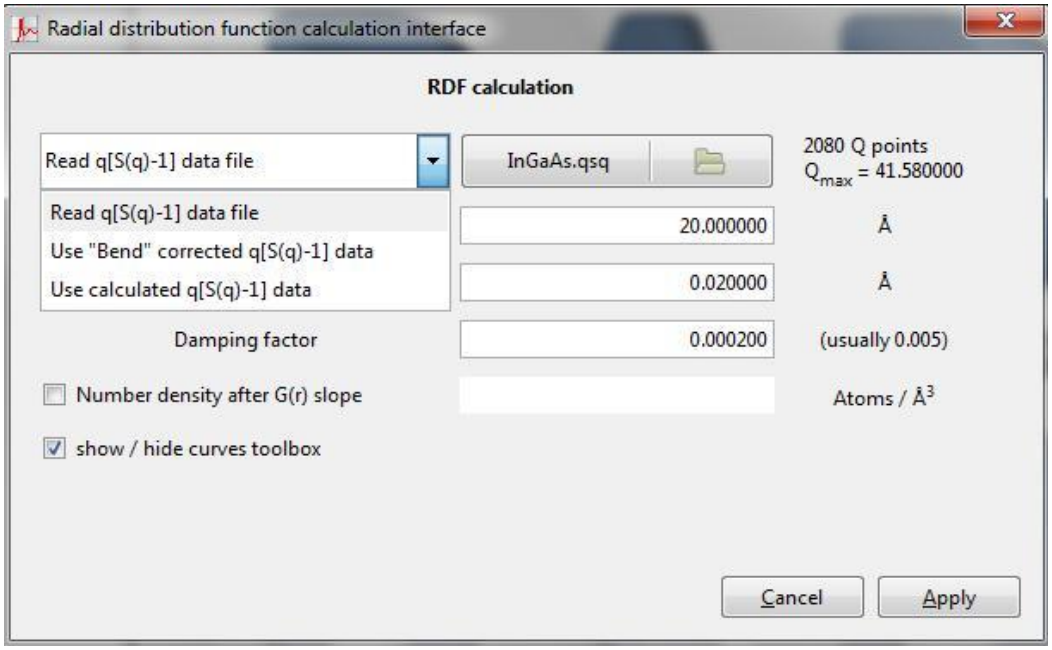

Read q[S(q)-1] data file — InGaAs.qsq

2080 Q points

Q_{max} = 41.580000

20.000000 Å

0.020000 Å

Damping factor 0.000200 (usually 0.005)

☐ Number density after G(r) slope — Atoms / Å^3

☑ show / hide curves toolbox

The G(r) shows very fine structural features of $In_{0.33}Ga_{0.67}As$. In particular, the first PDF/RDF peak is split into two subcomponents, positioned at approx. 2.4 Å and 2.6 Å, respectively (see below). They correspond to the presence of distinct Ga-As and In-As bonds in this material. More details can be found in the attached to this manual PRL paper.

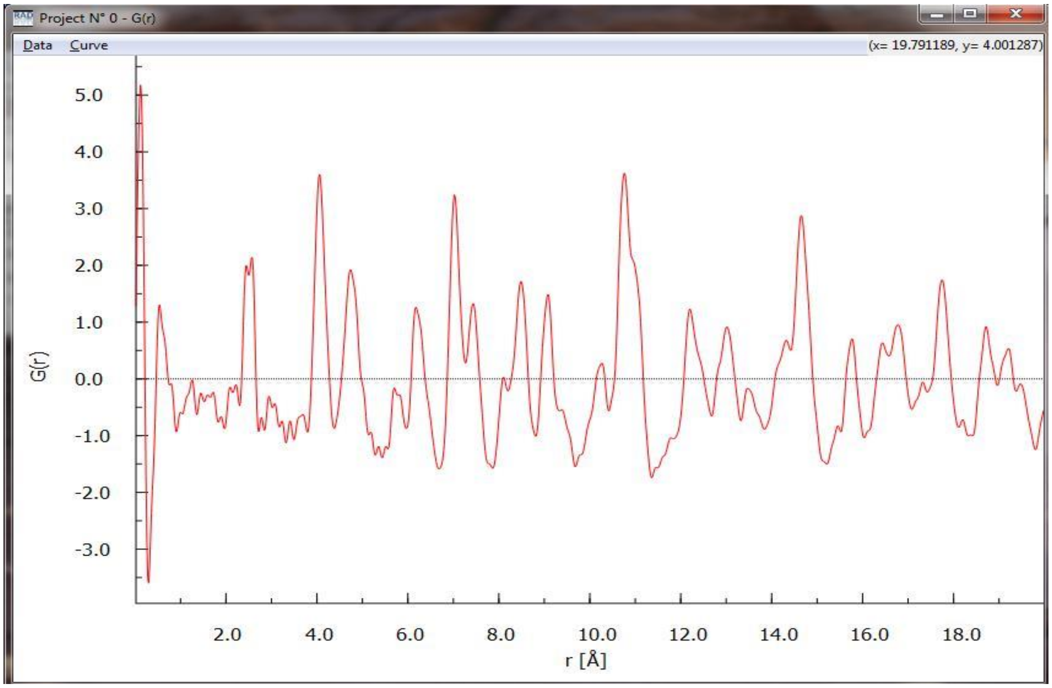

The other example highlights a processing of synchrotron XRD data for $SrTiO_3$ nanosized particles. Results from this study are published in V. Petkov et al. *Chem. Mat*. **18** (2006) p.814 (a copy of the paper is attached to this Manual). Here we provide the raw experimental data: “$SrTiO_3$.th”, the background scattering data: “Kapton.th”, the RAD_2 project (xml) file: “$SrTiO_3$.rpf”, the corrected XRD data: “$SrTiO_3$.cor”, the reduced structure function data: “$SrTiO_3$.qsq” and the computed G(r): “$SrTiO_3$.rdf”. A large area (mar345) detector has been used in this study. Since large area detectors are not x-ray energy sensitive the raw XRD data contains a considerable contribution from Compton scattering (option Compton “*All in*”; see below).

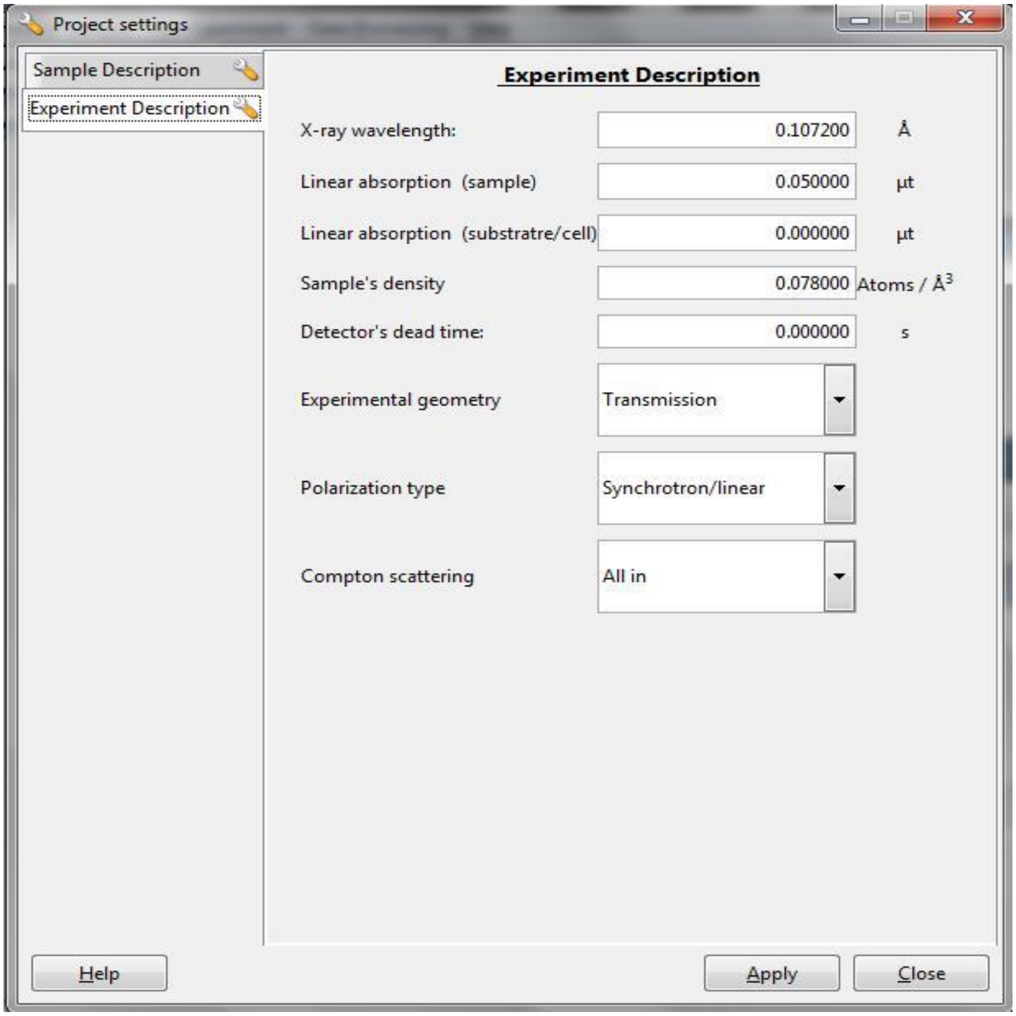

Experiment Description

X-ray wavelength: 0.107200 Å
Linear absorption (sample) 0.050000 μt
Linear absorption (substratre/cell) 0.000000 μt
Sample's density 0.078000 Atoms / $Å^3$
Detector's dead time: 0.000000 s
Experimental geometry Transmission
Polarization type Synchrotron/linear
Compton scattering All in

Users may start RAD_2, open the existing (xml) project file: “$SrTiO_3$.rpf”, and look over the sample/experimental set-up information provided in it. Some of this info is shown above. The step “*Raw data corrections*” is trivial and we again skip it. Here we will demonstrate the next step - the derivation of q[S(q)-1]; see below. RAD_2 reads the corrected data: “$SrTiO_3$.cor” or, alternatively, uses the just computed in step “Raw data correction” I(q) data set since it is still in the computer memory (Option “Use corrected Q data”; see below). At first the User may run the “high-angle” normalization method to obtain a reasonable estimate for the normalization constant (by hitting “Apply” button).

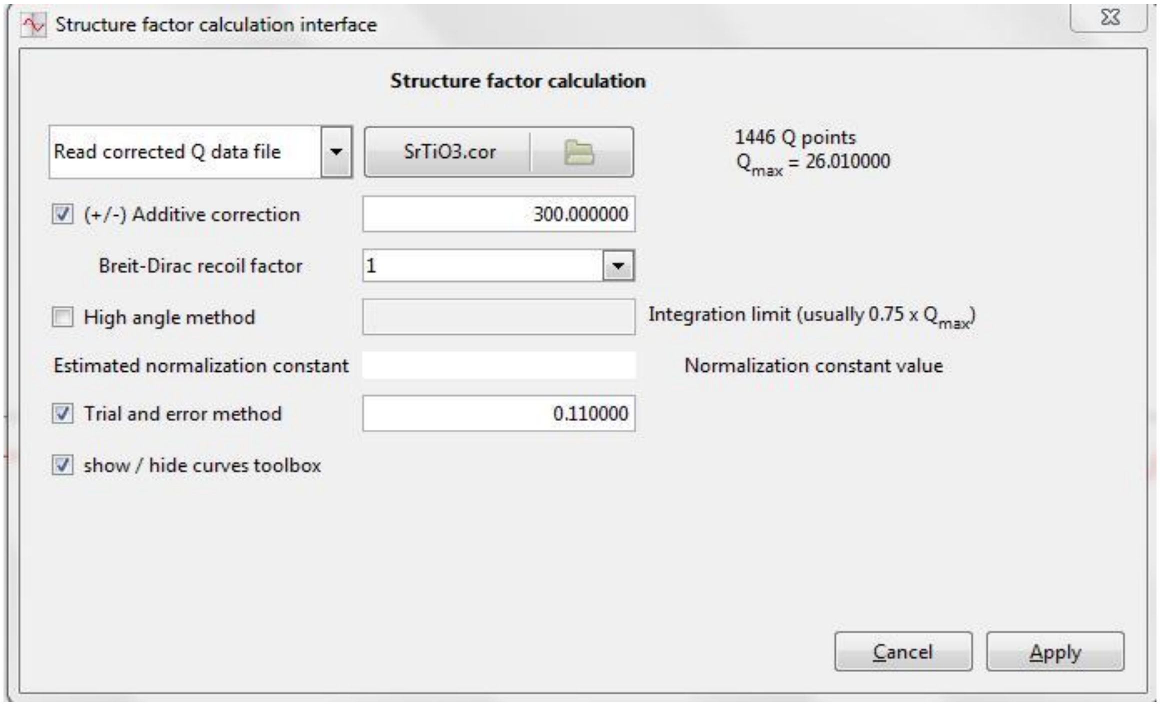

Structure factor calculation interface

Structure factor calculation

Read corrected Q data file: SrTiO3.cor

1446 Q points
Q_{max} = 26.010000

☑ (+/-) Additive correction: 300.000000

Breit-Dirac recoil factor: 1

☐ High angle method

Integration limit (usually 0.75 x Q_{max})

Estimated normalization constant

Normalization constant value

☑ Trial and error method: 0.110000

☑ show / hide curves toolbox

The originally obtained q[S(q)-1], however does not show a reasonable behavior (i.e. it does not oscillate about zero) so the User may continue in a “trial and error” mode to obtain as good a normalization constant and q[S(q)-1] data as possible. Here we “find” that an additional additive correction (300 !) and a normalization constant of 0.11 help a bit. The respective q[S(q)-1] is given in the plot below. This q[S(q)-1] behaves well up to q-values of about 14 Å^{-1} but then shows an unphysical downturn, mostly due to an improper Compton scattering correction. Users may often see a similar unphysical behavior of their q[S(q)-1)] data. Possible solutions: re-doing the data corrections from the very beginning, looking into the sample thickness/absorption correction and background scattering, collecting the data one more time using another detector etc. may help a bit. If none of the above works we may still save the badly behaving q(S(Q-1) data. We saved it in a file “SrTiO3.qsq”.

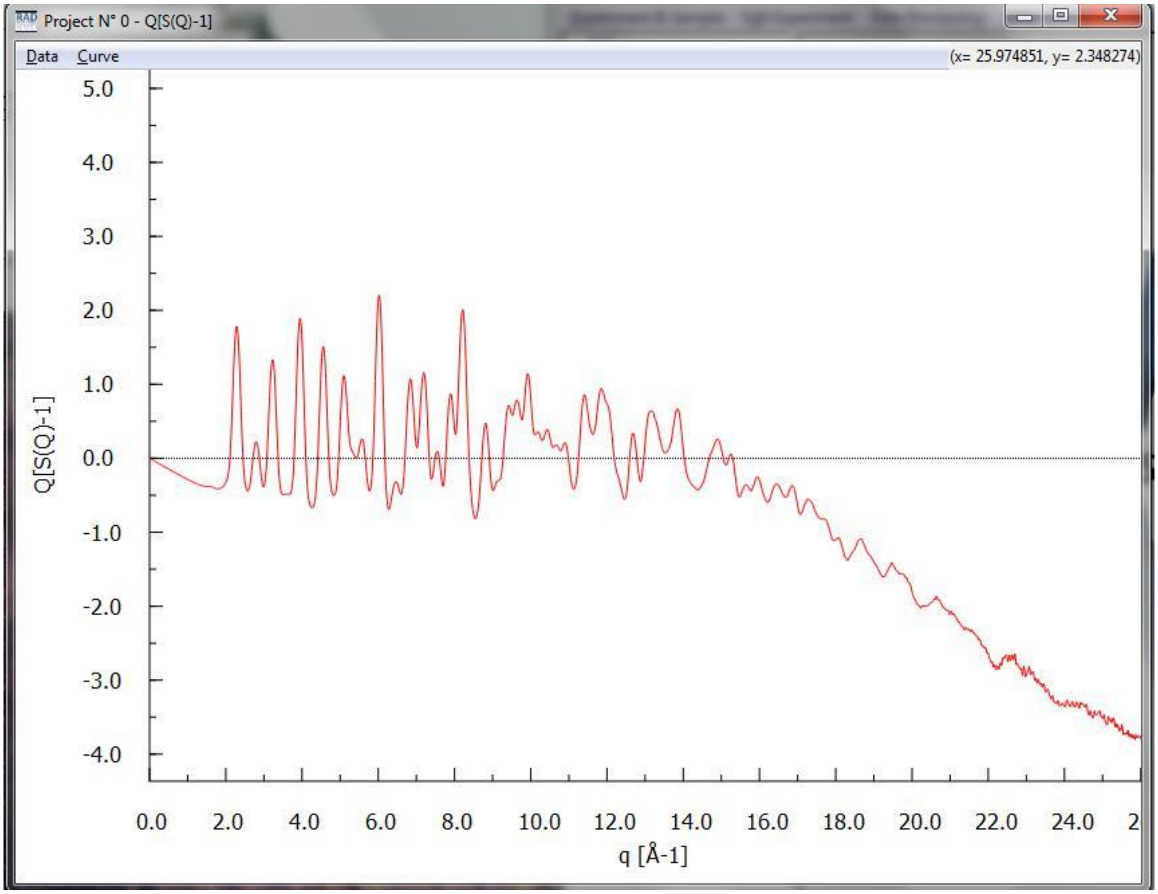

User's: do NOT use distorted/misbehaving/not-oscillating around zero etc. q[S(q)-1] data sets. If you do it the quality of the respective PDF/RDF data may be compromised very seriously. Some extra PDF/RDF quality checks as described in ref. [8] can help estimate the quality of your data.

To help in cases when the reduced structure function q[S(q)-1] data shows an unphysical up or down turn **at high-Q values** (as seen in the plot above) a special correction procedure S*(q) "Bend" Correction* is introduced in RAD_2.

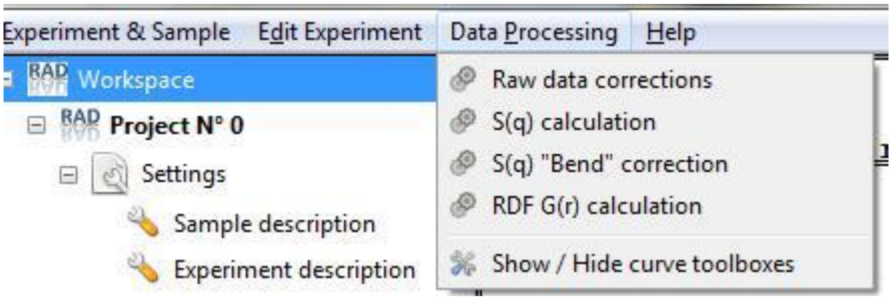

This procedure is a part of the "*Data Processing Menu*" of RAD_2 (see above). Once selected the user has to decide to use data saved on disc "e.g. file $SrTiO_3$.cor" or, alternatively, use the just computed q[S(q)-1] data that are still in computer memory. (Option "Use calculated q[S(q)-1] data"; see below). Then the User has to provide an estimate for **the high q value** at which the q[S(q)-1] function starts "bending away" from zero. In our case it is at about 14 A^{-1}. After applying the "bending" correction the behavior of the q(S(q)-1) is improved substantially (see below):

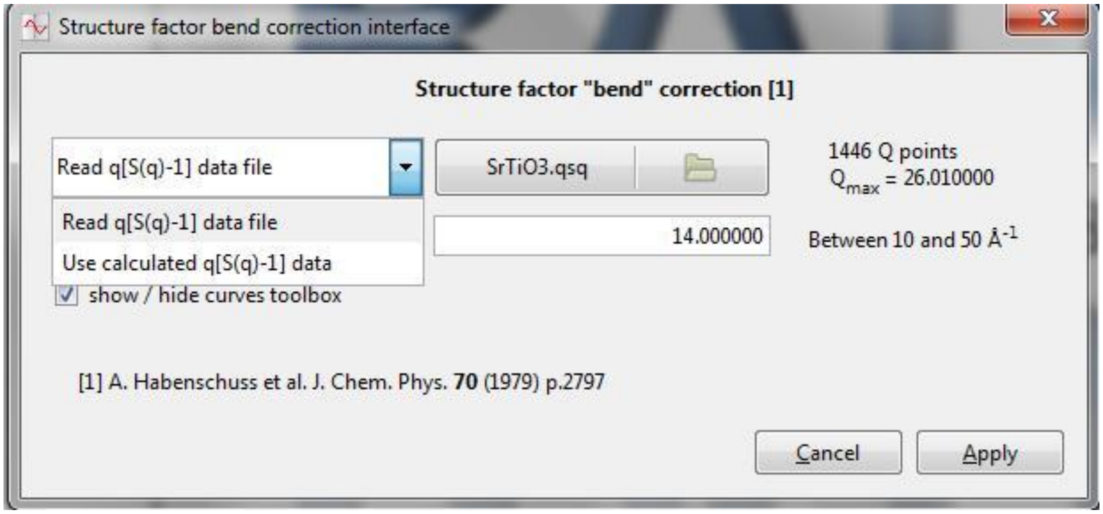

Structure factor "bend" correction [1]

SrTiO3.qsq

1446 Q points

Q_{max} = 26.010000

14.000000

Between 10 and 50 $Å^{-1}$

☑ show / hide curves toolbox

[1] A. Habenschuss et al. J. Chem. Phys. **70** (1979) p.2797

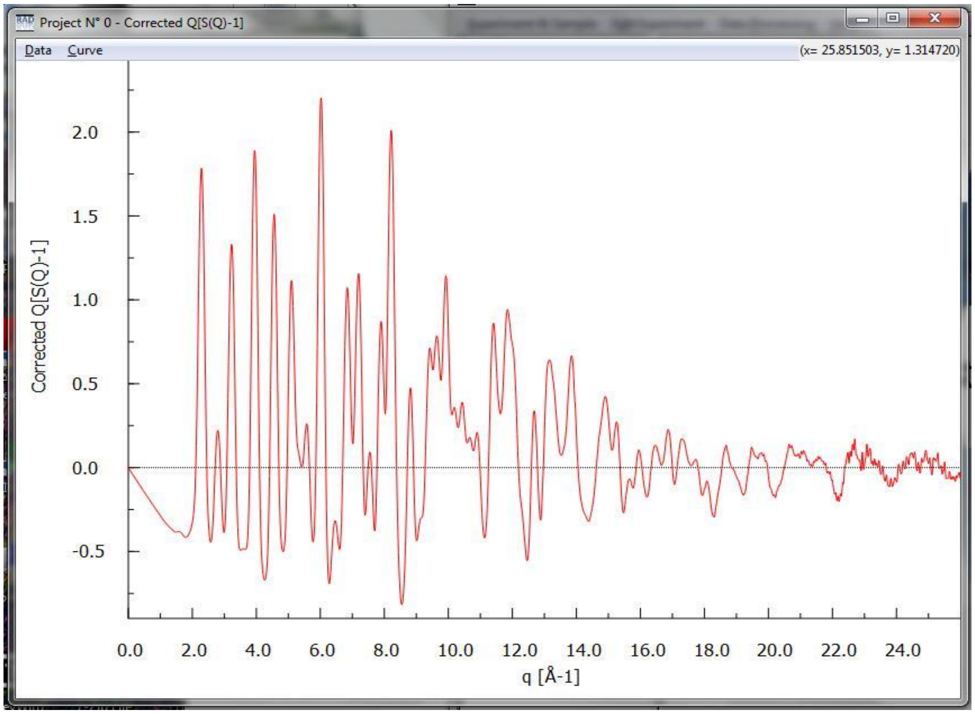

We save the so corrected q[S(q)-1] data in a file “$SrTiO_3$.rif” and use it to compute the respective atomic PDF G(r) as described below:

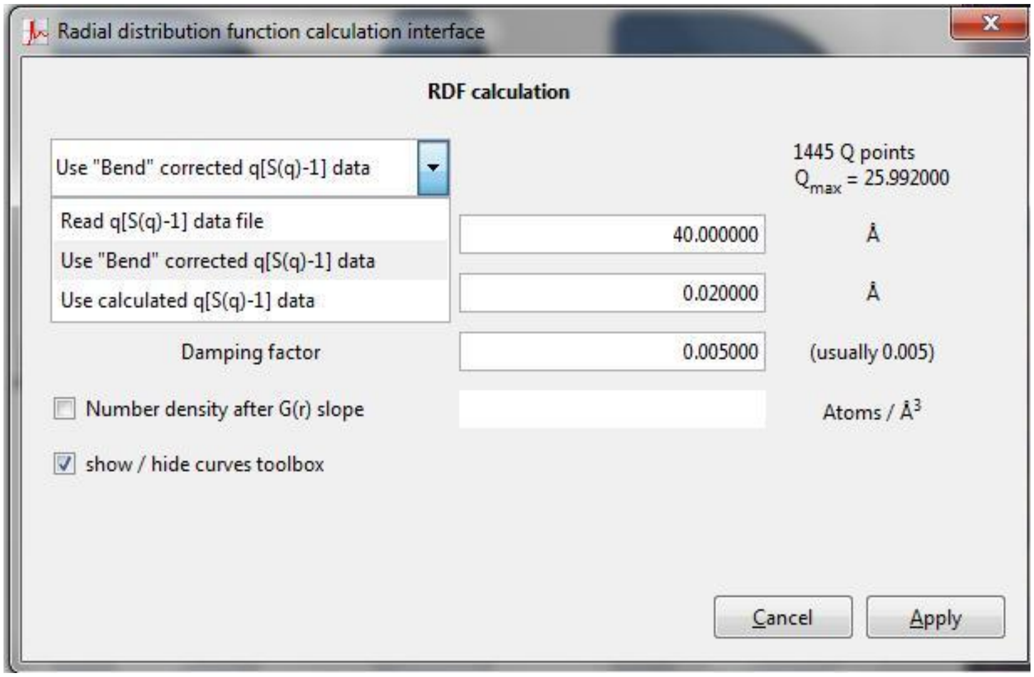

RDF calculation

Use "Bend" corrected q[S(q)-1] data

Read q[S(q)-1] data file
Use "Bend" corrected q[S(q)-1] data
Use calculated q[S(q)-1] data

1445 Q points
Q_{max} = 25.992000

40.000000 Å
0.020000 Å
Damping factor 0.005000 (usually 0.005)
☐ Number density after G(r) slope Atoms / $Å^3$
☑ show / hide curves toolbox

The resulted G(r) is of pretty good quality (see below).

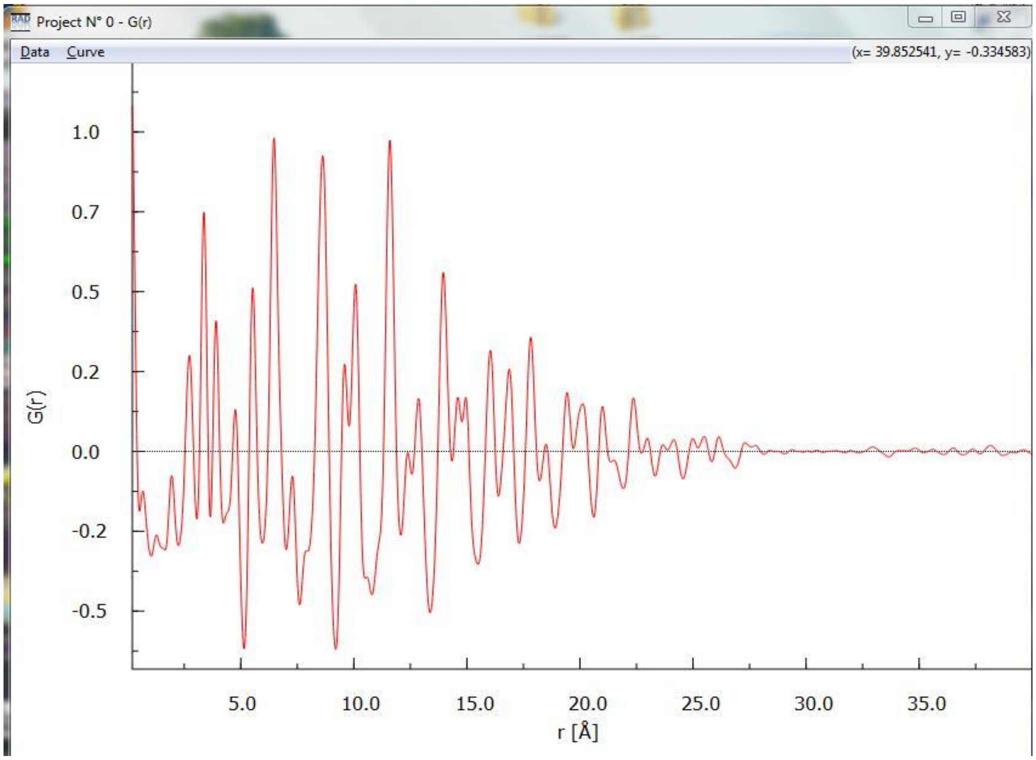

The examples above are just a glimpse of what RAD_2 Users may face in real life. Indeed atomic PDF/RDF analysis is not so difficult as it looks in first sight. Sure some time and persistence are necessary to become a successful RAD_2 User. But isn’t it the same with any real life endeavor ?

Good luck !

References:

[1] C. Giacovazzo et al., in “*Fundamentals of x-ray crystallography*”, (Oxford University Press, 1998).

[2] H.P. Klug and L.E. Alexander, in “*X-ray diffraction procedures for polycrystalline and amorphous materials*”, (John Wiley & Sons, 1974); T. Egami and S.J.L. Billinge in “*Underneath the Bragg peaks”* (Pergamon Press, Amsterdam, **2003**); V. Petkov *Maerials Today* **11** (2008) 28.

[3] D. A. Keen *J. Appl. Cryst*. **34** (2001) 172.

[4] B. Toby and T. Egami *Acta Cryst*. A **48** (1992) 336.

[5] P.J. Chupas et al. *J. Appl. Cryst*. **40** (2007) 463.

[6] V. Petkov et al**.** *Phys. Rev. Lett***.** **83** (1999) 4089.

[7] E. Curis and S. Benazeth, *J. Synchrotron Rad*. **7** (2000) 262.

[8] V. Petkov and R. Danev, *J. Appl. Cryst* . **31** (1998) 609.

Appendix 1:

Periodic Table of the Elements

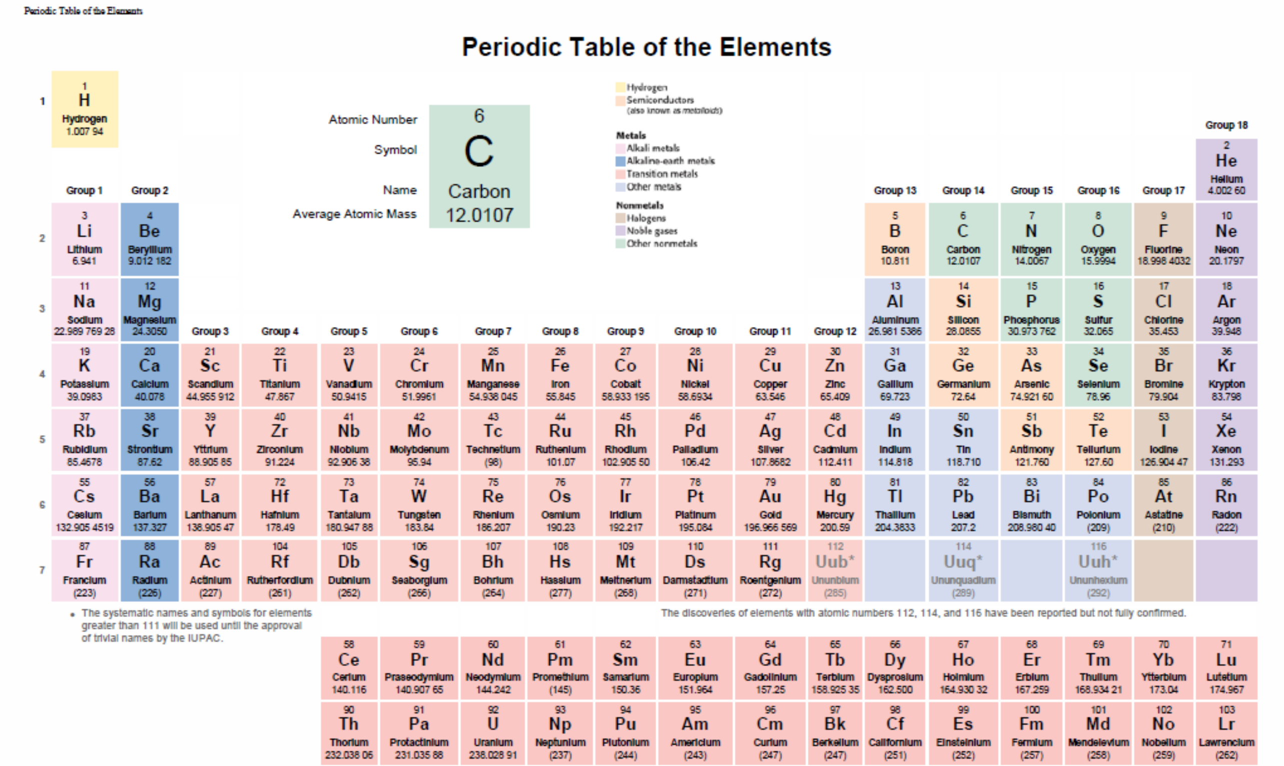

Periodic Table of the Elements

Periodic Table of the Elements

Atomic Number 6
Symbol C
Name Carbon
Average Atomic Mass 12.0107

■ Hydrogen
■ Semiconductors
(also known as *metalloids*)

Metals
■ Alkali metals
■ Alkaline-earth metals
■ Transition metals
■ Other metals

Nonmetals
■ Halogens
■ Noble gases
■ Other nonmetals

	Group 1	Group 2	Group 3	Group 4	Group 5	Group 6	Group 7	Group 8	Group 9	Group 10	Group 11	Group 12	Group 13	Group 14	Group 15	Group 16	Group 17	Group 18
1	1 H Hydrogen 1.007 94																	2 He Helium 4.002 60
2	3 Li Lithium 6.941	4 Be Beryllium 9.012 182											5 B Boron 10.811	6 C Carbon 12.0107	7 N Nitrogen 14.0067	8 O Oxygen 15.9994	9 F Fluorine 18.998 4032	10 Ne Neon 20.1797
3	11 Na Sodium 22.989 769 28	12 Mg Magnesium 24.3050											13 Al Aluminum 26.981 5386	14 Si Silicon 28.0855	15 P Phosphorus 30.973 762	16 S Sulfur 32.065	17 Cl Chlorine 35.453	18 Ar Argon 39.948
4	19 K Potassium 39.0983	20 Ca Calcium 40.078	21 Sc Scandium 44.955 912	22 Ti Titanium 47.867	23 V Vanadium 50.9415	24 Cr Chromium 51.9961	25 Mn Manganese 54.938 045	26 Fe Iron 55.845	27 Co Cobalt 58.933 195	28 Ni Nickel 58.6934	29 Cu Copper 63.546	30 Zn Zinc 65.409	31 Ga Gallium 69.723	32 Ge Germanium 72.64	33 As Arsenic 74.921 60	34 Se Selenium 78.96	35 Br Bromine 79.904	36 Kr Krypton 83.798
5	37 Rb Rubidium 85.4678	38 Sr Strontium 87.62	39 Y Yttrium 88.905 85	40 Zr Zirconium 91.224	41 Nb Niobium 92.906 38	42 Mo Molybdenum 95.94	43 Tc Technetium (98)	44 Ru Ruthenium 101.07	45 Rh Rhodium 102.905 50	46 Pd Palladium 106.42	47 Ag Silver 107.8682	48 Cd Cadmium 112.411	49 In Indium 114.818	50 Sn Tin 118.710	51 Sb Antimony 121.760	52 Te Tellurium 127.60	53 I Iodine 126.904 47	54 Xe Xenon 131.293
6	55 Cs Cesium 132.905 4519	56 Ba Barium 137.327	57 La Lanthanum 138.905 47	72 Hf Hafnium 178.49	73 Ta Tantalum 180.947 88	74 W Tungsten 183.84	75 Re Rhenium 186.207	76 Os Osmium 190.23	77 Ir Iridium 192.217	78 Pt Platinum 195.084	79 Au Gold 196.966 569	80 Hg Mercury 200.59	81 Tl Thallium 204.3833	82 Pb Lead 207.2	83 Bi Bismuth 208.980 40	84 Po Polonium (209)	85 At Astatine (210)	86 Rn Radon (222)
7	87 Fr Francium (223)	88 Ra Radium (226)	89 Ac Actinium (227)	104 Rf Rutherfordium (261)	105 Db Dubnium (262)	106 Sg Seaborgium (266)	107 Bh Bohrium (264)	108 Hs Hassium (277)	109 Mt Meitnerium (268)	110 Ds Darmstadtium (271)	111 Rg Roentgenium (272)	112 Uub* Ununbium (285)		114 Uuq* Ununquadium (289)		116 Uuh* Ununhexium (292)		
					58 Ce Cerium 140.116	59 Pr Praseodymium 140.907 65	60 Nd Neodymium 144.242	61 Pm Promethium (145)	62 Sm Samarium 150.36	63 Eu Europium 151.964	64 Gd Gadolinium 157.25	65 Tb Terbium 158.925 35	66 Dy Dysprosium 162.500	67 Ho Holmium 164.930 32	68 Er Erbium 167.259	69 Tm Thulium 168.934 21	70 Yb Ytterbium 173.04	71 Lu Lutetium 174.967
					90 Th Thorium 232.038 06	91 Pa Protactinium 231.035 88	92 U Uranium 238.028 91	93 Np Neptunium (237)	94 Pu Plutonium (244)	95 Am Americium (243)	96 Cm Curium (247)	97 Bk Berkelium (247)	98 Cf Californium (251)	99 Es Einsteinium (252)	100 Fm Fermium (257)	101 Md Mendelevium (258)	102 No Nobelium (259)	103 Lr Lawrencium (262)

- The systematic names and symbols for elements greater than 111 will be used until the approval of trivial names by the IUPAC.

The discoveries of elements with atomic numbers 112, 114, and 116 have been reported but not fully confirmed.

Appendix 2:

Dispersion corrections to the atomic scattering factors for x-rays

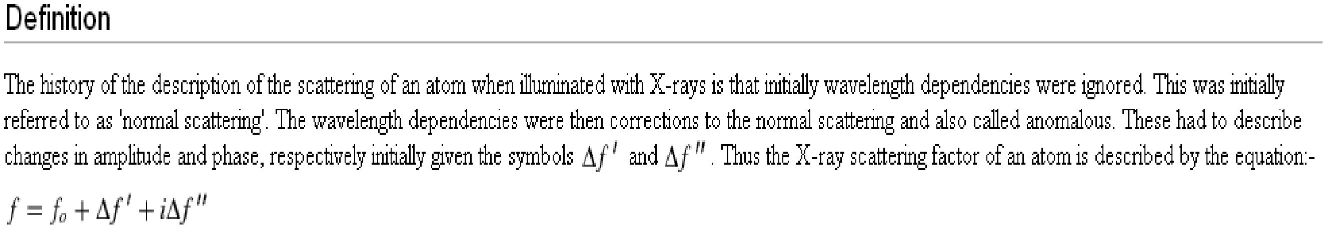

Definition

The history of the description of the scattering of an atom when illuminated with X-rays is that initially wavelength dependencies were ignored. This was initially referred to as 'normal scattering'. The wavelength dependencies were then corrections to the normal scattering and also called anomalous. These had to describe changes in amplitude and phase, respectively initially given the symbols $\Delta f'$ and $\Delta f''$. Thus the X-ray scattering factor of an atom is described by the equation:-

$$f = f_o + \Delta f' + i\Delta f''$$

Below are Δf” and Δf” anomalous dispersion corrections for Mo Ka and Ag Ka radiation after D. Cromer *Acta Cryst*. **18** (1965) p. 17. Note Δf” and Δf” are much smaller than f_o which is pretty close to Z, the atomic number of the respective atomic species.

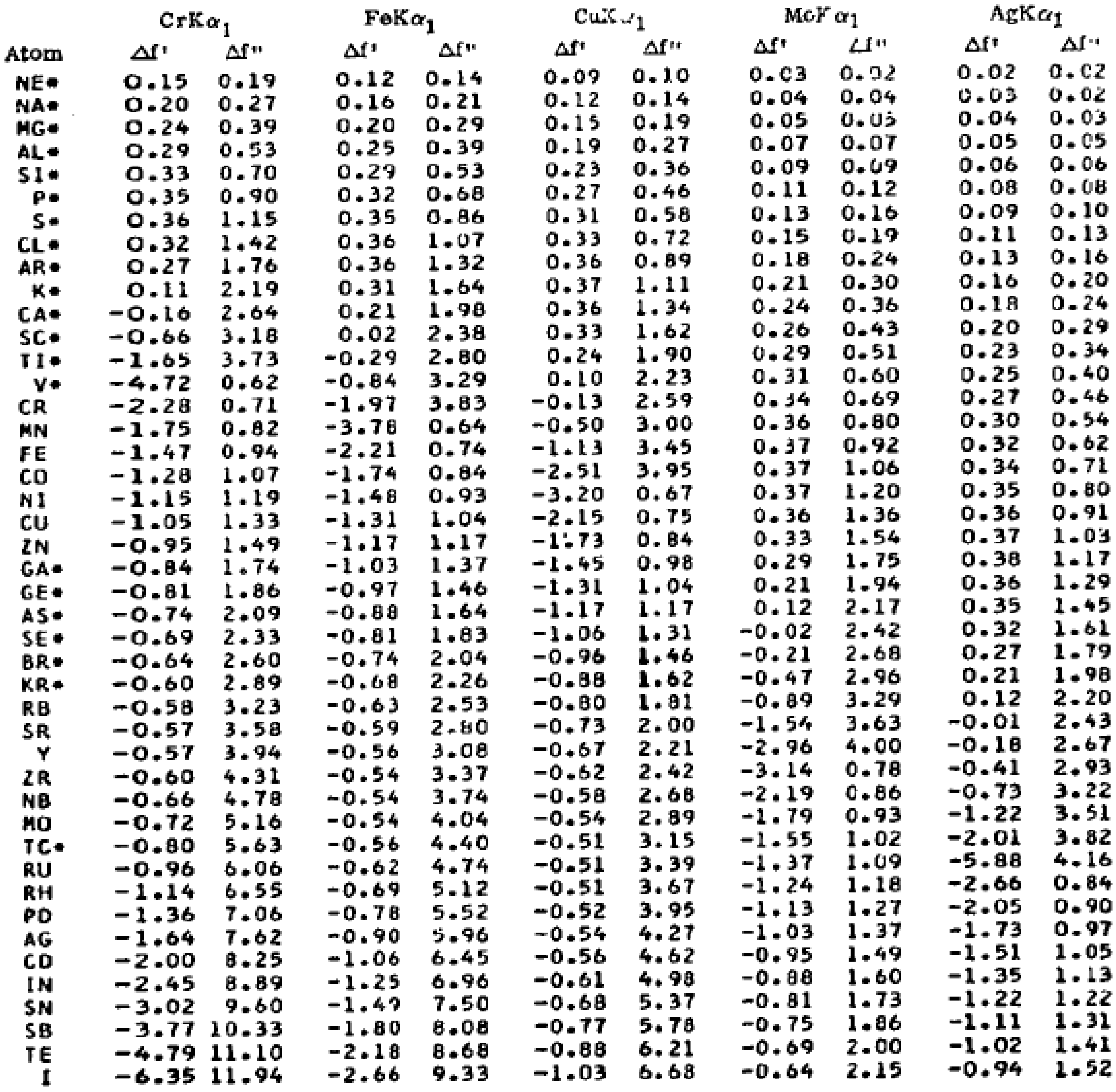

	$CrK\alpha_1$		$FeK\alpha_1$		$CuK\alpha_1$		$MoK\alpha_1$		$AgK\alpha_1$	
Atom	Δf'	Δf''	Δf'	Δf''	Δf'	Δf''	Δf'	Δf''	Δf'	Δf''
NE*	0.15	0.19	0.12	0.14	0.09	0.10	0.03	0.02	0.02	0.02
NA*	0.20	0.27	0.16	0.21	0.12	0.14	0.04	0.04	0.03	0.02
MG*	0.24	0.39	0.20	0.29	0.15	0.19	0.05	0.05	0.04	0.03
AL*	0.29	0.53	0.25	0.39	0.19	0.27	0.07	0.07	0.05	0.05
SI*	0.33	0.70	0.29	0.53	0.23	0.36	0.09	0.09	0.06	0.06
P*	0.35	0.90	0.32	0.68	0.27	0.46	0.11	0.12	0.08	0.08
S*	0.36	1.15	0.35	0.86	0.31	0.58	0.13	0.16	0.09	0.10
CL*	0.32	1.42	0.36	1.07	0.33	0.72	0.15	0.19	0.11	0.13
AR*	0.27	1.76	0.36	1.32	0.36	0.89	0.18	0.24	0.13	0.16
K*	0.11	2.19	0.31	1.64	0.37	1.11	0.21	0.30	0.16	0.20
CA*	−0.16	2.64	0.21	1.98	0.36	1.34	0.24	0.36	0.18	0.24
SC*	−0.66	3.18	0.02	2.38	0.33	1.62	0.26	0.43	0.20	0.29
TI*	−1.65	3.73	−0.29	2.80	0.24	1.90	0.29	0.51	0.23	0.34
V*	−4.72	0.62	−0.84	3.29	0.10	2.23	0.31	0.60	0.25	0.40
CR	−2.28	0.71	−1.97	3.83	−0.13	2.59	0.34	0.69	0.27	0.46
MN	−1.75	0.82	−3.78	0.64	−0.50	3.00	0.36	0.80	0.30	0.54
FE	−1.47	0.94	−2.21	0.74	−1.13	3.45	0.37	0.92	0.32	0.62
CO	−1.28	1.07	−1.74	0.84	−2.51	3.95	0.37	1.06	0.34	0.71
NI	−1.15	1.19	−1.48	0.93	−3.20	0.67	0.37	1.20	0.35	0.80
CU	−1.05	1.33	−1.31	1.04	−2.15	0.75	0.36	1.36	0.36	0.91
ZN	−0.95	1.49	−1.17	1.17	−1.73	0.84	0.33	1.54	0.37	1.03
GA*	−0.84	1.74	−1.03	1.37	−1.45	0.98	0.29	1.75	0.38	1.17
GE*	−0.81	1.86	−0.97	1.46	−1.31	1.04	0.21	1.94	0.36	1.29
AS*	−0.74	2.09	−0.88	1.64	−1.17	1.17	0.12	2.17	0.35	1.45
SE*	−0.69	2.33	−0.81	1.83	−1.06	1.31	−0.02	2.42	0.32	1.61
BR*	−0.64	2.60	−0.74	2.04	−0.96	1.46	−0.21	2.68	0.27	1.79
KR*	−0.60	2.89	−0.68	2.26	−0.88	1.62	−0.47	2.96	0.21	1.98
RB	−0.58	3.23	−0.63	2.53	−0.80	1.81	−0.89	3.29	0.12	2.20
SR	−0.57	3.58	−0.59	2.80	−0.73	2.00	−1.54	3.63	−0.01	2.43
Y	−0.57	3.94	−0.56	3.08	−0.67	2.21	−2.96	4.00	−0.18	2.67
ZR	−0.60	4.31	−0.54	3.37	−0.62	2.42	−3.14	0.78	−0.41	2.93
NB	−0.66	4.78	−0.54	3.74	−0.58	2.68	−2.19	0.86	−0.73	3.22
MO	−0.72	5.16	−0.54	4.04	−0.54	2.89	−1.79	0.93	−1.22	3.51
TC*	−0.80	5.63	−0.56	4.40	−0.51	3.15	−1.55	1.02	−2.01	3.82
RU	−0.96	6.06	−0.62	4.74	−0.51	3.39	−1.37	1.09	−5.88	4.16
RH	−1.14	6.55	−0.69	5.12	−0.51	3.67	−1.24	1.18	−2.66	0.84
PD	−1.36	7.06	−0.78	5.52	−0.52	3.95	−1.13	1.27	−2.05	0.90
AG	−1.64	7.62	−0.90	5.96	−0.54	4.27	−1.03	1.37	−1.73	0.97
CD	−2.00	8.25	−1.06	6.45	−0.56	4.62	−0.95	1.49	−1.51	1.05
IN	−2.45	8.89	−1.25	6.96	−0.61	4.98	−0.88	1.60	−1.35	1.13
SN	−3.02	9.60	−1.49	7.50	−0.68	5.37	−0.81	1.73	−1.22	1.22
SB	−3.77	10.33	−1.80	8.08	−0.77	5.78	−0.75	1.86	−1.11	1.31
TE	−4.79	11.10	−2.18	8.68	−0.88	6.21	−0.69	2.00	−1.02	1.41
I	−6.35	11.94	−2.66	9.33	−1.03	6.68	−0.64	2.15	−0.94	1.52

Atom	$CrK\alpha_1$ Δf'	$CrK\alpha_1$ Δf''	$FeK\alpha_1$ Δf'	$FeK\alpha_1$ Δf''	$CuK\alpha_1$ Δf'	$CuK\alpha_1$ Δf''	$MoK\alpha_1$ Δf'	$MoK\alpha_1$ Δf''	$AgK\alpha_1$ Δf'	$AgK\alpha_1$ Δf''
XE*	-11.31	10.29	-3.23	9.99	-1.20	7.15	-0.59	2.30	-0.87	1.62
CS*	-10.46	11.19	-4.04	10.83	-1.40	7.75	-0.53	2.49	-0.79	1.76
BA*	-10.83	8.81	-5.14	11.60	-1.66	8.30	-0.48	2.66	-0.73	1.88
LA*	-11.76	3.55	-7.09	12.45	-2.01	8.90	-0.44	2.86	-0.67	2.02
CE	-8.96	3.82	-8.67	10.74	-2.45	9.48	-0.42	3.04	-0.62	2.15
PR*	-7.81	4.08	-10.72	8.37	-3.01	10.05	-0.40	3.22	-0.58	2.28
ND	-7.07	4.36	-10.39	8.88	-3.70	10.65	-0.39	3.42	-0.54	2.41
PM*	-6.57	4.60	-12.63	3.57	-4.55	11.22	-0.38	3.60	-0.51	2.54
SM	-6.13	4.92	-9.03	3.82	-6.02	11.92	-0.38	3.82	-0.48	2.70
EU	-5.81	5.19	-7.88	4.04	-9.89	10.17	-0.39	4.03	-0.46	2.85
GD	-5.55	5.49	-7.16	4.27	-9.18	10.72	-0.40	4.24	-0.44	3.00
TB	-5.34	5.82	-6.65	4.52	-9.31	8.27	-0.42	4.48	-0.43	3.17
DY	-5.16	6.16	-6.24	4.79	-9.83	8.73	-0.45	4.73	-0.42	3.34
HO	-5.04	6.37	-5.97	4.95	-14.04	3.51	-0.51	4.95	-0.42	3.50
ER	-4.92	6.75	-5.70	5.25	-9.27	3.73	-0.56	5.22	-0.42	3.68
TM*	-4.82	7.12	-5.49	5.54	-8.06	3.93	-0.62	5.49	-0.42	3.88
YB	-4.76	7.43	-5.33	5.78	-7.36	4.10	-0.70	5.75	-0.44	4.06
LU	-4.71	7.77	-5.18	6.04	-6.85	4.29	-0.80	6.03	-0.46	4.26
HF	-4.65	8.24	-5.04	6.40	-6.43	4.55	-0.90	6.34	-0.48	4.48
TA	-4.63	8.67	-4.92	6.74	-6.11	4.78	-1.03	6.65	-0.51	4.70
W	-4.61	9.18	-4.82	7.14	-5.83	5.07	-1.17	6.99	-0.55	4.93
RE	-4.62	9.74	-4.73	7.57	-5.58	5.37	-1.34	7.34	-0.60	5.18
OS	-4.65	10.23	-4.67	7.95	-5.39	5.64	-1.54	7.68	-0.65	5.43
IR	-4.71	10.77	-4.63	8.37	-5.22	5.94	-1.77	8.05	-0.72	5.69
PT	-4.79	11.31	-4.60	8.80	-5.08	6.24	-2.05	8.43	-0.81	5.95
AU	-4.89	12.02	-4.58	9.35	-4.93	6.63	-2.36	8.84	-0.90	6.24
HG*	-5.02	12.76	-4.57	9.92	-4.80	7.04	-2.74	9.28	-1.00	6.55
TL	-5.22	13.39	-4.62	10.41	-4.72	7.39	-3.21	9.71	-1.13	6.85
PB	-5.44	14.19	-4.66	11.03	-4.64	7.83	-3.79	10.18	-1.28	7.18
BI	-5.70	14.99	-4.73	11.65	-4.57	8.27	-4.54	10.65	-1.45	7.52
PO*	-5.98	15.79	-4.81	12.28	-4.51	8.72	-5.70	11.16	-1.65	7.88
AT*	-6.36	16.66	-4.94	12.95	-4.47	9.19	-9.80	9.47	-1.89	8.24
RN*	-6.82	17.56	-5.11	13.65	-4.46	9.69	-9.02	9.92	-2.16	8.62
FR*	-7.38	18.56	-5.32	14.43	-4.46	10.24	-7.42	7.34	-2.49	9.03
RA	-8.14	19.50	-5.62	15.16	-4.51	10.76	-6.98	7.67	-2.87	9.42
AC*	-8.93	20.65	-5.88	16.06	-4.52	11.40	-6.89	8.04	-3.37	9.87
TH	-10.13	21.65	-6.27	16.83	-4.61	11.95	-7.18	8.38	-3.95	10.29
PA*	-11.81	22.69	-6.68	17.64	-4.70	12.52	-7.79	8.74	-4.85	10.76
U	-12.70	21.54	-7.23	18.40	-4.85	13.06	-9.19	9.09	-6.10	11.18
NP*	-14.38	22.59	-7.82	19.27	-4.99	13.68	-10.56	4.27	-7.61	9.52
PU*	-14.13	20.60	-8.57	20.04	-5.18	14.22	-8.32	4.44	-8.04	6.89
AM*	-14.16	21.49	-9.57	20.91	-5.41	14.84	-7.42	4.64	-6.71	7.16
CM*	-14.78	22.50	-11.24	21.87	-5.68	15.53	-6.84	4.85	-6.33	7.46
BK*	-15.75	23.42	-12.09	20.77	-6.00	16.17	-6.44	5.05	-6.24	7.74
CF*	-17.14	24.37	-13.68	21.62	-6.38	16.83	-6.12	5.26	-6.33	8.04

Appendix 3: Atomic Number density definition

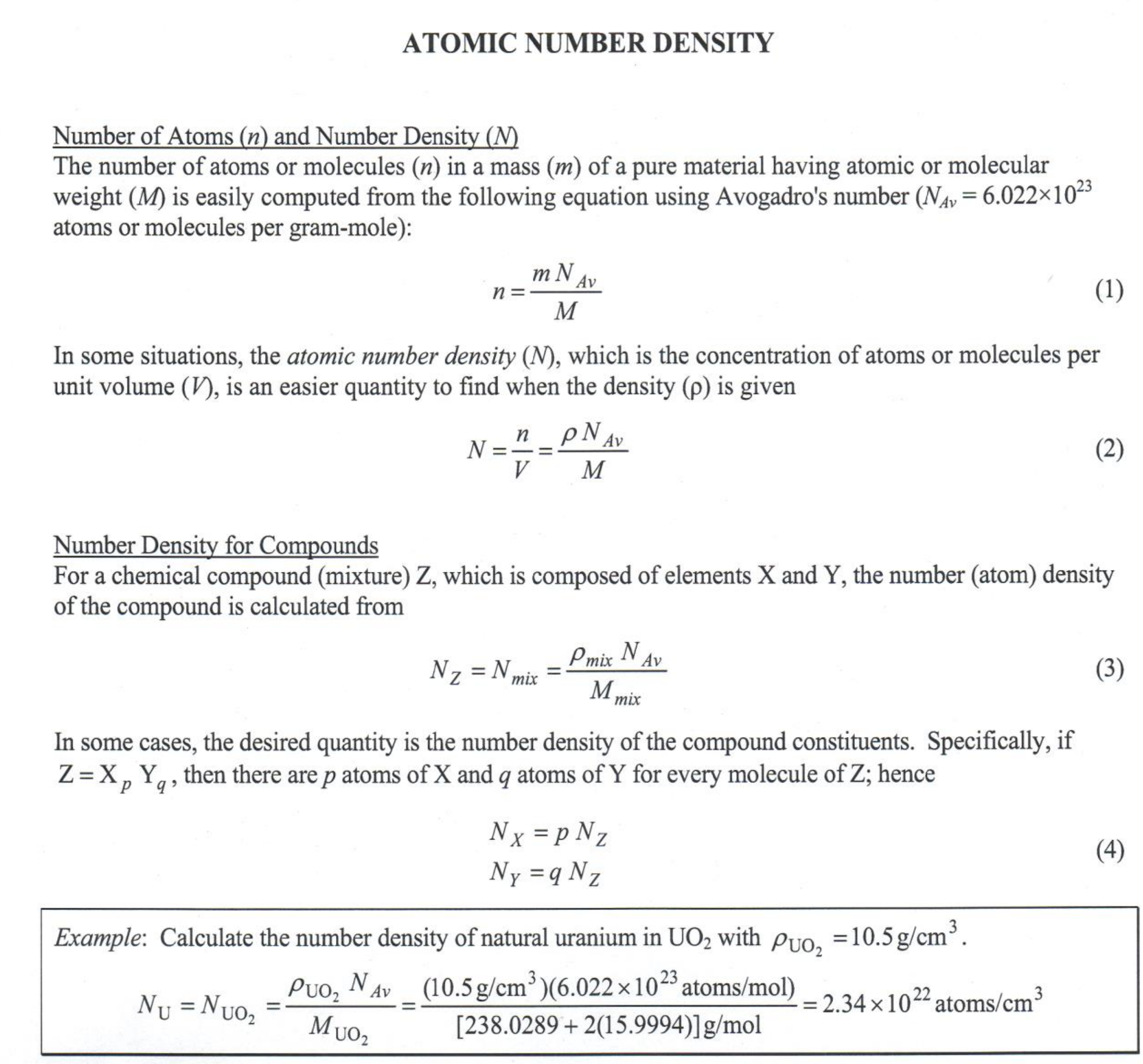

ATOMIC NUMBER DENSITY

Number of Atoms (n) and Number Density (N)

The number of atoms or molecules (n) in a mass (m) of a pure material having atomic or molecular weight (M) is easily computed from the following equation using Avogadro's number ($N_{Av} = 6.022\times10^{23}$ atoms or molecules per gram-mole):

$$n = \frac{m\,N_{Av}}{M} \qquad (1)$$

In some situations, the *atomic number density* (N), which is the concentration of atoms or molecules per unit volume (V), is an easier quantity to find when the density (ρ) is given

$$N = \frac{n}{V} = \frac{\rho\,N_{Av}}{M} \qquad (2)$$

Number Density for Compounds

For a chemical compound (mixture) Z, which is composed of elements X and Y, the number (atom) density of the compound is calculated from

$$N_Z = N_{mix} = \frac{\rho_{mix}\,N_{Av}}{M_{mix}} \qquad (3)$$

In some cases, the desired quantity is the number density of the compound constituents. Specifically, if $\mathrm{Z} = \mathrm{X}_p\,\mathrm{Y}_q$, then there are p atoms of X and q atoms of Y for every molecule of Z; hence

$$\begin{aligned} N_X &= p\,N_Z \\ N_Y &= q\,N_Z \end{aligned} \qquad (4)$$

Example: Calculate the number density of natural uranium in UO_2 with $\rho_{UO_2} = 10.5\,\mathrm{g/cm^3}$.

$$N_U = N_{UO_2} = \frac{\rho_{UO_2}\,N_{Av}}{M_{UO_2}} = \frac{(10.5\,\mathrm{g/cm^3})(6.022\times10^{23}\,\mathrm{atoms/mol})}{[238.0289 + 2(15.9994)]\,\mathrm{g/mol}} = 2.34\times10^{22}\,\mathrm{atoms/cm^3}$$

Appendix 4: Linear absorption factor μt definition/derivation

When passing through a material with a linear absorption coefficient, μ, and thickness, t, x-rays get attenuated/absorbed. The process can be quantified as follows:

$$I(\text{passed through sample}) = I_o(\text{before sample}).\exp(-\mu t)$$

By measuring I and I_o (see below) the linear absorption factor can be obtained from

$$\mu t = -\ln(I/I_o)$$

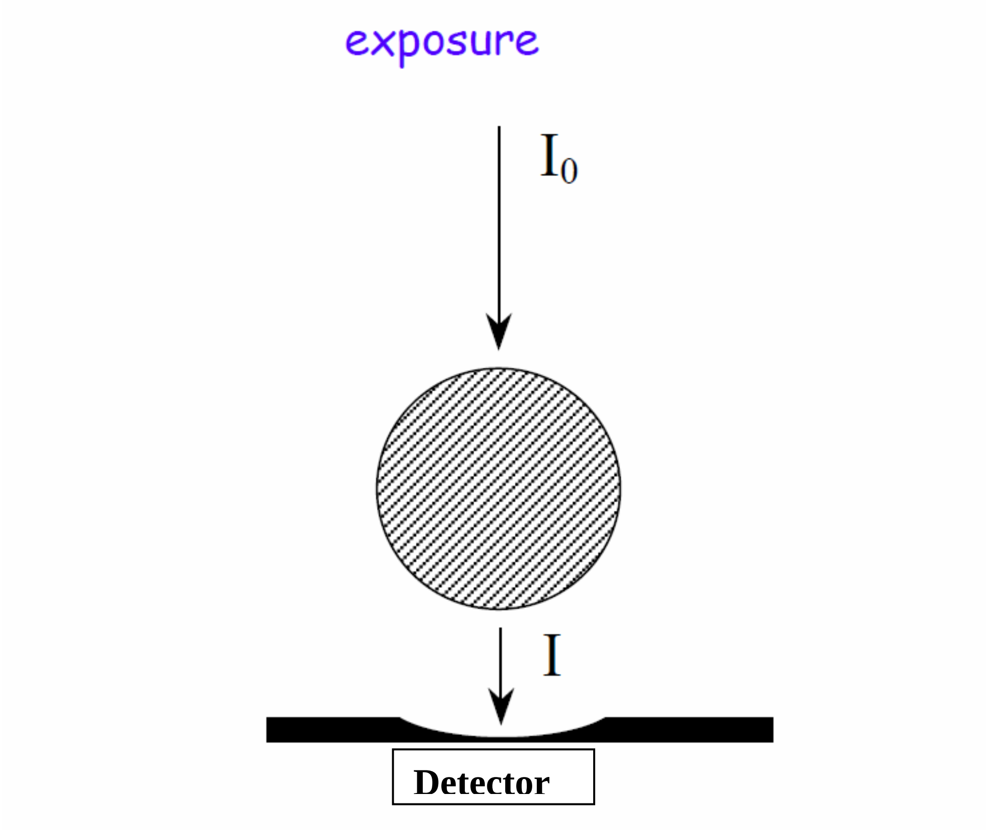

Attachments:

VP's papers featuring RAD and examples of RAD usage illustrated in this User's manual.

Invited reviewe article for Wiley's
"Characterization of Materials"
Introduces atomic PDFs technique

PAIR DISTRIBUTION FUNCTIONS ANALYSIS

Valeri Petkov

Department of Physics, Central Michigan University,
Mt. Pleasant, MI, USA

INTRODUCTION

The atomic-scale structure, that is, how atoms are arranged in space, is a fundamental material's property. Pair distribution functions (PDF)s analysis is a widely used technique for characterizing the atomic-scale structure of materials of limited structural coherence. It was first applied on liquids and glasses (Warren, 1934). Recently, it was extended to crystals with intrinsic disorder (Egami and Billinge, 2003) and nanosized particles (Petkov, 2008). The technique is based on the fact that any condensed material acts as a diffraction grating when irradiated with x-rays producing a diffraction pattern that is a Fourier transform of the distribution of the *distinct* atomic pair distances in that grating (Klug and Alexander 1974). Therefore, by collecting an x-ray diffraction (XRD) pattern and Fourier transforming it the distribution of the atomic pair distances in any condensed material can be obtained. In an atomic PDF that distribution appears as a sequence of peaks starting at the shortest and continuing up to the longest distinct atomic pair distance a material shows. The areas under the PDF peaks are proportional to the number of atomic pairs occurring at the respective distances and the widths of the peaks—to the root-mean-square (rms) scatter, U_{ij}, about those distances. In particular, the full width at half maximum of a PDF peak equals $2U_{ij}\sqrt{2\ln 2}$ where i and j denote the particular atomic pair type. The atomic rms scatter amplitudes U_{ij} (see articles X-ray Powder Diffraction and Single-Crystal X-ray Structure Determination) may be dynamic (e.g., thermal) or static (e.g., due to strain) in nature reflecting correlated or uncorrelated atomic motion (Jeong et al., 1999).

An example of experimental atomic PDFs for one of the most abundant material on Earth—water, in its solid crystalline and liquid forms, is shown in Figure 1. The PDF peaks below 2 Å reflect interatomic distances within the water molecules and those at longer distances—between atoms from different water molecules. Water molecules are arranged into a long-range ordered, periodic structure with an average hexagonal symmetry in crystalline ice (Kuhs and Lehmann, 1983). The degree of structural coherence in crystalline ice is high and so the respective PDF shows a series of well-defined peaks up to very high interatomic distances. Molecules in liquid water are only short-range ordered reflecting its low degree of structural coherence (Malenkov, 2009). Accordingly, the respective PDF peaks to distances of about 1 nm only. Depending on the degree of their structural coherence, materials may show PDFs behaving like that for solid crystalline ice or that for liquid water, or like something in between. Thus by examining the profile of an experimental atomic PDF, the degree of structural coherence in a condensed material can be easily recognized. Moreover, as exemplified below, by analyzing the positions and areas of the PDF's peaks the characteristic for a particular material distribution of distinct interatomic pair distances and numbers, also known as atomic coordination sphere radii (R_i) and numbers (CN_{ij}), can be obtained over the whole length of structural coherence a material shows. For a given condensed material, the $\{R_i, CN_{ij}\}$ distribution is unique and so it can be used as its "structural fingerprint." Also, a PDF can be easily computed for any model configuration of atoms and then compared with an experimental PDF. This allows convenient testing and refining of three-dimensional structure models for materials of any degree of structural coherence. The models may be periodic or not periodic in nature allowing crystals and noncrystals to be considered on the same footing. From the model, atomic configurations important material's properties, for example, the electronic band structure and conductivity type (Petkov, 2002), may be computed and so better understood.

COMPETITIVE AND RELATED TECHNIQUES

The first Nobel prize was awarded to Wilhelm Röntgen for the discovery of x-rays back in 1901. The Nobel prize in 1914 went to Max von Laue for the discovery of x-rays diffraction in crystals. Since then x-ray diffraction has been a major scientific tool for the determination of the structure of single crystals. The techniques benefits from the fact that several independent diffraction patterns can be collected for different orientations of the single crystal specimen with respect to the x-ray beam (Giacovazzo, 1998). The recorded several tens to many hundreds or even thousands sharp diffraction spots, also known as Bragg peaks, provide a firm basis for the determination of the atomic-scale structure of single crystals from simple solids to proteins (see also Single-Crystal X-ray Structure Determination). The atomic PDF resembles the so-called Patterson function that is widely used in traditional crystallography (Giacovazzo, 1998). However, while the Patterson function peaks at interatomic distances within the unit cell of a crystal, the atomic PDF peaks (see Fig. 1) at all distinct interatomic distances occurring in a material. Interatomic distances of different spatial orientations but same magnitude will come as a single PDF peak since the atomic PDF is one dimensional, spherically, that is, all atomic-scale structure orientations averaged representation of the respective diffraction grating/material (see Fig. 2). For this reason, atomic PDFs analysis has little advantage to offer in single crystal structure studies. Its advantages are much more obvious in studying the atomic-scale structure of materials that are not perfect single crystals in nature.

Typical polycrystalline materials consist of a large number of randomly oriented crystallites. As a result, polycrystalline materials exhibit one-dimensional diffraction patterns where all atomic-scale structure

Characterization of Materials, edited by Elton N. Kaufmann.

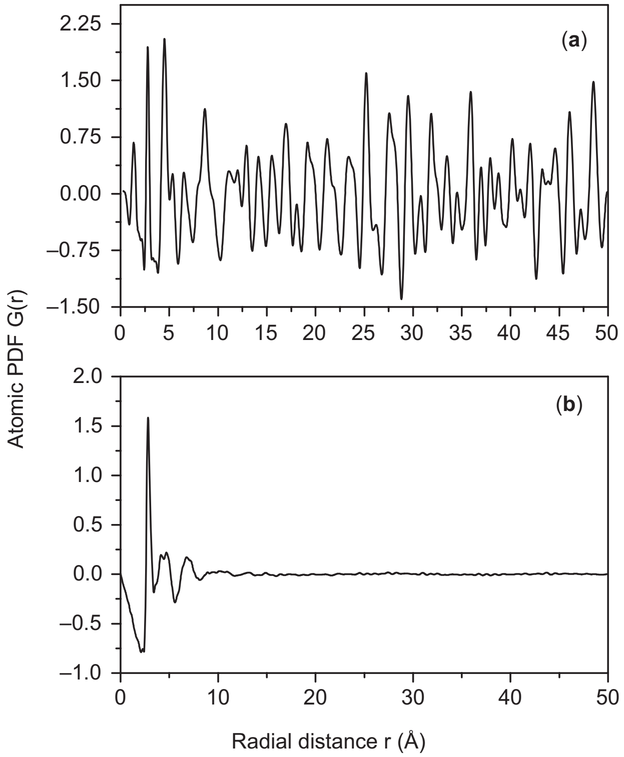

Figure 1. Experimental atomic PDFs for solid crystalline (**a**) and liquid water (**b**).

orientations are randomly, that is, spherically averaged (see article X-ray Powder Diffraction). Although the structure orientations are averaged out in x-ray powder diffraction patterns they still show several tens up to a few hundred sharp Bragg peaks allowing a successful crystal structure refinement and even determination to be carried out in an almost routine way (David et al., 2002; Samy et al., 2010). Depending on their degree of structural coherence materials will show powder diffraction patterns with only sharp Bragg peaks (e.g., crystalline ice) or only broad, diffuse-type diffraction features (e.g., water), or both. Powder diffraction analysis mostly concentrates on the sharp Bragg peaks and considers them in terms of structure models based on infinite periodic lattices (Hahn, 2002). On the other hand, atomic PDFs analysis uses both the Bragg peaks and the diffuse-type scattering components in the diffraction pattern. In this way both the existing atomic order, manifested in the Bragg-like peaks, and all structural "imperfections" (e.g., strain, defects, very small/nanosize particle's dimension) that are responsible for its limited extent, manifested in the diffuse component of the diffraction pattern, are reflected in the experimental PDFs. This renders the atomic PDFs analysis much better suited to study materials where the periodicity of the atomic arrangement is partially broken due to local structural distortions (Petkov, 1999) or the atomic arrangement is not periodic at all (Roux et al., 2011). In this respect, atomic PDFs analysis goes beyond traditional powder x-ray diffraction analysis that yields only the periodic features of the atomic-scale structure.

Spectroscopy techniques such as expended x-ray absorption fine structure (EXAFS) and nuclear magnetic resonance (NMR) are also frequently used to study the local atomic arrangement in materials, including determining of atom–atom separations and coordination numbers (Czichos et al., 2006; see articles NMR Spectroscopy in the Solid State and XAFS Spectroscopy). These techniques have a better atomic species sensitivity (less than 1 at%) than x-ray diffraction-based atomic PDFs analysis (down to few atomic percent). Spectroscopy techniques, however, yield structural information related not to all present but only to the particular atomic species probed. Besides, this information is limited to interatomic distances up to 5–6 Å only.

Imaging techniques such as high-resolution transmission electron microscopy (TEM) can provide information about material's structure with atomic resolution (Czichos et al., 2006; see articles Scanning Electron Microscopy and Transmission Electron Microscopy). However, as any other image, TEM images are just a projection down an axis and so are not easy to be interpreted in terms of a unique three-dimensional atomic arrangement. The situation may change for better with the recent advances in TEM tomography (Midgley and Dunin-Borkowski, 2009). Nevertheless, data from present day EXAFS and TEM experiments are very useful, in particular in providing independent constraints for structure modeling guided by atomic PDFs (Roux et al., 2011).

PRINCIPLES OF THE METHOD

Atoms in condensed matter interact via chemical bonds that impose preferred atom–atom separations and coordination numbers that do not change a lot even when a material appears in phase states of very different structural coherence. For example, both quartz crystals (SiO_2) and silica glass (SiO_2) are made of rigid Si–O_4 tetrahedral units that share all of their corners. The difference is that in quartz crystals, the tetrahedra are assembled into a periodic network of hexagonal symmetry (Page and Donnay, 1976), whereas in the glass that network is completely random (Zachariasen, 1932). The situation with crystalline ice and water is similar (Malenkov, 2009) regardless of the fact that the hydrogen–oxygen bonds in it are much weaker than the Si-O covalent bonds in silicates. Given the presence of well-defined chemical bonds and the imposed by them distinct atom–atom separations and coordination numbers, a quantity called atomic pair distribution function can be defined for any condensed material. In particular, the frequently used reduced atomic PDF, $G(r)$, gives the number of atoms in a spherical shell of unit thickness at a distance r from a reference atom as follows:

$$G(r) = 4\pi r[\rho(r) - \rho_o] \tag{1}$$

where $\rho(r)$ and ρ_o are the local and average atomic number densities, respectively. As illustrated in Figure 2, the atomic PDF is a one-dimensional function that oscillates

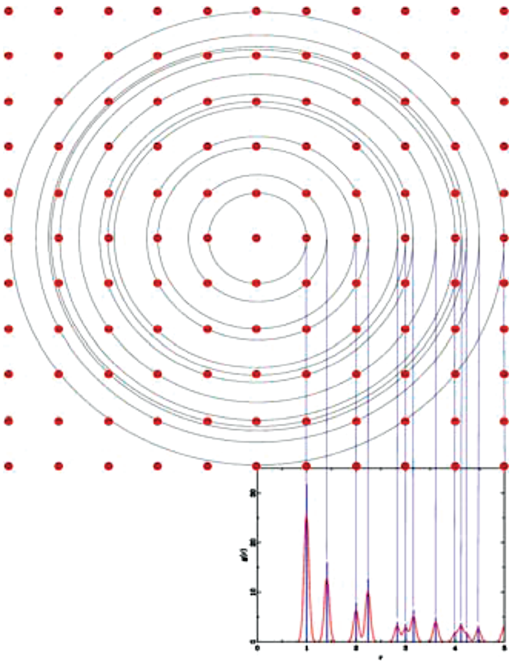

Figure 2. Spherically averaged distribution of interatomic distances and numbers in a hypothetical square lattice of atoms (points). The distribution peaks at distances separating pairs of atoms; peak areas are proportional to the number of atoms at those distances.

around zero and shows positive peaks at distances separating distinct pairs of atoms, that is, where the local atomic density exceeds the average one. As demonstrated in Figure 1, the oscillations are very pronounced and characteristic to the particular phase state of the studied material. Since the wavelength of x-rays is comparable to the distances between atoms in condensed matter, x-rays can scatter constructively from the grating of uniformly separated and coordinated atoms in a condensed material. Moreover, the resulted diffraction pattern reflects the spatial characteristics of that grating (Giacovazzo, 1998; Klug and Alexander 1974). Indeed, the PDF $G(r)$ is the exact Fourier transform of the atomic-scale structure sensitive part of the scattered x-ray intensities, also known as structure function, S(Q), that is,

$$G(r) = (2/\pi)\int_{Q=Q_{\min}}^{Q_{\max}} Q[S(Q)-1]\sin(Qr)dQ \qquad (2)$$

where Q is the magnitude of the wave vector ($Q = 4\pi\sin\theta/\lambda$), 2θ is the angle between the incoming and outgoing x-rays and λ is the wavelength of the x-rays used (Wagner, 1969). Note the structure function, $S(Q)$, is related to only the coherent/elastic part of the scattered x-ray intensities, $I^{\mathrm{coh.}}(Q)$, as follows:

$$S(Q) = 1 + \left[I^{\mathrm{coh.}}(Q) - \sum c_i|f_i(Q)|^2\right] \bigg/ \left|\sum c_i f_i(Q)\right|^2, \quad (3)$$

where c_{i} and $f_i(Q)$ are the atomic concentration and x-ray scattering factor, respectively, for the atomic species of type i. Note, other definitions of $S(Q)$ and the atomic PDF are also known but less frequently used (Keen, 2001). Also, the integral in Equation 2 is taken from $Q_{\min}$ to $Q_{\max}$ where the former is the lowest (typically of the order of 0.3–0.5 Å^{-1}) and the latter the highest wave vectors, respectively, reached in the diffraction experiment. In other words, in this common derivation of $G(r)$ the small-angle scattering intensities that appear at wave vectors approaching zero are not included. If those were included a modified atomic distribution function, $G'(r) = 4\pi r[\rho(r) - \gamma_o(r)\rho_o]$ would be obtained, where $\gamma_o(r)$ is function reflecting large-scale density fluctuations in the material studied, including the shape of its constituent crystallites/particles (Farrow and Billinge, 2009). No examples of atomic PDF studies that incorporate small-angle scattering intensities are known yet, though this may change in future. In this review article, we stick to the common derivation (given in Equations 1, 2 and 3) and usage of atomic PDFs that do not include small-angle scattering information. Within this common derivation, the integral in Equation 2 can be represented in a discrete form to take into account the discrete nature of XRD experiment, that is,

$$G(r_k) = (2/\pi)\sum_{i=1}^{N} Q_i[S(Q_i)-1]\sin(Q_i r_k)\Delta Q \qquad (4)$$

where N is the number of actual experimental data points, Q_i, collected in equidistant ΔQ steps as usually done in XRD studies. Here r_k is a real-space distance at which $G(r)$ has been chosen to be evaluated. For practical purposes $G(r)$ is also evaluated at a number of equidistant real space distances $r_{\mathrm{k}} = k\Delta r$ points, where k is an integer number. Typically Δr is of the order of 0.01 to 0.05 Å. However, following the Nyquist-Shannon sampling theorem the step Δr is best to be set close to $\pi/Q_{\max}$ (Thijsse, 1984; Farrow et al., 2011).

Therefore, to obtain an experimental atomic PDF an XRD data set should be collected, only the coherent part, $I^{\mathrm{coh.}}(Q)$, of the collected intensities extracted, reduced to a structure factor S(Q) (Equation 3) and then Fourier transformed (Equations 2 and 4). For a material comprising n atomic species a single diffraction experiment would yield a total atomic distribution function, $G(r)$, which is a weighted sum of $n(n+1)/2$ partial PDFs, $G(r_{ij})$, that is,

$$G(r) = \sum_{i,j} w_{ij} G_{ij}(r), \qquad (5)$$

where w_{ij} are weighting factors (Wagner, 1969) depending on the concentration and scattering power of the atomic species as follows:

$$w_{ij} = c_i c_j f_i(Q) f_j(Q) \bigg/ \left|\sum c_i f_i(Q)\right|^2. \qquad (6)$$

For practical purposes w_{ij}'s are often evaluated for $Q = 0$.

A total PDF for a multielement material, however, will comprise quite a few partial atomic correlations which may render its interpretation ambiguous.

Element specificity may be added by employing the so-called resonant XRD, which involves measuring two diffraction data sets close to but below the absorption edge of an atomic species, taking the difference between these two data sets, and Fourier transforming it into a quantity called a differential atomic PDF. Similarly to EXAFS spectroscopy, the differential atomic PDF will reflect only correlations relative to the element whose absorption edge is probed. However, unlike EXAFS, it will show these correlations to the longest interatomic distances to which they extend (Petkov and Shastri, 2010). As demonstrated recently, differential atomic PDFs can be very useful in revealing very fine structural features of complex materials (Petkov et al., 2010a).

PRACTICAL ASPECTS OF THE METHOD

To ensure good quality results XRD experiments aimed at atomic PDFs analysis should be conducted paying special attention to the following details:

Source of X-ray Radiation: XRD data up to high wave vectors should be collected so that the respective atomic PDF is of good enough real-space resolution to reveal all important structural features of the material studied. High-wave vectors can be reached by employing x-rays of a shorter wavelength, that is, of higher energy. For example, by using synchrotron radiation x-rays of energy 60 keV (Petkov et al., 1999) structure functions for (In–Ga)As semiconductors extending to $Q_{\max}=45$ $Å^{-1}$ were possible to be obtained (see Fig. 3). The respective atomic PDFs have an excellent real-space resolution, $\delta r = 2\pi/Q_{\max} = 0.14$ Å, allowing to reveal the presence of distinct Ga–As (2.44 Å) and In–As (2.61 Å) bonds in this semiconductor alloy (see Fig. 4). If x-rays of energy 8 keV (Cu K_α radiation) or 22 keV (Ag K_α) radiation were used XRD data would have been possible to be collected to $Q_{\max}$ values of approximately only 8 $Å^{-1}$ and 20 $Å^{-1}$, respectively (see the broken lines in Fig. 3). Using XRD data with $Q_{\max}=20$ $Å^{-1}$ in the Fourier transformation of Equation 2 and 4 would not have allowed to resolve the distinct Ga-As and In-As bonds but yet allowed to reveal well the characteristic sequence of coordination spheres in (In–Ga)As semiconductor alloys (see Fig. 5). Using XRD data with $Q_{\max}=8$ $Å^{-1}$ would have produced a very low-resolution PDF where the individual peaks are merged (see the 5–8 Å region in Fig. 5) beyond recognition. Such low real-space resolution PDF data may be very misleading, leading to erroneous interpretation. The example emphasizes the importance of collecting and using XRD data up to as high wave vectors as possible in atomic PDF studies. This can be achieved on in house equipment using sealed x-ray tubes with a Mo or better Ag and definitely not Cu anode, or by employing higher energy synchrotron radiation sources.

XRD Data Statistics and Collection Time: Regardless of the source of high-energy x-rays used the diffraction data should be collected with a very good statistical accuracy, usually 2–3 orders of magnitude better than that required for traditional powder XRD (e.g., Rietveld analysis) studies. An example illustrating the importance of collecting XRD of good statistical accuracy is given in Figure 6. An XRD pattern for 5 nm CdTe quantum dots (QDs) collected with 10^4 counts per Q_i data point yields a structure function that is of good statistical accuracy at low-Q values only. Due to the presence of a multiplicative Q factor in the kernel of the Fourier transformation (see Equation 2) the data noise, that is, hardly visible at low-Q values, appears greatly amplified at higher wave vectors. Following the Fourier transformation this data noise leads to pronounced high-frequency ripples throughout the respective atomic PDF. The ripples distort its profile and even may be falsely taken for "real" interatomic distances. An XRD pattern collected with 10^6 counts per Q_i data point yields an almost noise free structure factor and an atomic PDF revealing the atomic-scale structure of CdTe QDS in very accurate detail (Pradhan et al., 2007). To achieve good statistical accuracy obviously longer than usual XRD data collection time is necessary to be used. Data collection time estimates relevant to atomic PDF studies are discussed in (Toby and Egami, 1992; Peterson et al. 2003; Mullen and Levin, 2011). Also, the step ΔQ (or the equivalent to it step in the Bragg angles) with which the XRD data are

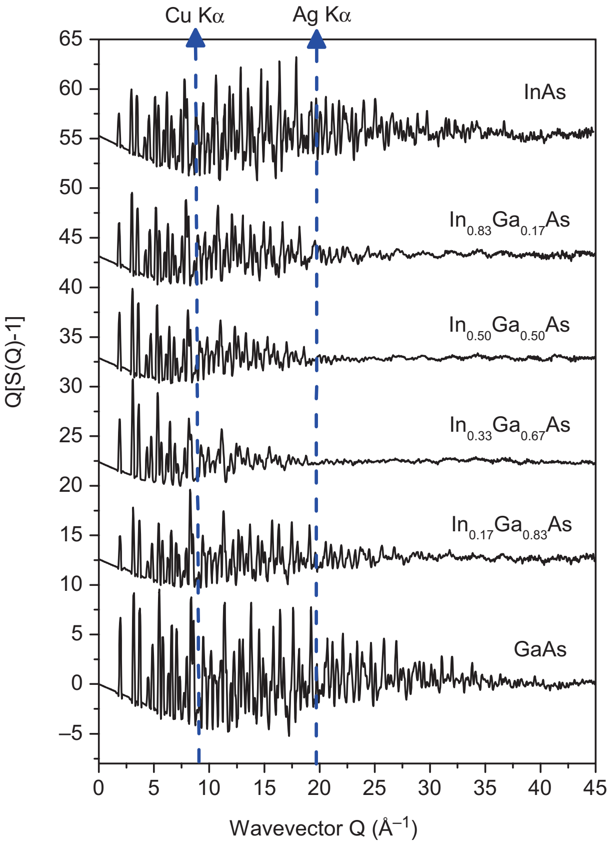

Figure 3. Experimental structure factors for (In–Ga)As semiconductor alloys obtained with synchrotron x-rays of energy 60 keV ($\lambda = 0.205$ Å). Broken lines show the maximum wave vector Q that could have been reached if CuK_α ($\lambda = 1.54$ Å) or AgK_α ($\lambda = 0.509$ Å) radiation were used instead.

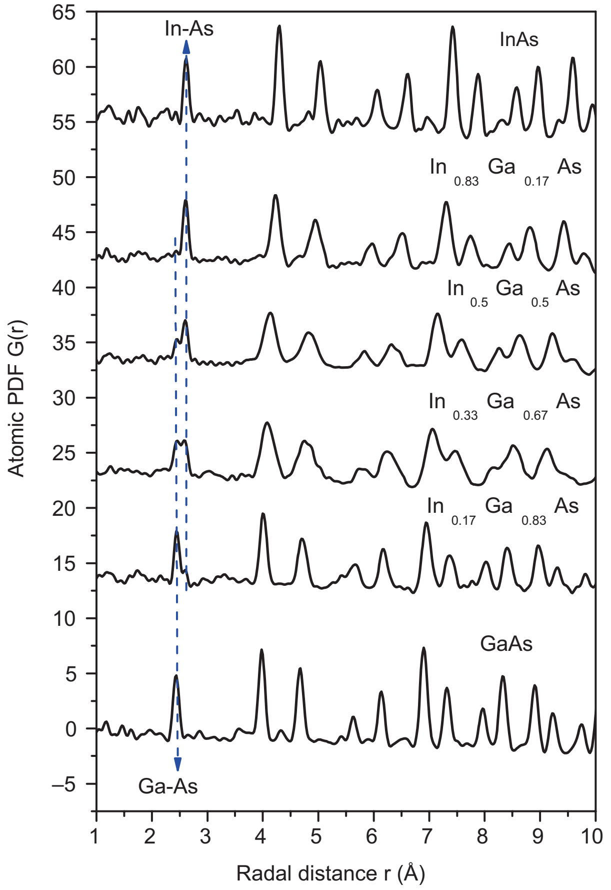

Figure 4. Experimental PDFs for (In–Ga)As semiconductors obtained by Fourier transforming the structure factors of Figure 3. Broken lines with arrows mark the shortest Ga–As (2.44 Å) and In–As (2.61 Å) bond lengths in the alloy samples.

collected should be small enough (e.g., ensuring at least 5–7 Q_i data points under a Bragg-like peak) so that no fine diffraction features are missed. In total, all this may result in many tens of hours of data collection time per sample if a sealed x-ray tube source and a single point (e.g., scintillation) detector are employed. Synchrotron x-rays and large area detectors may reduce the data collection time to seconds (Chupas et al., 2003; Lee et al., 2008a).

Experimental Setup (Q-space) Resolution: In general, structure studies on materials of limited structural coherence do not require experimental setups with very high reciprocal (Q)-space resolution because of the inherently diffuse nature of the XRD patterns such materials show. However, care should be taken that the reciprocal space resolution of the experimental set up, including the detector, is not too low either. As an example, atomic PDFs for $BaZr_{0.1}Ti_{0.9}O_3$ ceramics obtained from XRD data sets collected with two different types of detectors, an image plate (IP) detector, and a detector set of 12 single crystals (Lee et al., 2008b) are shown in Figure 7. The quite low Q-space resolution of the XRD data collected with an area IP detector, that is, the quite large detector introduced broadening of the XRD peaks, leads to a very fast, unphysical decay (Qiu, 2004a) in the respective atomic PDF. As a result, it appears completely flat for distances above 50–60 Å that are much shorter than the actual length of structural coherence in these ceramics. By contrast, the much higher Q-space resolution of the XRD data collected with the detector set of 12 single crystals results in an atomic PDF showing physical oscillations, that is, the presence of distinct atomic coordination spheres, to very high interatomic distances allowing studying of long-range atomic ordering effects. Therefore, to avoid unwanted loss of information in the higher region of atomic PDFs, the Q-space resolution of the experimental set up, in particular that of the detector, should be adjusted accordingly.

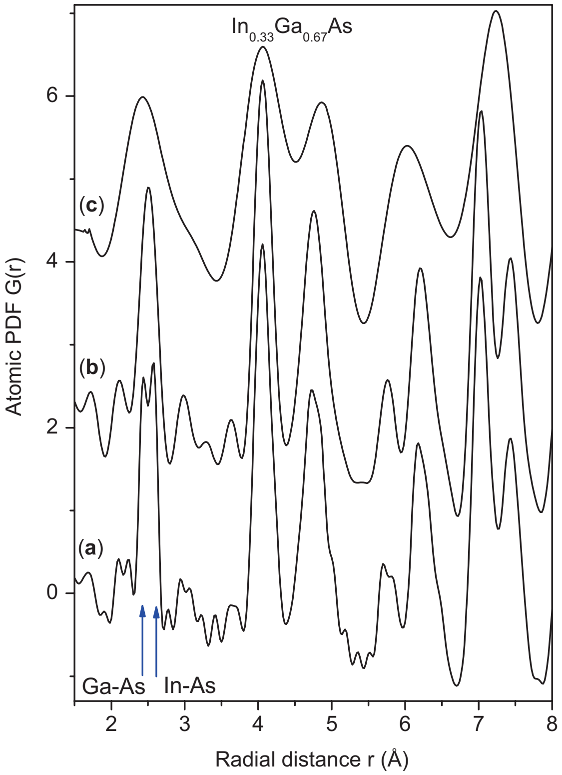

Figure 5. Experimental PDFs for $In_{0.33}Ga_{0.67}As$ alloy obtained by Fourier transforming the respective structure factor of Figure 3 with Q_{max} set to 45 Å^{-1} (**a**), 20 Å^{-1} (**b**), and 8 Å^{-1} (**c**). Arrow marks the shortest Ga–As (2.44 Å) and In–As (2.61 Å) bond lengths in this material. Those are clearly resolved only when XRD data collected up to 45 Å^{-1} are included in the Fourier transformation.

Finite Particle's Size Effect on Atomic PDFs: Atomic PDFs analysis is very well suited to study the atomic arrangement in nanosized particles (Gilbert et al., 2004; Petkov, 2008). The finite size and highly anisotropic shape of nanosized, in particular 1–10 nm in size, particles may affect the shape and intensity of the peaks in experimental atomic PDFs substantially (Petkov et al., 2009). The effect of particle's finite size on the atomic PDFs is somewhat similar to that of the low-Q space resolution discussed above so care should be taken that those are not confused with each other. The finite particle's size effect can be taken into account by using appropriate particle's shape functions (Kodama

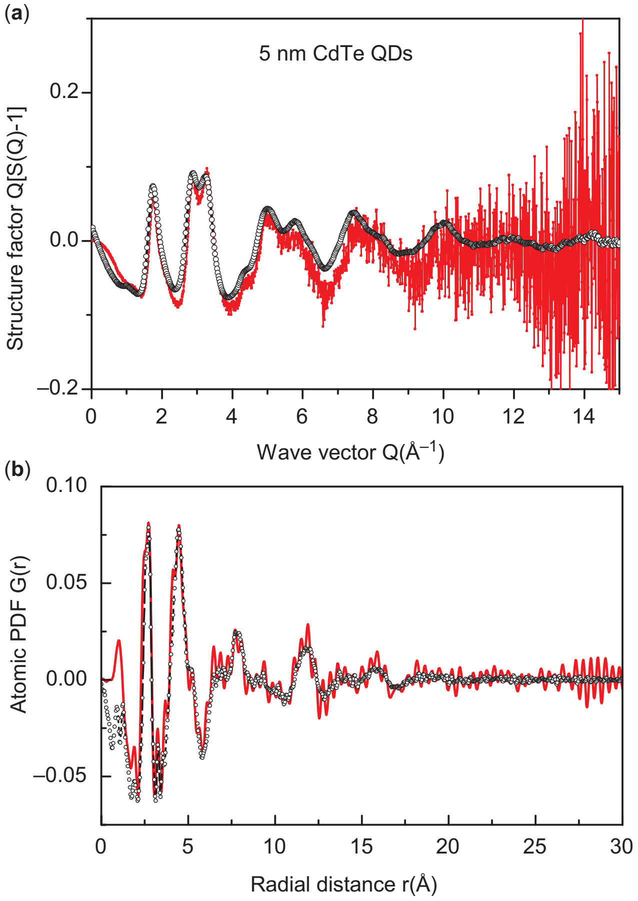

Figure 6. Experimental structure factors for 5 nm CdTe quantum dots (QD)s collected with 10^4 (full line in gray) and 10^6 (symbols) counts per data point (**a**). The respective atomic PDFs are shown in (**b**). That obtained from the data set of lower statistical accuracy suffers pronounced high-frequency, unphysical ripples.

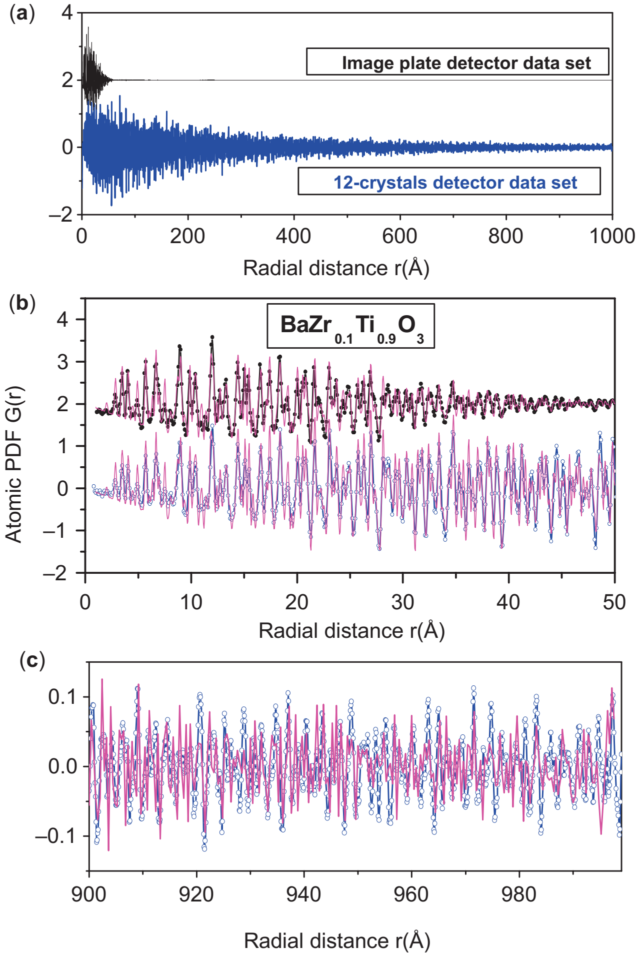

Figure 7. (**a**) Experimental atomic PDFs for BZT ceramics obtained with an image plate detector (line in black) and a detector set of 12 single crystals (line in dark gray). The low Q-resolution image plate detector yields an atomic PDF that decays to zero at distances of 50–60 Å that are much shorter than the average domain size in the ceramics material studied. The higher Q-resolution detector set of 12 crystals yields an atomic PDF that shows physical oscillations up to distances of 1000 Å, and more, that are comparable to the average domain size in this material. (**b**, **c**) Fragments of the experimental PDF data as fit with a model featuring the well-known perovskite structure of BZT (line in light gray). Experimental and model PDF's peaks match well to very high interatomic distances confirming the physical origin of the PDF's oscillations.

et al. 2006; Farrow et al., 2007) or by building finite size, real particle's shape structure models (Korsunsky et al., 2007; Petkov et al., 2010b).

Background Scattering Treatment: Air, sample holder etc. background-type scattering should be kept to a minimum since atomic PDFs are related to only the coherent/elastic part, $I^{\text{coh.}}(Q)$, of the x-ray intensities scattered from the sample alone (see Equation 3). As practice has repeatedly shown it is always easier to correct for a weak background signal than for a strong one. Therefore, as high as possible sample to background scattering ratio is recommended, especially at high wave vectors where that ratio should at least be of the order of 4–5 to 1. Once reduced to a minimum, the background scattering should be measured with the same statistical accuracy as the sample scattering and so used in the process of reducing the experimental XRD data into an atomic PDF.

Sample Related "Unwanted" Scattering: X-rays are both scattered from and absorbed inside materials via various processes (Klug and Alexander, 1974). The absorption of high-energy x-rays is relatively low and usually does not pose much of a problem in atomic PDFs studies. The same is true for multiple scattering of high-energy x-rays. As illustrated in Figure 8, inelastic (Compton) scattering, however, may be very strong and even exceed the elastic scattering, especially at high wave vectors (Petkov, 2002). Inelastic, that is, scattered with modified energy x-ray photons should be eliminated from the experimental XRD pattern since only its coherent/elastic part is related to the atomic PDF (see Equation 3). The elimination is best to be done during data collection by using x-ray energy sensitive detectors (Ruland, 1964; Petkov, 1999, 2000). Alternatively, it can

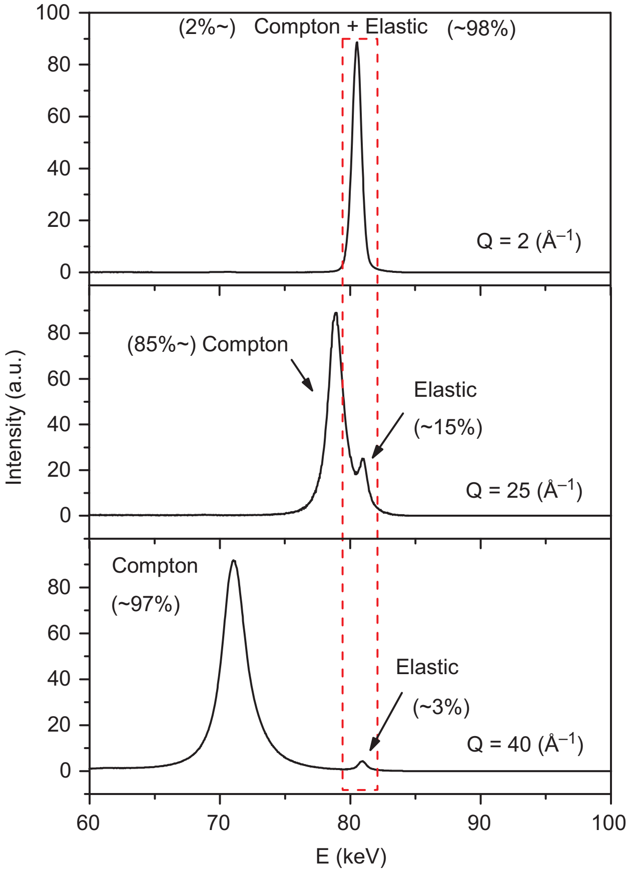

Figure 8. X-ray scattered intensities versus x-ray energy spectra from $Ca_{0.25}Al_{0.5}Si_{0.5}O_2$ glass collected at three different wave vectors, *Q*. Data were taken with x-rays of energy 80.6 keV (Petkov et al., 1999). Note the dramatic decrease of the coherent/elastic scattering (marked with broken line in red) with the increase of *Q*.

be done analytically during the reduction of the experimental XRD data into an atomic PDF. The analytical elimination of Compton scattering is, however, inevitably based on some theoretical approximations (Hajdu and Palinkas, 1972) which may lead to difficulties (Qiu, 2004a) in obtaining good quality atomic PDF data.

METHOD AUTOMATION

Atomic PDFs analysis is fully automated in all of its aspects, including XRD data collection, XRD data reduction into atomic PDFs, the interpretation of experimental PDFs in terms interatomic distances and numbers, and atomic PDFs guided structure modeling rendering the technique a rather convenient and useful scientific tool.

XRD data of quality good enough for a successful atomic PDFs study can be collected on in-house equipment for powder XRD. However, instead of the standard Cu K_α radiation source, x-ray tubes with a Mo or Ag anode or rotating (Mo or Ag) anode sources should be employed so that the XRD data are collected to at least 15–20 Å^{-1}. Also, extra care should be exercised to reduce the inherently high background scattering inside the enclosures of the standard powder XRD instruments. XRD data of quality good enough for a successful PDF study are much easily collected at synchrotron radiation sources because of the much higher intensity and energy of the x-rays produced by them allowing $Q_{\max}$ values of 30–45 Å^{-1} to be achieved. Several beam lines at numerous synchrotron radiation facilities are available all over the world, including instruments entirely dedicated to atomic PDFs studies (Chupas et al., 2003; Lee et al. 2008a; Kohara et al., 2001).

Software for correcting experimental XRD patterns for background and other "unwanted" scattering as well as for x-ray absorption, polarization, detector dead time and x-ray energy resolution, normalizing the corrected intensities into absolute units, reducing them into structure functions *S*(*Q*), and finally performing a Fourier transformation to obtain an atomic PDF is readily available (Petkov, 1989; Qiu, 2004b; Soper and Barney, 2011).

Positions and areas of peaks in experimental atomic PDFs can be extracted with the help of any software package used for visualization, manipulation, and plotting of scientific data.

Relatively small-size (up to few hundred atoms) structure models based on periodic (Bravais) lattices can be conveniently built, tested, and refined against experimental atomic PDFs with the help of the program PDFgui (Farrow et al., 2007).

Large-scale (many thousands of atoms) structure models featuring pronounced local disorder can be built, tested, and refined against experimental atomic PDFs with the help of the program DISCUS (Neder and Proffen, 2008).

Completely, nonperiodic model atomic configurations featuring glasses and liquids can be tested and refined against experimental PDF data employing reverse Monte Carlo (Gereben et al., 2007) or molecular dynamics (Lindahl et al., 2001) type procedures.

Once constructed, structure models for materials of limited structural coherence can be analyzed in terms of bond length, bond angle, and partial coordination number distributions, topological connectivity, local symmetry, and other structural characteristics with the help of the program ISAACS (Roux and Petkov, 2010).

ATOMIC PDF DATA ANALYSIS AND INTERPRETATION

An experimental atomic PDF carries a wealth of atomic-scale structure information. Some pieces of it are immediately evident in the PDF data, others need applying of extra analytical procedures to be extracted and fully exploited.

An important material's characteristic that is evident in the experimental atomic PDFs is the material's phase type (e.g., see Fig. 1). Here a phase means a part of a material that has a well-defined chemical composition and atomic-scale structure, is physically and chemically homogeneous within itself and so is surrounded by a boundary that makes it mechanically separable from the rest of the material and/or the material's environment. Bragg XRD is a major tool for qualitative phase

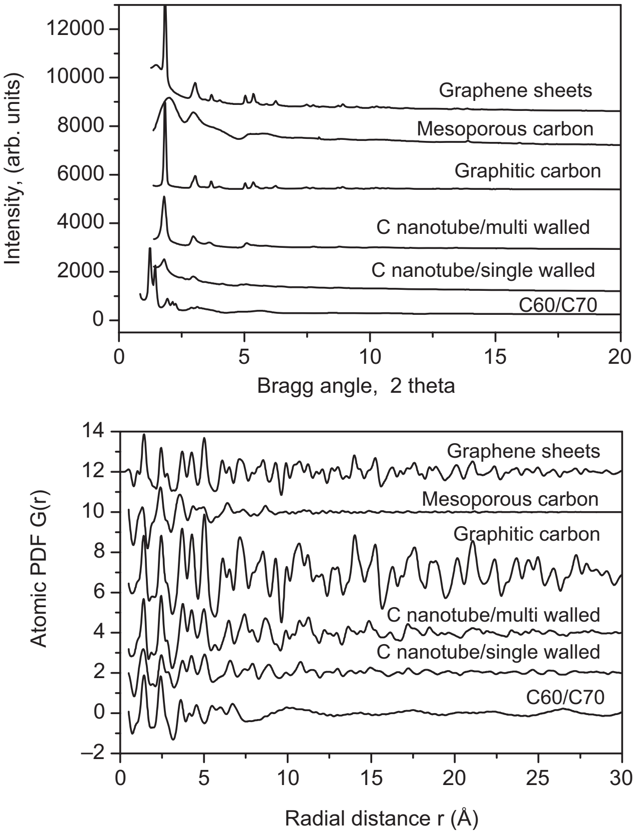

Figure 9. Experimental XRD patterns (up) and the respective atomic PDFs (down) for a series of graphitic carbons.

identification of crystalline materials. XRD patterns for materials of limited structural coherence, however, are usually quite diffuse in nature and so are difficult to be used for unambiguous phase identification. Atomic PDFs can be employed instead. As an example, experimental XRD patterns and atomic PDFs for a series of nanosized graphitic materials are shown in Figure 9. The XRD patterns show only a few Bragg-like features, whereas the respective atomic PDFs show numerous peaks coming from the sequence of well-defined atomic coordination spheres in these graphitic materials. Since carbon atoms in the different graphitic materials are arranged differently (e.g., forming stacks of flat sheets in graphitic carbons, folded sheets in the nanotubes, and spheres in the C_{60} fullerenes) the respective experimental PDFs are substantially different and so can be used to identify each of the respective graphitic phases. Reference databases of atomic PDFs can be generated for important classes of materials of limited structural coherence (e.g., for silicate glasses, industrial amorphous polymers, and pharmaceuticals) and used for their qualitative phase identification in a manner similar to that implemented in the so-called Powder Diffraction File with XRD patterns of crystals (Smith and Jenkins, 1996). Examples of successful application of atomic PDFs analysis for determining the relative fraction of phases in a mixture, that is, for quantitative phase analysis are known as well (Gateshki et al., 2007).

Another important material's characteristic is the length of structural coherence, also known as the mean size of coherent x-ray scattering domains (Klug and Alexander, 1974). Atoms from different domains are not well lined up and so do not make consecutive sequences of well defined atomic coordination spheres. Accordingly, the peaks in the atomic PDFs suffer extra loss of sharpness for distances longer than the "domain size" rendering the atomic PDF featureless beyond those distances. The fact is well demonstrated in Figure 10 showing experimental atomic PDFs for crystalline Au and nanosized Au particles (Petkov et al., 2005a). The smaller the particles, the shorter the real space distance at which the respective atomic PDF decays to zero. It goes from about 50 Å for 30 nm down to 10 Å for 1.7 nm particles. Note, the length of structural coherence in the particles is shorter than their actual size since the particles (see Fig. 11A for a structure model of 3 nm particles) exhibit extended structural defects, resembling wedge disclinations, dividing their inner part into domains that are misoriented with respect to each other. Care should be taken that the behavior of the longer part of the experimental PDFs is not dominated by low *Q*-space resolution effects (see Fig. 7) when the length of structural coherence is the quantity of interest. Correction procedures for moderate *Q*-space resolution effects are discussed in (Gateshki et al., 2005).

The commonly used atomic PDF *G*(*r*) (see Equations 1 and 2) slopes as $4\pi\rho_o{}^{*}r$ for small *r* values, in particular in the region from $r=0$ to about $r=1$ Å where no real interatomic distances exist. Therefore, estimates for the atomic number density ρ_o (i.e., density measured in atoms/Å^3) of the material studied can be obtained from the initial slope of experimental *G*(*r*) data as illustrated in Figure 10. Note since XRD experimental errors tend to add up close to the origin of the Fourier transformation (Peterson et al., 2003; Qiu, 2004a), that is, close to $r=0$ Å, the ρ_o estimate should be done with due care.

Atomic coordination numbers, CN_{ij}, are another important structural parameter. They can be derived from the area of the respective PDFs peaks. As defined the atomic PDF *G*(*r*) oscillates about zero (see Equation 1 and Fig. 1) making it inconvenient for integrating its peaks for the purpose of obtaining an estimate for the peak's areas. Another atomic PDF defined as:

$$RDF = 4\pi r^2\rho(r) = 4\pi r^2\rho o + r^{*}G(r) \qquad (7)$$

where *r* is the radial distance, and $\rho(r)$ and ρ_o the local and average atomic number densities, respectively, is better to be used in this case. From the integrated *RDF* peak areas, the number of atomic neighbors of type *j* around atomic species of type *i*, that is, CN_{ij}, can be obtained as follows:

$$CN_{ij} = c_j{}^{*}(\text{respective RDF Peak Area})/w_{ij} \qquad (8)$$

where the atomic concentrations c_j and the weighting factors w_{ij} (see Equation 6) should strictly obey the sum

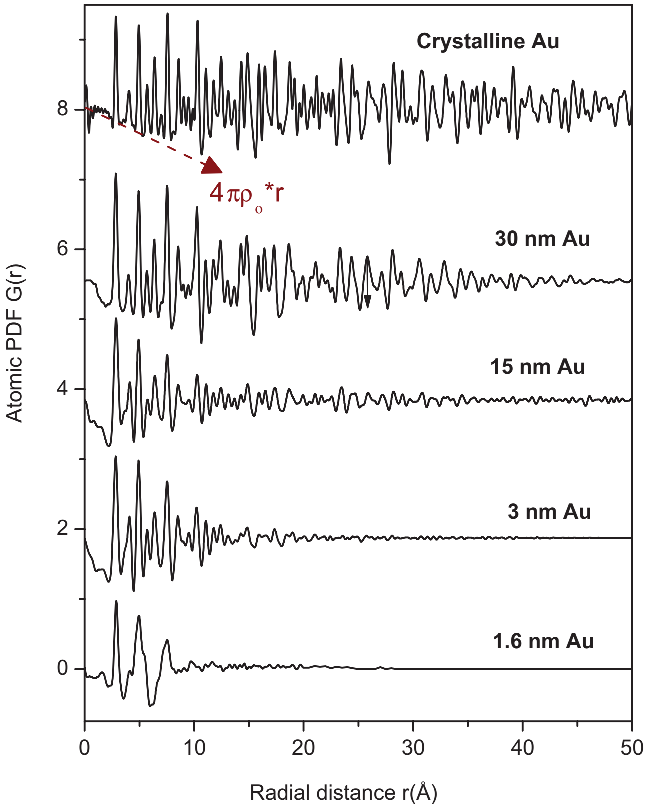

Figure 10. Experimental atomic PDFs for crystalline (μm-sized) and nanosized Au particles (Petkov et al., 2005a). Arrow marks the low-r PDF region that slopes as $4\pi\rho_o{}^*r$.

rules $\sum c_j = 1$ and $\sum w_{ij} = 1$. Note the area of a PDF/RDF peak is not simply proportional (via the c_j term in Equation 8) to the number of respective atomic pairs CN_{ij} but depends on the atomic pair's relative scattering power (via the w_{ij} term in Equation 8) as well. Therefore, for accurate estimates of CN_{ij} to be obtained, Equation 8 should be strictly applied. The areas of individual RDF peaks can be obtained by a direct integration when those peaks are well resolved. When the RDF peaks are partially overlapped, which is often the case, the individual peak areas can still be evaluated very precisely by fitting each peak with a Gaussian function as demonstrated in Figure 12. In this example, the first coordination numbers of Si, Al, and Ca atoms in $Ca_{x/2}Al_xSi_{1-x}O_2$ glasses are obtained allowing to draw important conclusions about the type of coordination units and their connectivity in the glass network (Petkov et al., 2000).

The ultimate goal of structure studies is the determination of the positions of the atoms constituting the material under study. In case of crystalline-like materials, PDFs analysis can yield the positions of atoms within the unit cell of a periodic lattice by using available software (Farrow et al., 2007, Neder and Proffen, 2008). At first, a structure model featuring a unit cell of a periodic lattice is designed using theoretical predictions or available crystal structure data for materials of similar chemistry. The sequence of coordination radii and numbers (r_i, CN_{ij}) for that model is computed and then convoluted with gaussians to take into account the thermal and eventually static atomic rms displacements in the material under study. Thus computed model PDF is compared to the experimental one and the difference between the experimental and model PDF data minimized by adjusting the atomic positions and rms displacements in the initial model. Example of a determination of the structure of a crystalline-like material via atomic PDF analysis is shown in Figure 11c. Nonperiodic type structure models that are more appropriate for liquids and glasses can also be tested and refined against atomic PDFs using available software (Gereben et al., 2007; Lindahl et al., 2001). In this case, the model is a large-scale atomic configuration of many thousand atoms that is a statistically representative fragment of the material under study. An example is shown in Figure 11b. Finite size models, that is, models not subject to periodic boundary conditions, that are very appropriate for nanosized metallic particles (see Fig. 11a), semiconductor quantum dots (Pradhan

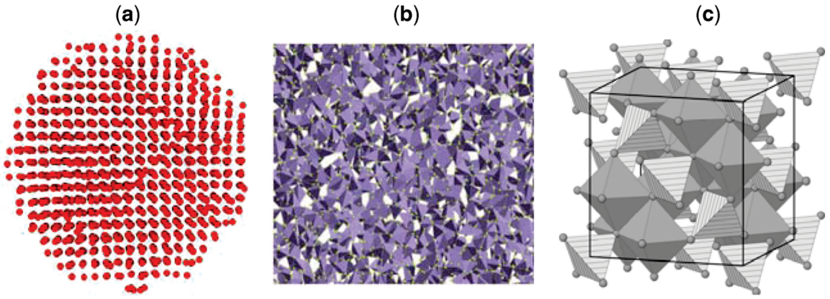

Figure 11. Structure models of 3 nm Au particles (**a**), $GeSe_2$ glass (**b**), and Mg ferrite (**c**) derived from fits to the respective experimental atomic PDFs. The model for Au particles features atoms (red circles) arranged in an face-centered cubic type structure (Petkov et al., 2005a). The model for $GeSe_2$ glass feature a random network of corner and edge-sharing Ge-Se_4 tetrahedra (Petkov and Messurier, 2010). The model (Gateshki et al., 2005) for Mg ferrite features a periodic cubic lattice of Fe-O_6 octahedral (gray) and Fe-O_4 tetrahedral units (shaded).

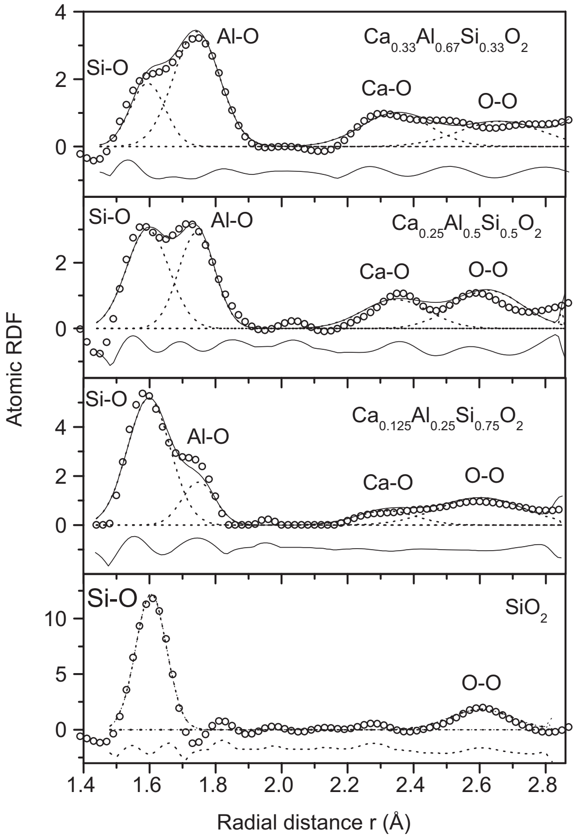

Figure 12. Gaussian fit to the first peaks in the RDFs for $Ca_{x/2}Al_xSi_{1-x}O_2$ ($x = 0$, 0.25, 0.5, 0.67) glasses. Experimental data: symbols; fitted data: full line; individual Gaussians: broken line; residual difference: full line (bottom). Peaks are labeled with the corresponding atomic pairs.

et al., 2007), or large organic molecules (Petkov et al., 2005b) can also be tested and refined against atomic PDFs. Successful attempts of using atomic PDFs for *ab initio* structure determination are also known (Juhas et al., 2006). In the atomic PDF-based structure determination process, plausible constraints based on a priori knowledge about material's chemistry, density, local coordination (e.g., from complimentary NMR or EXAFS experiments), and others are often needed to be employed to discriminate between competing solutions. Note, atomic PDFs are one-dimensional, spherically averaged representation of the atomic arrangement so the uniqueness of the three-dimensional structure solution found by atomic PDFs analysis is not always guaranteed.

SAMPLE PREPARATION

Atomic PDFs analysis can be done on samples of any size, shape, and phase state so long those can be mounted on a typical in-house or synchrotron XRD instrument. No special sample preparation is necessary though optimizing the sample size and shape with respect to maximizing the scattered intensities and reducing sample-related unwanted scattering is highly recommended, anytime it is possible. Also, a careful choice of the XRD data collection geometry, that is, reflection versus transmission versus capillary, should be made according the particular sample's phase state (Klug and Alexander, 1974; Thijsse, 1984).

SPECIMEN MODIFICATION

X-ray diffraction is a nondestructive technique. Samples measured remain completely unaltered which is a great advantage comparing with other material's structure characterization techniques such as electron microscopy and diffraction for example. Rarely organic materials can become damaged by the high flux of synchrotron radiation x-rays. Therefore, such samples should not be overexposed but only measured as long as necessary to obtain good statistical accuracy.

PROBLEMS

Typical problems include distortions of the PDFs peak shape (e.g., see Fig. 5), appearance of false PDF peaks (e.g., see Fig. 6) and/or shifts in PDFs peaks positions due to misalignment of the XRD instrument or errors in the x-ray wavelength calibration. Various sources of errors and their particular effect on atomic PDFs are discussed in (Peterson et al., 2003; Qiu et al., 2004b; Petkov and Danev, 1998). To minimize errors in atomic PDFs: (i) the XRD instrument should be carefully aligned, (ii) x-ray wavelength well calibrated, (iii) background and sample-related unwanted scattering minimized by a careful optimization of the experimental setup, (iv) XRD data taken to high wave vectors, (v) in appropriate ΔQ steps, and (vi) each with a very good statistical accuracy. Estimates for the latter are given in (Toby and Egami, 1992). The so-collected XRD data should be carefully reduced to atomic PDFs using as precise as possible data for the chemical composition, density, and x-ray absorption factor of the actual sample measured. Simple measures of experimental atomic PDFs quality are described in (Klug and Alexander, 1974; Toby and Egami, 1992; Peterson et al., 2003). Software implementing these measures and correcting experimental atomic PDFs for moderate errors is available as well (Petkov and Danev, 1998). Common problems with the interpretation of atomic PDFs include misidentifying an experimental artifact feature (e.g., a PDF ripple due to the finite $Q_{\max}$ value) (Warren and Mozzi, 1975) as a structural feature or vice versa. To avoid such problems, the particular experimental details such as instrument resolution and $Q_{\max}$ should be precisely taken into account in the PDF fitting/structure refinement process. Also, structure models resulted from atomic PDFs analysis, in particular when reverse

Monte Carlo simulations are employed, may come out way too disordered, including predicting way too short/long bond lengths and/or way too distorted atomic coordination units unless suitable structure constraints/restraints are imposed on the structure modeling/refinement process. Simple checks for atomic bond lengths and angles feasibility and bond valence sums consistency using available software (Roux and Petkov, 2010) can be done to certify that such mishaps did not occur.

ACKNOWLEDGMENTS

Thanks are due NSF, DOE, NRL, and ICDD for providing funds over several years for atomic PDFs studies, results of which are shown in this paper. Also, thanks are due to Th. Proffen for generating Fig. 2.

LITERATURE CITED

Chupas, P. J., Qiu, X., Hanson, J. C., Lee, P. L., Grey, C. P., and Billinge, S. J. L. 2003. Rapid-acquisition pair distribution function (RA-PDF) analysis. *J. Appl. Cryst.* 36: 1342–47.

Czichos, H., Saito T., and Smith, L. (eds.). 2006. Handbook of Materials Measurements Methods. Springer. Berlin

David, W. I. F., Shakland, K., McCusker, L. B., and Baerlocher, Ch.edts. 2002. Structure Determination from Powder Diffraction. Oxford University Press. Oxford

Egami, T. and Billinge S. J. L. 2003. Underneath the Bragg peaks: Structural Analysis of Complex Materials. Pergamon Press, Elsevier Ltd. New York

Farrow, C. L., Juhás, P., Liu, J. W., Bryndin, D., Božin, E. S., Bloch, J., Proffen, Th., and Billinge, S. J. L. 2007. PDFfit2 and PDFgui: computer programs for studying nanostructure in crystals. *J. Phys.: Condens. Matter* 19: 335219.

Farrow, C. L. and Billinge, S. J. L. 2009. Relationship between the atomic pair distribution function and small-angle scattering: Implications for modeling of nanoparticles. *Acta Cryst. A* 65:232–239.

Farrow, C. L., Shaw, M., Kim, H., Juhas, P., and Billinge, S. J. L. 2011. Nyquist–Shannon sampling theorem applied to refinements of atomic pair distribution functions. *Phys. Rev. B* 84:134105–7.

Gateshki, M., Petkov, V., Pradhan, S. K., and Vogt, T. 2005. Structure of nanocrystalline $MgFe_2O_4$ from x-ray diffraction, Rietveld and atomic pair distribution function analysis *J. Appl. Cryst.* 38:772–79.

Gateshki, M., Niederberger, M., Deshpande, A. S., Ren, Y., and Petkov, V. 2007. Atomic-scale structure of nanocrystalline CeO_2–ZrO_2 oxides by total x-ray diffraction and pair distribution function analysis, *J. Phys.: Condens Matter.*, 19:156205–12.

Gereben, O., Jovari, P., Temleitner, L. and Pusztai, L. 2007. A new version of the RMC++ reverse Monte Carlo programme, aimed at investigating the structure of covalent glasses. *J. Optoelectron. Adv. Mater.* 9:3021–7.

Giacovazzo, C. (ed.). 1998. In Fundamentals of x-ray crystallography. Oxford University Press.

Gilbert, B., Huang, F., Waychunas, G. A., and Banfield, J. F. 2004. Nanoparticles: Strained and stiff. *Science* 305:651–654.

Hahn, T. (ed.). 2002. International Tables for Crystallography. Volume A. Kluwer Academic Publishers. Dordrecht, The Netherlands

Hajdu, F. and Palinkas, G. 1972. On the determination of the absolute intensity of X-rays scattered by a non-crystalline specimen. *J. Appl. Cryst.* 5:395–401.

Jeong, I. K., Proffen, Th., Mohiuddin-Jacobs, F., Billinge, S. J. L. 1999 Measuring correlated atomic motion using X-ray diffraction. *J. Phys. Chem.* 103:921–924.

Juhas, P., Cherba, D. M., Duxbury, P. M., Punch, W. F., and Billinge, S. J. L. 2006. Ab initio determination of solid-state nanostructure. *Nature* 440:655–658.

Keen, D. A. 2001. A comparison of various commonly used correlation functions for describing total scattering. *J. Appl. Cryst.* 34:172–177.

Klug, P. K. and Alexander, L. E. 1974. X-Ray Diffraction Procedures: For Polycrystalline and Amorphous Materials. 2nd ed., John Wiley & Sons, Inc. New York

Kodama, K., Iikibo, S., Taguchi, T., and Shamoto, S. 2006. Finite size effects of nanoparticles on the atomic pair distribution functions. *Acta Cryst.* A 62:444–453.

Kohara, S., Suzuya, K., Kashihara, Y., Matsumoto, N., Umesaki, N., and Sakai, I. 2001. A horizontal two-axis diffractometer for high-energy x-ray diffraction using synchrotron radiation on bending magnet beamline BL04B2 at SPring-8. *Nucl. Instr. and Meth.* A 467–468:1030–33.

Korsunsky, V. I., Neder, B. R., Hofman, A., Dembski, S., Graf, Ch., and Ruhl, E. 2007. Aspects of the modeling of the radial distribution function for small nanoparticles. *J. Appl. Cryst.* 40:975–985.

Kuhs, W. F. and Lehmann, M. S. 1983. The structure of the ice Ih by neutron diffraction. *J. Phys. Chem.* 87: 4312–13.

Lee, J. H., Aydiner, C. C., Almer, J., Bernier, J., Chapman, K. W., Chupas, P. J. Haeffner, D., Kump, K., Lee, P. L., Lienert, U., Miceli, A., and Vera, G. 2008a. Synchrotron applications of an amorphous silicon flat-panel detector. *J. Synchrotr. Rad.* 15:477–488.

Lee, P. L., Shu, D., Ramanathan, M., Preissner, C., Wang, J., Beno, M. A., Von Dreele, R. B. Ribaud, L., Kurtz, Ch., Antao, S. M. Jiao, X., and Toby, B. H. 2008b. A twelve-analyzer detector system for high-resolution powder diffraction. *J. Synchr. Rad.* 15:427–32.

Lindahl, E., Hess, B., and Spoel, D. 2001. GROMACS 3.0: A package for molecular simulation and trajectory analysis. *J. Mol. Modeling*, 7:306–17.

Malenkov, G. 2009. Liquid water and ices: Understanding the structure and physical properties. *J. Phys.: Condens. Matter.* 21:283101–35.

Midgley, P. A. and Dunin-Borkowski, R. E. 2009. Electron tomography and holography in materials science. *Nat. Mat.* 8:271–280.

Mullen, K. and Levin, I. 2011. Mitigation of errors in pair distribution function analysis of nanoparticles. *J. Appl. Cryst.* 44:788–97.

Neder, R. B. and Proffen, Th. 2008. Diffuse scattering and defect structure simulations. A Cook Book using the Program DISCUS. Oxford University Press. Oxford

Page, Y. Le and Donnay, G. 1976. Refinement of the crystal structure of low-quartz. *Acta Cryst.* 32:2456–2459.

Peterson, P. F., Bozin, E. S., Proffen, Th., and Billinge, S. J. L. 2003. Improved measures of quality of atomic pair distribution function quality. *J. Appl. Cryst.* 36:53–64.

Petkov, V. and Danev, R. 1998. IFO—a program for image reconstruction-type calculation of atomic distribution functions for disordered materials. *J. Appl. Cryst.* 31:609–19.

Petkov, V., Jeong, I-K., Chung, J. S., Thorpe, M. F., Kycia, S. and Billinge S. J. L. 1999. High-real space resolution measurement of the local structure of In $_x$Ga $_{1-x}$ As semiconductor alloys using X-ray diffraction. *Phys. Rev. Lett.* 83:4089–92.

Petkov, V., Billinge, S. J. L., Sashtri, S., and Himmel, B. 2000. Polyhedral units and connectivity in calcium aluminosilicate glasses from high-energy x-ray diffraction. *Phys. Rev. Lett.* 85:3436–9.

Petkov, V., Billinge, S. J. L., Larson, P., Mahanti, S. D., Vogt, T., Rangan, K. K., and Kanatzidis, M. 2002. Structure of nanocrystalline materials using atomic pair distribution function analysis: Study of $LiMoS_2$ *Phys. Rev. B.* 65: 092105.

Petkov, V., Peng, Y., Williams, G., Huang, B., Tomalia, D., and Ren, Y. 2005a. Structure of gold nanoparticles suspended in water studied by x-ray diffraction and computer simulations, *Phys. Rev. B* 72:195402–8.

Petkov, V., Parvanov, V., Tomalia, D., Swanson, D., Bergstrom, D., and Vogt, T. 2005b. 3D structure of dendritic and hyper--branched macromolecules by x-ray diffraction", *Solid State Commun.* 134*:* 671–75.

Petkov, V. 2008 Nanostructure by high-energy XRD. *Mater. Today* 11:28–38.

Petkov, V., Cozzoli, P. D., Buonsanti, R., Cingolani, R., and Ren, Y. 2009. Size, shape and internal atomic ordering of nanocrystals by atomic pair distribution functions: a comparative study of gamma-Fe_3O_3 nanosized spheres and tetrapods. *J. Am. Chem. Soc.* 131:14264–6.

Petkov, V. and Shastri, S. 2010. Element-specific view of the atomic ordering in materials of limited structural coherence by high-energy resonant x-ray diffraction and atomic pair distribution functions analysis: A study of PtPd nanosized catalysts. *Phys. Rev. B* 81:165428.

Petkov, V., Selbach, S. M., Einarsrud, M.-A., Grande, T., and Shastri, S. D. 2010a. Melting of Bi-sublattice in nanosized $BiFeO_3$ perovskite by resonant x-ray diffraction. *Phys. Rev. Lett.* 105:185501–4.

Petkov, V., Moreels, I., Hens, Z., and Ren, Y. 2010b. PbSe quantum dots: Finite, off-stoichiometric, and structurally distorted. *Phys. Rev. B* 81:241304–4.

Petkov, V. and Messurier, D. Le. 2010. Atomic-scale structure of $GeSe_2$ glass revisited: a continuous or broken network of Ge-$(Se_{1/2})_4$ tetrahedra. *J. Phys.: Condens. Matter* 22: 115402–6.

Pradhan, S. K., Deng, Z. T., Tang, F., Wang, C., Ren, Y., Moeck, P., and Petkov, V. 2007. 3D structure of CdX ($X = Se$, Te) nanocrystals by total x-ray diffraction. *J. Appl. Phys.* 102:044304–7.

Qiu, X., Thompson, J. W., and Billinge, S. J. L. 2004a. PDFgetX2: A GUI driven program to obtain the pair distribution function from X-ray powder diffraction data. *J. Appl. Cryst.* 37:678–78.

Qiu, X., Bozin, E. S., Juhas, P., Proffen, Th., and Billinge, S. J. L. 2004b. Reciprocal-space instrumental effects on the real-space neutron atomic pair distribution function. *J. Appl. Cryst.* 37:110–16.

Roux, S. Le, Martin, S., Christensen, R., Ren, Y., and Petkov, V. 2011. Three dimensional structure of multicomponent $(Na_2O)_{0.35}$ $[(P_2O_5)_{1-x}$ $(B_2O_3)_x]_{0.65}$ glasses by high energy X-ray diffraction and constrained reverse Monte Carlo simulations. *J. Phys.: Condens. Matter* 23:035403.

Roux, S. Le and Petkov, V. 2010. ISAACS—Interactive structure analysis of amorphous and crystalline systems. *J. Appl. Crystallogr.* 43:181–85.

Ruland, W. 1964. The separation of coherent and incoherent Compton x-ray scattering. *Brit. J. Appl. Phys.* 15: 1301–07.

Samy, A. Dinnebier, R. E. Smaalen, S. Van 2010. Maximum entropy method and charge flipping, a powerful combination to visualize the true nature of structural disorder from in situ x-ray powder diffraction data. *Acta Cryst. B* 66: 184–195.

Smith, D. K. and Jenkins, R. 1996. The powder diffraction file: Past, present, and future. *J. Res. Natl. Inst. Stand. Technol.* 101:259–271.

Soper, A. K. and Barney, E. R. 2011. Extracting the pair distribution function from white-beam X-ray total scattering data. *J. Appl. Cryst.* 44:714–26.

Thijsse, B. J. 1984. The accuracy of experimental radial distribution functions for metallic glasses. *J. Appl. Cryst.* 17:61–76.

Toby, B. H. and Egami, T. 1992. Accuracy of pair distribution function analysis applied to crystalline and non-crystalline materials. *Acta Cryst. A* 48:336–346.

Warren, B. E. 1934 The diffraction of X-rays in glass. *Phys. Rev. B.* 45:657–661.

Warren, B. E. and Mozzi, R. L. 1975. The termination effect for amorphous patterns. *J. Appl. Cryst.* 8:674–677.

Wagner, C. N. J. 1969. Structure of amorphous alloy films. *J. Vac. Sci. Tech.* 6:650–657.

Zachariasen, W. H. 1932. The atomic arrangement in glass. *J. Am. Chem. Soc.* 54:3841–3851.

KEY REFERENCES

Egami and Billinge, 2003. See above.

This book is an excellent summary of the atomic PDFs analysis and its application to crystals with intrinsic disorder.

Keen, 2001. See above.

This paper gives an overview of the various definitions of atomic PDFs used by the scientific community.

Klug and Alexander, 1974. See above

This book presents a detailed explanation of the principles of traditional powder XRD and its extension into atomic PDFs analysis.

Thijsse, 1984. See above.

This article provides a detailed account of XRD experiments aimed at atomic PDFs analysis.

Wagner, 1969. See above.

The paper introduces the most frequently used atomic PDF definition.

First publication of RAD back in 1989....

A.22

Machine Computation	(*a*)	(*b* (i))	(*b* (ii))	(*b* (iii))	(*c*)
FMLS	2:53	1:25	4:15	4:05	12:20
BDLS	1:17	0:46	2:10	2:21	5:02
DMAP	0:55	0:43	2:17	2:10	4:52

The Weitek 3167 coprocessor is twice as fast as the 80387 and the IBM version on a 3090/200 is more than 20 times as fast as the VAX version.

References

Brown, I. D. (1983). *Acta Cryst.* A**39**, 216–224.

Gabe, E. J. (1988). *Crystallographic Computing* 4, edited by N. W. Isaacs & M. R. Taylor, pp. 381–392. Oxford Univ. Press/IUCr.

Gabe, E. J. & Lee, F. L. (1981). *Acta Cryst.* A**37**, C339.

Gabe, E. J., Lee, F. L. & Le Page, Y. (1985). *Crystallographic Computing* 3, edited by G. M. Sheldrick, C. Krüger & R. Goddard, pp. 167–174. Oxford: Clarendon Press.

Johnson, C. K. (1971). *ORTEP*II. Report ORNL-3794, revised. Oak Ridge National Laboratory, Tennessee, USA.

Larson, A. C. (1969). *Acta Cryst.* A**25**, S1.

Larson, A. C. & Gabe, E. J. (1978). *Computing in Crystallography*, edited by H. Schenk, R. Olthof-Hazekamp, H. van Koningsveld & G. C. Bassi, pp. 81–89. Delft Univ. Press.

Le Page, Y. (1982). *J. Appl. Cryst.* **15**, 255–259.

Le Page, Y. (1987). *J. Appl. Cryst.* **20**, 264–269.

Le Page, Y. (1988). *J. Appl. Cryst.* **21**, 983–984.

Le Page, Y. & Gabe, E. J. (1979). *J. Appl. Cryst.* **12**, 464–466.

Maguire, M. (1982). *Int. J. Man Mach. Stud.* **16**, 237

Main, P., Fiske, S. J., Hull, S. E., Lessinger, L., Germain, G., Declercq, J.-P. & Woolfson, M. M. (1980). *MULTAN*80. *A System of Computer Programs for the Automatic Solution of Crystal Structures from X-ray Diffraction Data.* Univs. of York, England, and Louvain, Belgium.

Motherwell, W. D. S. & Clegg, W. (1978). *PLUTO.* Program for plotting molecular and crystal structures. Univ. of Cambridge, England.

J. Appl. Cryst. (1989). **22**, 387–389

***RAD*, a program for analysis of X-ray diffraction data from amorphous materials for personal computers.**

By V. Petkov, *Sofia University, Department of Solid State Physics, Sofia-1126, Bulgaria*

(*Received* 21 *May* 1988; *accepted* 10 *February* 1989)

Abstract

RAD is an interactive computer program for radial distribution analysis of X-ray diffraction data from amorphous materials. *RAD* has been written in Fortran 77 and runs on IBM PC/XT/AT or compatible computers.

1. Introduction

The radial distribution function $4\pi r^2\rho(r)$ (RDF) is used to characterize amorphous structures. It represents the number of atoms in a spherical shell of radius r and unit thickness. The function is zero for values of r less than the hard-sphere diameter of the atoms and modulates about $4\pi r^2\rho_0$ for larger values of r, where ρ_0 is the average atomic density of the amorphous material. Peaks in the RDF(r) indicate frequently occurring atom–atom distances; the area under a peak is equal to the average number of atom pairs within a particular range of distances (Klug & Alexander, 1954).

The reduced RDF, $G(r) = 4\pi r[\rho(r) - \rho_0]$, is associated by a Fourier transformation with the interference function $i(s)$, which is the structure-dependent part of the experimental X-ray diffraction data. In the program *RAD* the interference function is defined, following Pings & Waser (1968), as

$$i(s) = \left[I_a^{\mathrm{coh}}(s) - \sum_{i=1}^{n} x_i f_i^2(s) \right] \Big/ \left[\sum_{i=1}^{n} x_i f_i(s) \right]^2 \qquad (1)$$

where $s = 4\pi(\sin\theta)/\lambda$, 2θ is the scattering angle, λ the wavelength, f_i are the atomic scattering factors, x_i the molar fractions of components, n the number of atomic species, and $I_a^{\mathrm{coh}}(s)$ is the coherently scattered intensity in electron units.

The aim of the radial distribution analysis is to evaluate the RDF(r) as the Fourier transform of the $i(s)$, which in turn can be obtained from the experimental intensities $I(s)$. The total scattered intensity $I(s)$ is related to $I_a^{\mathrm{coh}}(s)$ (Wagner, 1969*a*), neglecting the small-angle and multiple scattering, by

$$I_a^{\mathrm{coh}}(s) = \beta[I(s) - I_b(s)]/[P(s)A(s)] - M(s)I_a^{\mathrm{inc}}(s) \qquad (2)$$

where β is an unknown normalization constant, $I_b(s)$ is the background scattering (from air, substrate *etc.*), $P(s)$ and $A(s)$ are the appropriate polarization and absorption factors respectively, $M(s)$ is the monochromator attenuation function, and $I_a^{\mathrm{inc}}(s)$ is the incoherent scattering in electron units scaled to one structural unit.

2. Outline of the program

The program consists of a main part and four subroutines (*SETUPD, DATRED, NORM, CALCRD*), where separate steps in processing the experimental intensities are performed.

The main program consists of input–output and control statements corresponding to the different options.

0021-8898/89/040387-03$03.00

The subroutine *SETUPD* creates the X-ray diffraction data file, which includes scattering angles and up to 750 intensity values, and a parameter data file, supplied by the user. The parameter data file includes the number of atomic species (up to ten) constituting the sample, the corresponding molar fractions x_i and the atomic numbers Z_i, the atomic scattering-factor coefficients (Cromer & Mann, 1968), anomalous-dispersion corrections (Cromer, 1965), the wavelength λ, the linear absorption factor of the sample, the average atomic density of the amorphous material, the counter dead time, some control flags determined from the experimental configuration (geometry and monochromatization type) and the monochromator attenuation function (Ruland, 1964). Some of the numbers (density ρ_0 for instance) are not crucial in the data processing and can be neglected in the data file.

The subroutine *DATRED* uses as input data the X-ray diffraction data file and a parameter data file. The experimental data undergo the following treatments:

(i) Subtraction of background scattering according to Warren & Mozzi (1970) and Wagner (1969*b*).

(ii) Correction for counter dead time (Klug & Alexander, 1954).

(iii) Correction for polarization (Wagner, 1978; Thijsse, 1984) depending on the type of monochromatization.

(iv) Correction for absorption (Wagner, 1969*a*) depending on the geometry.

(v) The missing values between $2\theta = 0$ and the first experimental data are derived by linear extrapolation to the origin.

(vi) The corrected XRD data are smoothed (Savitzky & Golay, 1964), calculated in steps of $\Delta s = 0{\cdot}05$ from $s = 0$ to $s_{\max} = 4\pi(\sin\theta_{\max})/\lambda$ by means of a cubic spline interpolation and stored as a new data file.

The subroutine *NORM* uses a corrected data file from *DATRED* and the parameter data file as input. The independent coherent scattering,

$$\sum_{i=1}^{n} x_i f_i^2(s), \tag{3}$$

the sharpening factor,

$$\left[\sum_{i=1}^{n} x_i f_i(s)\right]^2, \tag{4}$$

and the incoherent scattering,

$$I_a^{\rm inc} = (\lambda/\lambda')^2 \sum_{i=1}^{n} x_i Z_i (b_i s)^{a_i}/[1+(b_i s)^{a_i}], \tag{5}$$

where a_i, b_i are semi-empirical expressions (Thijsse, 1984) and λ' is a modified wavelength, are here calculated.

The corrected X-ray diffraction data are scaled into electron units by the so-called high-angle method (Wagner, 1978):

$$\beta_{\rm HA} = \int_{s_{\min}}^{s_{\max}} \left[\sum_{i=1}^{n} x_i f_i^2(s) + M(s) I_a^{\rm inc}(s)\right] {\rm d}s \times \left\{\int_{s_{\min}}^{s_{\max}} [I(s) - I_b(s)][P(s)A(s)]^{-1}\,{\rm d}s\right\}^{-1}; \tag{6}$$

and the interference function $i(s)$ is calculated. As an independent check the integral

$$\int_{s_{\min}}^{s_{\max}} s^2 i(s)\,{\rm d}s = -2\pi^2\rho_0 \tag{7}$$

is computed according to the so-called sum rule (Wagner, 1978). When a satisfactory normalization is reached, by varying the low limit of integration $s_{\min}$ ($s_{\max}/2 < s_{\min} < s_{\max}$), the $i(s)$ data are stored as a new file.

The subroutine *CALCRD* uses as input an interference function data file and again the parameter data file. The reduced RDF $G(r)$ is calculated, properly damped (Klug & Alexander, 1954), as a Fourier transform of the $i(s)$:

$$G(r) = (2/\pi) \int_{s=0}^{s_{\max}} si(s) \sin(sr) \exp(-bs^2)\,{\rm d}s, \tag{8}$$

where b is the damping factor. A straight line is fitted to the $G(r)$ in the range $r = 0$–1 Å to obtain an estimate for the average atomic density ρ_0, on the basis of the expression

$$G(r) = -4\pi\rho_0 r \tag{9}$$

which holds only for small values of r. The RDF is calculated and the reduced RDF or optionally the RDF is stored as a new data file.

Residual errors in the $i(s)$, due to incorrect normalization of the data, may introduce spurious oscillations in the corresponding $G(r)$ in the region between the origin and the first peak. In order to avoid such errors a correction may be performed by means of repeated Fourier transformations (Kaplow, Strong & Averbach, 1965) and a new extended file (up to $2s_{\max}$) with corrected $i(s)$ values may be created. This file may be used as an input data file in the subroutine *CALCRD*.

RAD has been tested using published X-ray diffraction data for silica glass (Konnert & Karle, 1973). Fig. 1 shows the agreement between $si(s)$ values computed by *RAD* and by *RADILS* (Konnert & Karle, 1973). The program *RAD* proved to be useful for analysis of X-ray diffraction data from metallic glasses (Petkov, Apostolov & Skumryev, 1989).

3. Implementation of *RAD*

RAD consists of 1500 statements written in Microsoft Fortran 77 occupying about 110 Kbyte of core memory. It runs on IBM PC/XT/AT under PC-DOS 3.1. DOS utilities

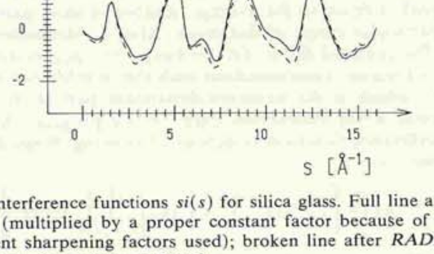

Fig. 1. Interference functions $si(s)$ for silica glass. Full line after *RAD* (multiplied by a proper constant factor because of the different sharpening factors used); broken line after *RADILS* (with permission from J. Karle).

and commands can be easily performed without leaving *RAD*.

During the data processing the raw data, the corrected data, the independent coherent and the incoherent scattering, the interference function $i(s)$, the reduced RDF and the RDF can be displayed by means of built-in graphic routines, if the computer is equipped with a CGA graphics card.

[illegible]ortran source code is available from the author on a floppy disk upon request.

I am indebted to Mr N. Zotov, IPM-BAN Sofia, for valuable discussions and advice.

References

CROMER, D. T. (1965). *Acta Cryst.* **18**, 17–23.

CROMER, D. T. & MANN, J. B. (1968). *Acta Cryst.* A**24**, 312–323.

KAPLOW, R., STRONG, S. & AVERBACH, B. (1965). *Phys. Rev. Sect. A*, **138**, 1336–1345.

KLUG, H. P. & ALEXANDER, L. E. (1954). *X-ray Diffraction Procedures*, p. 791. New York: Wiley.

KONNERT, J. H. & KARLE, J. (1973). *Acta Cryst.* A**29**, 702–710.

PETKOV, V., APOSTOLOV, A. & SKUMRYEV, V. (1989). *J. Non-Cryst. Solids*, **108**, 75–79.

PINGS, C. J. & WASER, J. (1968). *J. Chem. Phys.* **48**, 3016–3018.

RULAND, W. (1964). *Br. J. Appl. Phys.* **15**, 1301–1307.

SAVITZKY, A. & GOLAY, M. J. E. (1964). *Anal. Chem.* **36**, 1627–1640.

THIJSSE, B. J. (1984). *J. Appl. Cryst.* **17**, 61–76.

WAGNER, C. N. J. (1969*a*). *J. Vac. Sci. Tech.* **6**, 650–657.

WAGNER, C. N. J. (1969*b*). *Adv. X-ray Anal.* **12**, 50–70.

WAGNER, C. N. J. (1978). *J. Non-Cryst. Solids*, **31**, 1–40.

WARREN, B. E. & MOZZI, R. L. (1970). *J. Appl. Cryst.* **3**, 59–65.

J. Appl. Cryst. (1989). **22**, 389–393

*SIR*88 – a direct-methods program for the automatic solution of crystal structures.

By M. C. BURLA, *Dipartimento di Scienze della Terra, Università,* 06100 *Perugia, Italy,* M. CAMALLI, *Istituto 'G. Giacomello', Area della Ricerca CNR,* 00016 *Montelibretti, Roma, Italy,* G. CASCARANO and C. GIACOVAZZO, *Dipartimento Geomineralogico, Campus Universitario,* 70124 *Bari, Italy,* G. POLIDORI, *Dipartimento di Scienze della Terra, Università,* 06100 *Perugia, Italy,* R. SPAGNA, *Istituto 'G. Giacomello', Area della Ricerca CNR,* 00016 *Montelibretti, Roma, Italy* and D. VITERBO, *Dipartimento di Chimica, Università della Calabria,* 87030 *Rende (Cosenza), Italy*

(*Received* 20 *January* 1989; *accepted* 28 *March* 1989)

Abstract

*SIR*88 is an integrated package of computer programs for the solution of crystal structures. The package is based on the estimation of one- and two-phase structure seminvariants and three- and four-phase structure invariants according to the theory of representations [Giacovazzo (1977). *Acta Cryst.* A**33**, 933–944; (1980). *Acta Cryst.* A**36**, 362–372]. The program works in all the space groups and in most cases it is able to provide the correct solution without user intervention. Some prior information like the availability of a partial structure or of pseudotranslational symmetry is easily exploited to obtain the structure solution.

Introduction

The *SIR* (semi-invariants representations) package has been developed for solving crystal structures by direct methods. Its establishment was initiated some years ago. The present release, *SIR*88, is the second which we consider suitable for distribution and includes new features with respect to the previous version, *SIR*85. Even though *SIR*85 has been distributed by the authors to many laboratories worldwide over the last three years and has contributed to the determination of several difficult crystal structures, hitherto no published description of *SIR* has been available, except for the abstract presented at the IX ECM Meeting (Cascarano, Giacovazzo, Burla, Nunzi, Polidori, Camalli, Spagna & Viterbo, 1985).

The theoretical basis of *SIR* is the theory of representations (Giacovazzo, 1977, 1980*a*, *b*) according to which, for any structure invariant or seminvariant Φ, the set of diffraction magnitudes may be arranged in a sequence of subsets in order of their expected effectiveness (in the statistical sense) for the estimation of Φ. Thus different formulas can be used for estimating a given Φ, each exploiting a different subset of diffraction magnitudes, and therefore a different amount of prior information (faster access to this subset is guaranteed by storing all the reciprocal lattice in the central memory). In *SIR*88 one- and two-phase seminvariants and three- and four-phase invariants are estimated according to various formulas and subsequently used in the phasing process. Symmetry is used by *SIR*88 in a general way, so allowing the use of phase relationships in all space groups. A further goal of *SIR*88 is to minimize the amount of expertise the user has to bring to solving a crystal structure. To this end all decisions concerning data manipulations or appropriate choice of parameters can be assumed by the program. Therefore scientists untrained in direct methods or experienced people prepared to trust the *SIR*88 default mode can often solve crystal structures without personal intervention. However a large range of options is available to experienced crystallographers for choosing their own way of solving crystal structures.

0021-8898/89/040389-05$03.00

LI

One of the first applications of RAD back in 1989............

A.24

Journal of Non-Crystalline Solids 108 (1989) 75–79
North-Holland, Amsterdam

RADIAL DISTRIBUTION FUNCTIONS FOR RE_4Al_3 METALLIC GLASSES (RE = Pr, Gd, Tb, Dy)

V. PETKOV, A. APOSTOLOV and V. SKUMRYEV

Sofia University, Department of Solid State Physics, Sofia – 1126, Bulgaria

Received 29 July 1988
Revised manuscript received 13 October 1988

Using X-ray diffraction the radial distribution functions for RE_4Al_3 (RE = Pr, Gd, Tb, Dy) metallic glasses have been determined. The RE–RE atomic distances and first coordination numbers have also been estimated. A structural model based on spherically arranged dense packed tetrahedra is proposed.

1. Introduction

In recent years rare earths (RE)–aluminum (Al) amorphous alloys have been of considerable interest because of their peculiar magnetic and electrical properties [1,2 and refs. therein]. For elucidation of these properties a detailed knowledge of the structure is needed as physical properties are correlated to a great extent with the local atomic arrangement. However, structure investigations have not been carried out up to now. In the present paper we report the results of a structural study of RE_4Al_3 (RE = Pr, Gd, Tb, Dy) metallic glasses.

The glassy structure is usually expressed in terms of a radial distribution function RDF (r), which represents the number of atoms in a spherical shell of radius r and unity thickness. This characterization is, however, a one-dimensional picture of the three-dimensional atomic structure. The complete structural characterization, with determination of the structural building units and their arrangement, can be derived only from a structural model with RDF (r) and average atomic density ρ in correspondence with the experimental RDF (r) and ρ.

The aim of our structural study is to obtain the RDFs for RE_4Al_3 metallic glasses by means of the X-ray diffraction (XRD) method, to analyse them in detail and to propose an appropriate structural model on this basis. Quasi-crystalline structural models, based on randomly oriented microcrystalline regions of close-packed RE atoms, and non-crystalline structural models, based on a dense random packing of hard spheres, will be used as trial structural models since the RE_4Al_3 metallic glasses have no crystalline counterparts.

2. Experimental part

2.1. Sample preparation and characterization

The specimens were alloyed from 99.9% pure RE and Al by arc melting under an argon atmosphere. A number of ribbons – 30 μm thick and 2 mm wide – were obtained from each master alloy through the melt-spinning technique. A number of pieces were cut from adjacent sections of the ribbons and carefully arranged onto a rectangular plastic frame using adhesive tape as a substrate to form a single layer. The layers prepared in this way were used for the XRD measurements.

The chemical composition of all samples corresponds to the overall formula $RE_{57}Al_{43}$. Electron microprobe measurements in selected areas show there are slight fluctuations in the relative RE and

0022-3093/89/$03.50 © Elsevier Science Publishers B.V.
(North-Holland Physics Publishing Division)

Al concentration in the "wheel-quenched" and "air-quenched" ribbon sides only.

The density of the samples $\rho(Pr_4Al_3) = 5.9 \mp 0.1$ g/cm^3, $\rho(Gd_4Al_3) = 6.6 \mp 0.1$ g/cm^3, $\rho(Tb_4Al_3) = 6.9 \mp 0.1$ g/cm^3, $\rho(Dy_4Al_3) = 7.1 \mp 0.1$ g/cm^3, was measured using the Archimedes method.

2.2. *X-ray diffraction measurements*

The XRD data were collected by a semiautomatic powder diffractometer using filtered Mo k_α radiation and scintillation registration. Different collecting sequences were used for averaging the systematic effect of the apparatus' instability. The data were collected with the same sample several times so that at least 5000 counts were accumulated for each Bragg angle.

The linear absorption factors μt, measured by simple attenuation experiments, are of order of unity so the conditions are suitable for performing XRD measurements in symmetrical transmission geometry. As the transmission geometry has advantages in the small-angle region [3,4] but is not efficient in the high-angle region (because of the slower counting rate in comparison with the reflection) the following experimental procedure was adopted.

First, the samples were mounted in a symmetrical reflection geometry and scattered intensity collected in $\Delta 2\theta$ steps of 0.2° from $2\theta = 12°$ to 60° and $\Delta 2\theta = 0.4°$ from $2\theta = 60°$ to 145°.

Second, the samples were positioned in symmetrical transmission geometry and measurements performed in the range from $2\theta = 7°$ to 70° in steps of 0.2°.

Third, a consistency check between the transmission and the reflection data was performed [5]. If the test result were satisfactory a unique set of XRD data from $2\theta = 7°$ up to 145° was composed, combining the low-angle transmission data with the high-angle reflection data, otherwise the XRD data set was rejected and the measurements repeated. This procedure ensures XRD data free from systematic errors [5,6].

The background scattering was measured with only the substrate mounted on the goniometer axis.

2.3. *X-ray diffraction data processing*

The raw XRD data were corrected for background scattering, counter dead time, polarization and absorption. The missing values between $2\theta = 0°$ and $2\theta = 7°$ have been derived by means of a linear extrapolation. The corrected data were spline smoothed, recalculated in steps of $\Delta s = 0.05$ from $s = 0$ to $s_{max} = 4\pi \sin(\theta_{max})/\lambda = 16.8$ Å^{-1} and scaled into electron units by the so-called "high-angle" method. Only the coherently scattered intensity I_a^{coh} was extracted after removing the incoherent (Compton) scattering. The interference functions

$$I(s) = \left[I_a^{coh} - \sum_{i=1}^{n} x_i f_i^2(s) \right] \Big/ \left[\sum_{i=1}^{n} x_i f_i(s) \right]^2,$$

and the reduced RDFs

$$G(r) = (2/\pi) \int_{s=0}^{s_{max}} sI(s) \sin(sr)\, ds$$

where all symbols have the usual meaning, have been computed according to the Pings and Waser method [7].

Some residual errors in the $I(s)$, mainly occurring as a result of the incorrect normalization of the XRD data, introduce large spurious oscillations in the region between the origin and the first peak in the corresponding $G(r)$. For preventing such errors a correction was performed by means of repeated Fourier transforms in the way proposed by Kaplow, Strong and Averbach [8].

Figure 1 shows the uncorrected reduced interference function $F(s) = sI(s)$ for Gd_4Al_3 and the residual difference after the subtraction of the $F(s)$ corrected according to the method of Kaplow et al. Figure 2 shows the results of the same procedure but for the corresponding reduced RDF $G(r)$. As can be seen from these figures the change for all values of $F(s)$ is small, of the order of the data noise at high s values, but is enough to remove the ripples in the $G(r)$ at small values of r. The final interference functions $F(s)$ and the corresponding reduced RDFs $G(r)$ are shown respectively in figs. 3 and 4.

For checking the influence of the high-angle XRD data upon the final $G(r)$ values, the upper

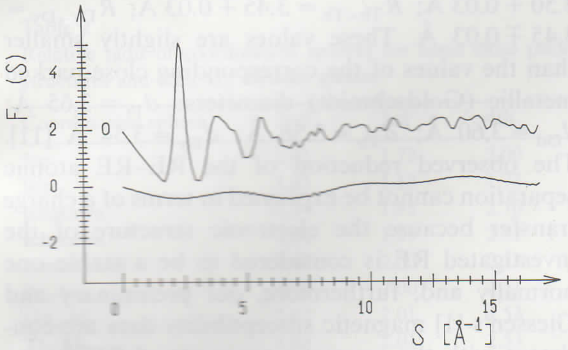

Fig. 1. The uncorrected reduced interference function $F(s)$ for Gd$_4$Al$_3$ and the residual difference after subtraction of the $F(s)$ corrected according to the method of Kaplow et al. [8].

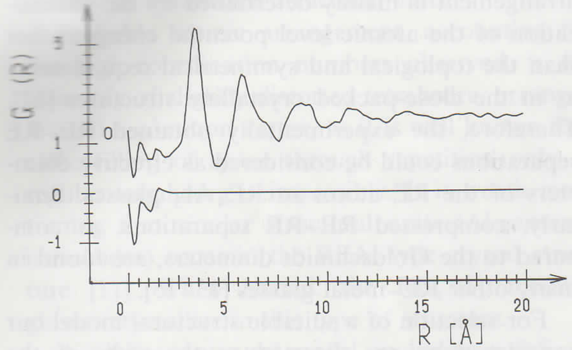

Fig. 2. The uncorrected reduced radial distribution function $G(r)$ for Gd$_4$Al$_3$ and the residual difference after the subtraction of the $G(r)$ corrected according to the method of Kaplow et al. [8].

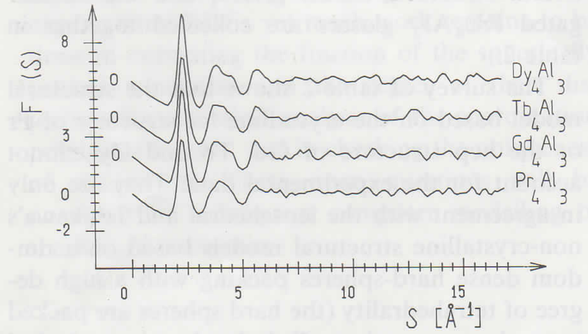

Fig. 3. Total reduced interference functions for RE$_4$Al$_3$ metallic glasses (with displaced zeroes).

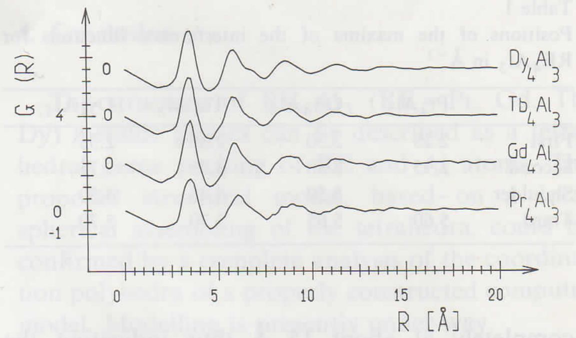

Fig. 4. Total reduced radial distribution functions for RE$_4$Al$_3$ metallic glasses (with displaced zeroes).

limit of integration $s_{\max}$ was changed up to $s_{\max}/2$. In addition, a complementary XRD experiment was performed for the Gd$_4$Al$_3$ sample, using Co K$_\alpha$ radiation and Ross balanced Fe–Mn filters. However it produced no qualitative changes in the $G(r)$. Therefore, a conclusion can be drawn that all details of the $G(r)$, including the weak shoulder on the second peak near $r = 7$ Å (see fig. 4), have physical meaning and the atom–atom separations and coordination numbers derived from RDFs are within the error limits stated below.

All of the above-mentioned calculations and corrections were performed on an IBM PC/XT with use of the program RAD [9].

3. Discussion

As shown in fig. 3 the $F(s)$ curves for all of the samples except Pr$_4$Al$_3$, are composed of a sharp first maximum, second maximum with a shoulder on its large-s side and subsequent small oscillations (due to the poor XRD data statistics). The shoulder of the second $F(s)$ peak for Pr$_4$Al$_3$ is not very strong but is still clearly visible. The positions of the maxima are listed in table 1. The values obtained for Gd$_4$Al$_3$ correspond with those reported by Buschow [10].

Figure 4 shows that the features of the reduced RDFs do not vary substantially with the constituent RE elements. For all samples the correlations between the atomic positions decrease with increase of the atom–atom separations and vanish

Table 1
Positions of the maxima of the interference functions for RE_4Al_3 in $Å^{-1}$

	Pr_4Al_3	Gd_4Al_3	Tb_4Al_3	Dy_4Al_3
First	2.25	2.30	2.35	2.35
Second	3.95	3.80	3.75	3.75
Shoulder	–	4.50	4.45	4.50
Third	5.60	5.65	5.70	5.70

completely at about 15 Å thus indicating the existence of a short-range topological order only.

It is commonly known that for multicomponent alloys the total $G(r)$, derived from a single diffraction experiment, is a sum of the partial reduced RDFs $G_{ij}(r)$,

$$G(r) = \sum_{i,j} w_{ij} G_{ij}(r),$$

where the weighting factor w_{ij} is an appropriate average value of the weighting function $w_{ij}(s)$ which varies slowly with s [3–5].

The weighting factor of the RE–RE pairs is predominant (more than 75%) for the samples under investigation. On the contrary, the contribution of the Al–Al pairs to the experimental RDF is negligible (only about 1%). Furthermore, the individual contributions of the RE–RE and the RE–Al pairs to the first RDFs maxima are not resolved because of the insufficient resolution of the XRD experiment ($s_{max} = 16.8$ $Å^{-1}$). Therefore, the area under the first peak of the RDFs is approximately equal to the average number of the nearest neighbours of the RE atoms, and the positions of the first maxima are strongly determined by the RE–RE separation. According to these considerations, the number of the RE nearest neighbours and the RE–RE atomic separation can be estimated on the basis of the total RDFs only.

The estimated number of RE nearest neighbours is as follows: $CN_{Pr} = 13.5 \mp 0.5$; $CN_{Gd} = 14.0 \mp 0.5$; $CN_{Tb} = 14.0 \mp 0.5$; $CN_{Dy} = 14.0 \mp 0.5$. Not surprisingly these values are high because coordination numbers higher than 12 are well known in the complex crystal structures of RE–Al alloys [11].

The estimated distances between the RE atoms are as follows: $R_{Pr-Pr} = 3.55 \mp 0.03$ Å; $R_{Gd-Gd} = 3.50 \mp 0.03$ Å; $R_{Tb-Tb} = 3.45 \mp 0.03$ Å; $R_{Dy-Dy} = 3.45 \mp 0.03$ Å. These values are slightly smaller than the values of the corresponding close packed metallic (Goldschmidt) diameters: $d_{Pr} = 3.65$ Å; $d_{Gd} = 3.60$ Å; $d_{Tb} = 3.56$ Å; $d_{Dy} = 3.54$ Å [11]. The observed reduction of the RE–RE atomic separation cannot be explained in terms of a charge transfer because the electronic structure of the investigated RE is considered to be a stable one normally and, furthermore, our preliminary and Giessen's [1] magnetic susceptibility data are consistent with the magnetic moments of RE^{3+} ions only. It should be mentioned that there is a difference between the Goldschmidt diameters determined from close-packed crystalline structures and the atomic diameters determined from RDFs for metallic glasses. In the latter the local atomic arrangement is mainly determined by the minimization of the atomic level potential energy rather than the toplogical and symmetrical requirements as in the close-packed crystalline structures [12]. Therefore, the experimentally obtained RE–RE separations could be considered as effective diameters of the RE atoms in RE_4Al_3 glasses. Similarly, compressed RE–RE separations, as compared to the Goldschmidt diameters, are found in many other RE–metal glasses [13–15].

For selection of a suitable structural model our considerations are directed to the radii of the coordination spheres estimated by the positions of the maxima in the RDFs. In this aspect, the relative radii of the coordination spheres for hexagonal close-packed (hcp) and face-centered cubic (fcc) crystalline structures, Ichikawa's dense random packing of hard spheres [16], the icosahedral structural model [17,18] and the investigated RE_4Al_3 glasses are collected together in table 2.

The survey of table 2 shows that the structural model based on the crystalline fcc structure of Pr or the hcp structure of Gd, Tb and Dy cannot account for the experimental data. They are only in agreement with the icosahedral and Ichikawa's non-crystalline structural models based on a random dense hard-spheres packing with a high degree of tetrahedrality (the hard spheres are packed in such a way that all holes have tetrahedral symmetry). This means that the metal atoms in

Table 2
Relative radii of coordination spheres for some close packed structures and RE_4Al_3 metallic glasses

Coordination sphere	2nd	3rd	4th
fcc	1.41	1.73	2.00
hcp	1.41	1.63	1.73
Ichikawa $^{+}$	1.74	1.95	2.70
Ichikawa $^{++}$	1.66	1.99	2.52
Icosahedral	1.67	2.00	2.53
Pr_4Al_3	1.70	2.00	2.51
Gd_4Al_3	1.67	2.01	2.53
Tb_4Al_3	1.68	2.01	2.53
Dy_4Al_3	1.67	2.00	2.49

$^{+}$ With a low degree of tetrahedrality.
$^{++}$ With a high degree of tetrahedrality.

RE_4Al_3 glasses are well approximated by an assembly of tetrahedral structural units.

Probable atomic arrangement, accounting for the high coordination numbers observed, is the assembly of slightly distorted tetrahedra, arranged around a common vertex, as it is well known that close filling of space through repetition only of regular tetrahedra is impossible. It is worth mentioning that similar structural units (Al-centered icosahedra) occur in the REAl-type crystal structure [11]. When heated, the RE_4Al_3 metallic glasses crystallize in this type of structure.

A similar structural model, including a definite amount of octahedra, has been proposed for Gd–Y metallic glasses by Laridjani and Sadoc [19]. There are only a few traces of octahedral structural units on the low-*r* side of the second RDF peaks of the investigated RE_4Al_3 metallic glasses (see fig. 4).

At least qualitatively, our structural model is capable of accounting for the peculiarities of the experimental RDFs yet much work remains to be done in estimating the fraction of the spherically packed tetrahedra and the degree of their distortion, for statistical analysis of the coordination polyhedra formed, and in checking the uniqueness of the model. These open questions will be answered by subsequent computer modelling of the RE_4Al_3 structure.

4. Conclusion

The structure of RE_4Al_3 (RE = Pr, Gd, Tb, Dy) metallic glasses can be described as a tetrahedral dense packing of RE and Al atoms. The proposed structural model, based on a local spherical assembling of the tetrahedra, could be confirmed by a complete analysis of the coordination polyhedra of a properly constructed computer model. Modelling is presently under way.

The authors are indebted to Mr. L. Bozukov and Mr. V. Kostadinov for their help in producing the RE_4Al_3 samples.

References

[1] B. Giessen, A. Hines and L. Kobacoff, IEEE Trans. Magn. 16 (1980) 1203.
[2] K. Shirakawa, K. Aoki and T. Masumoto, J. Non-Cryst. Solids 61&62 (1984) 1371.
[3] H. Klug and L. Alexander, in: X-ray Diffraction Procedures (Wiley, New York, 1954) p. 721.
[4] C. Wagner, J. Non-Cryst. Solids 42 (1980) 3.
[5] B. Thijsse, J. Appl. Cryst 17 (1984) 61.
[6] B. Thijsse and J. Sietsma, J. Non-Cryst. Solids 61&62 (1984) 361.
[7] C. Pings and J. Waser, J. Chem. Phys. 48 (1968) 3016.
[8] R. Kaplow, S. Strong and B. Averbach, Phys. Rev. A138 (1965) 1336.
[9] V. Petkov, J. Appl. Cryst., in press.
[10] K. Buschow, Sol. St. Commun. 27 (1978) 275.
[11] W. Pearson, in: Crystal Chemistry and Physics of Metals and Alloys (Wiley, New York, 1972).
[12] T. Egami and Y. Waseda, J. Non-Cryst. Solids 64 (1984) 113.
[13] M. Maurer, J. Friedt and G. Krill, J. Phys. F 13 (1983) 2389.
[14] S. Nandra and P. Grundy, J. Phys. F 7 (1977) 207.
[15] K. Fukuda, S. Katayama, T. Katayama, A. Nukui and A. Makisima, Jap. J. Appl. Phys. 25 (1986) 1640.
[16] T. Ichikawa, Phys. Stat. Sol. A29 (1975) 293.
[17] J. Sadoc, J. Dixmier and A. Guinier, J. Non-Cryst. Solids 12 (1973) 46.
[18] C. Briant and J. Burton, Phys. Stat. Sol. B85 (1978) 393.
[19] M. Laridjani and J. Sadoc, J. de Phys. 42 (1981) 1293.

More recent application of RAD

High Real-Space Resolution Measurement of the Local Structure of $\mathrm{Ga}_{1-x}\mathrm{In}_x\mathrm{As}$ Using X-Ray Diffraction

V. Petkov,[1] I-K. Jeong,[1] J. S. Chung,[1] M. F. Thorpe,[1] S. Kycia,[2] and S. J. L. Billinge[1]
[1]*Department of Physics and Astronomy and Center for Fundamental Materials Research, Michigan State University, East Lansing, Michigan 48824-1116*
[2]*Cornell High Energy Synchrotron Source, Cornell University, Ithaca, New York 14853*

(Received 7 June 1999)

High real-space resolution atomic pair distribution functions PDFs from the alloy series $\mathrm{Ga}_{1-x}\,\mathrm{ln}_x$ As have been obtained using high-energy x-ray diffraction. The first peak in the PDF is resolved as a doublet due to the presence of two nearest neighbor bond lengths, Ga-As and In-As, as previously observed using x-ray absorption fine structure. The widths of nearest, and higher, neighbor PDF peaks are analyzed by separating the broadening due to static atom displacements from the thermal motion. The PDF peak width is 5 times larger for distant atomic neighbors than for nearest neighbors. The results are in agreement with model calculations.

PACS numbers: 61.66.Dk, 61.43.Dq, 61.72.Dd

The average atomic arrangement of crystalline semiconductor alloys is usually obtained from the position and intensities of the Bragg peaks in a diffraction experiment [1], and the actual nearest neighbor and sometimes next nearest neighbor distances for various pairs of atoms by XAFS measurements [2]. In this Letter, we show how high-energy x-ray diffraction and the resulting high-resolution atomic pair distribution functions PDFs can be used for studying the local atomic arrangements in $\mathrm{Ga}_{1-x}\mathrm{In}_x\mathrm{As}$ alloys. We show that the first peak in the PDFs can be resolved as a doublet and, hence, the mean position and also the widths of the Ga-As and In-As bond length distributions determined. The detailed structure in the PDF can be followed out to very large distances and the widths of the various peaks obtained. We use the concentration dependence of the peak widths to separate the broadening due to static atom displacements from the thermal broadening. At large distances the static part of the broadening is shown to be up to 5 times larger than it is for nearest neighbor pairs. Using a simple valence force field model, we get good agreement with the experimental results.

Ternary semiconductor alloys, in particular $\mathrm{Ga}_{1-x}\mathrm{In}_x\mathrm{As}$, have technological significance because they allow important properties, such as band gaps, to be tuned continuously between the two end points by varying the composition x. Surprisingly, there is no complete experimental determination of the microscopic structure of these alloys. On average, both GaAs and InAs form in the zinc-blende structure where Ga or In and As atoms occupy two interpenetrating face-centered-cubic lattices and are tetrahedrally coordinated to each other [1]. However, both extended x-ray absorption fine structure (XAFS) experiments [2] and theory [3] have shown that Ga-As and In-As bonds do not take some average value but remain close to their *natural* lengths of $L^0_{\text{Ga-As}} = 2.437$ Å and $L^0_{\text{In-As}} = 2.610$ Å in the alloy. Because of the two different bond lengths present, the zinc-blende structure of $\mathrm{Ga}_{1-x}\mathrm{In}_x\mathrm{As}$ alloys becomes locally distorted. A number of authors [2–5] have proposed distorted local structures, but there have been limited experimental data available to date. The fully distorted structure is a prerequisite as an input for accurate band structure and phonon dispersion calculations [6].

The technique of choice for studying the local structure of semiconductor alloys has been XAFS [2,5]. However, XAFS provides information only about the immediate atomic ordering (first and sometimes second coordination shells) and all longer-ranged structural features remain hidden. To remedy this shortcoming, we have taken the alternative experimental approach of obtaining high-resolution PDFs of these alloys from high-energy x-ray diffraction data.

The PDF is the instantaneous atomic density-density correlation function which describes the local arrangement of atoms in a material [7]. The PDF, $G(r)$, is the sine Fourier transform of the experimentally observable total structure factor, $S(Q)$, where Q is the magnitude of the wave vector, given by

$$G(r) = \frac{2}{\pi} \int_0^{Q_{\max}} F(Q) \sin Qr \, dQ \,, \tag{1}$$

with $F(Q) = Q[S(Q) - 1]$. The total structure factor, $S(Q)$, is the normalized scattered intensity from the powder sample.

PDF analysis yields the real local structure, whereas an analysis of the Bragg scattering alone yields the average crystal structure. Determining the PDF has been the approach of choice for characterizing glasses, liquids, and amorphous materials for a long time [8]. However, its widespread application to study *crystalline* materials has been relatively recent [9]. Very high real-space resolution is required to differentiate the distinct Ga-As and In-As bond lengths present in $\mathrm{Ga}_{1-x}\mathrm{In}_x\mathrm{As}$. High real-space resolution is obtained by measuring $S(Q)$ to a very high value of Q ($Q_{\max} \geq 40$ Å^{-1}). An indium neutron absorption resonance rules out neutron measurements in the

0031-9007/99/83(20)/4089(4)$15.00

$Ga_{1-x}In_xAs$ system. We therefore carried out x-ray powder diffraction measurements. To access Q values in the vicinity of 40–50 $Å^{-1}$ it is necessary to use x rays with energies $\geq$50 keV. The experiments were carried out at the A2 24 pole wiggler beam line at Cornell High Energy Synchrotron Source (CHESS), which is capable of delivering intense x rays of energy 60 keV. Six powder samples of $Ga_{1-x}In_xAs$, with $x = 0.0$, 0.17, 0.5, 0.67, 0.83, and 1.0, were measured. The samples were made by standard methods and the details of the sample preparation will be reported elsewhere [10]. All measurements were done in symmetric transmission geometry at 10 K. The relative intensities of the Bragg peaks compare well with those expected from the crystal structure, suggesting that the samples are free of any significant texture. Low temperature was used to minimize thermal vibration in the samples, and hence to increase the sensitivity to static atomic displacements. A double crystal Si(111) monochromator was used. Scattered radiation was collected with an intrinsic germanium detector connected to a multichannel analyzer. The elastic component was separated from the incoherent Compton scattering before data analysis [10]. Several diffraction runs were conducted with each sample, and the resulting spectra averaged to improve the statistical accuracy. The data were normalized for flux, corrected for background scattering, detector deadtime and absorption, and divided by the average form factor to obtain the total structure factor, $S(Q)$ [7,8,11], using the program RAD [10,12]. Experimental reduced structure factors, $F(Q)$, are shown in Fig. 1. The corresponding reduced PDFs, $G(r)$, are shown in Fig. 2. The data for the Fourier transform were terminated at $Q_{\max} = 45$ $Å^{-1}$ beyond which the signal to noise ratio became unfavorable. This is a very high momentum transfer for x-ray diffraction measurements. For comparison, $Q_{\max}$ from a Cu K_α x-ray tube is less than 8 $Å^{-1}$.

Significant Bragg scattering (well-defined peaks) are immediately evident in Fig. 1 up to $Q \sim 35$ $Å^{-1}$ in the end members, GaAs and InAs. This implies that the samples have long range order and that there is little positional disorder (dynamic or static) on the atomic scale. The Bragg peaks disappear at much lower Q values in the alloy data: the samples are still long-range ordered but they have significant local positional disorder. At high-Q values, oscillating diffuse scattering is evident. This has a period of $2\pi/2.5$ $Å^{-1}$ and contains information about the shortest atomic distances in $Ga_{1-x}In_xAs$ alloys seen as a sharp first peak in $G(r)$ at 2.5 Å (see Fig. 2). In the alloys, this peak is split into a doublet as is clearly evident in Fig. 2; with a shorter Ga-As bond and a longer In-As bond. This peak is shown on an expanded scale in the inset to Fig. 3 for all the compositions measured. We determined the positions of the two subcomponents of the first PDF peak, i.e., the mean Ga-As and In-As bond lengths, and the results are shown in Fig. 3. Also shown is the room temperature result previously obtained in the XAFS study of Mikkelson and Boyce [2]. There is clearly good agreement. The PDF-based bond lengths are shifted to smaller lengths by about 0.012 Å since our data were measured at 10 K, whereas the XAFS experiments were at room temperature. The nearest neighbor peak is the only peak which is sharp in the experimental PDFs, as can be seen in Fig. 2. From the second-neighbor onwards the significant atomic displacements in the alloy samples result in broad atom-pair distributions without any resolvable splitting. Model calculations show that this broadening is intrinsic and not due to any experimental limitations. The PDF peak widths in $Ga_{1-x}In_xAs$ were quantified by fitting individual peaks using Gaussians convoluted with sinc functions with FWHM 0.086 Å to account for the experimental resolution coming from the finite $Q_{\max}$. At low r this was accomplished by fitting individual peaks. At high r where there is significant peak overlap a profile fitting regression program was used [13]. The resulting mean-square Gaussian standard deviations are shown in Fig. 4. One can see that the static contribution to the PDF peak width on 2nd and higher neighbors is up to 5 times larger than on the near neighbors. The peak width has a maximum at a composition $x = 0.5$ and affects the common (As) more than the mixed (metal) sublattice.

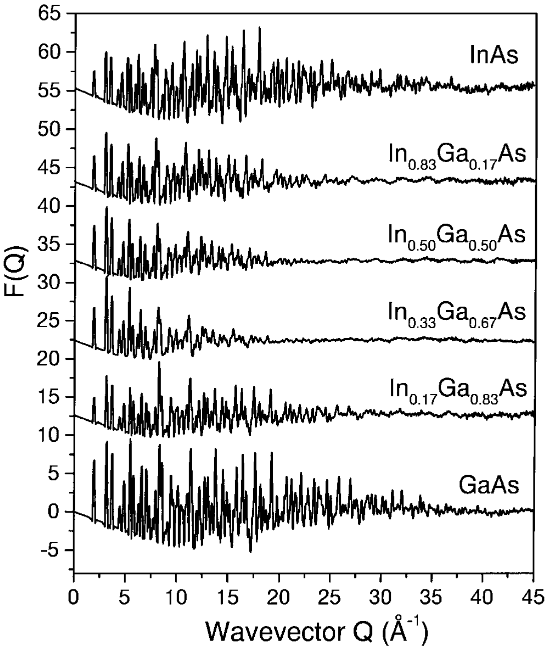

FIG. 1. The reduced structure factor, $F(Q)$, for $Ga_{1-x}In_xAs$ measured at 10 K for various concentrations.

In order to better understand these results, we have modeled to the static and thermal disorder in the alloy by using a Kirkwood potential [14]. The potential contains nearest neighbor bond stretching force constants α and force constants β that couple to the change in the angle between adjacent nearest neighbor bonds. We choose these parameters to fit the end members [3] with $\alpha_{\text{Ga-As}} = 96$ N/m, $\alpha_{\text{In-As}} = 97$ N/m, $\beta_{\text{Ga-As-Ga}} = \beta_{\text{As-Ga-As}} = 10$ N/m, and

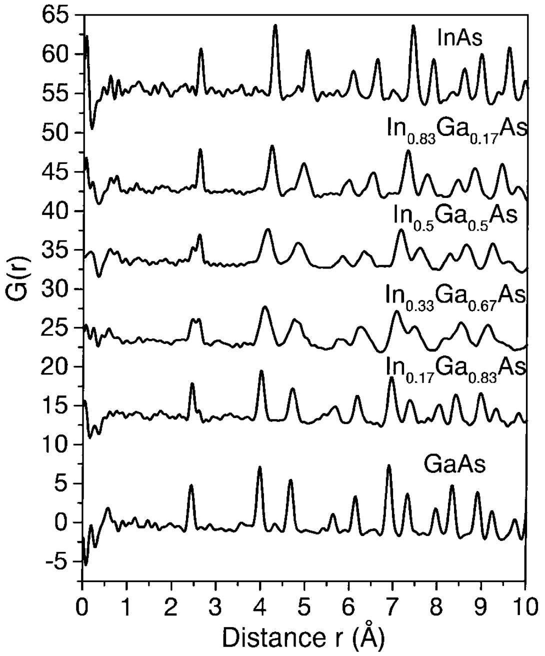

FIG. 2. The reduced PDF, $G(r)$, for $Ga_{1-x}In_xAs$ measured at 10 K for various concentrations.

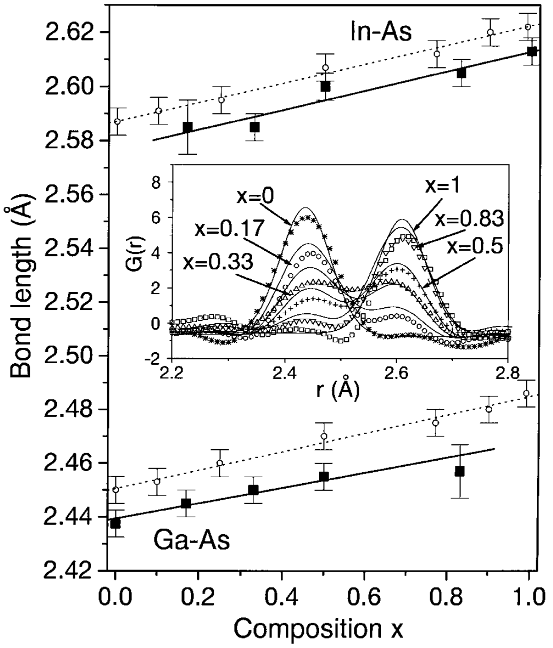

FIG. 3. Solid symbols: Ga-As and In-As bond lengths vs composition as extracted from the present PDFs. Open symbols: room-temperature XAFS results from Ref. 2. Inset: Split nearest neighbor PDF peak from the data (symbols) and the model (solid lines).

$\beta_{\text{In-As-In}} = \beta_{\text{As-In-As}} = 6$ N/m. The additional angular force constant required in the alloy is taken to be the geometrical mean, so that $\beta_{\text{Ga-As-In}} = \sqrt{(\beta_{\text{Ga-As-Ga}}\beta_{\text{In-As-In}})}$. We have constructed a series of cubic 512 atom periodic supercells in which the Ga and In atoms are distributed randomly according to the composition x. The system is relaxed using the Kirkwood potential to find the displacements from the virtual crystal positions. The volume of the supercell is also adjusted to find the minimum energy. Using this strained static structure, a dynamical matrix has been constructed, and the eigenvalues and eigenvectors found numerically. From this the Debye-Waller factors for all the individual atoms in the supercell can be found and hence the PDF of the model by including the Gaussian broadening of all the subpeaks, which is the correct procedure within the harmonic approximation [15]. The model PDF is plotted with the data in the inset to Fig. 3 and in Fig. 5. The agreement at higher r is comparable to that in the r range shown. All the individual peaks shown in the figures consist of many Gaussian subpeaks. The overall fit to the experimental $G(r)$ is excellent, and the small discrepancies in Fig. 5 between theory and experiment are probably due to small residual experimental errors. Note that in comparing with experiment, the theoretical PDF has been convoluted with a sinc function to incorporate the truncation of the experimental data at $Q_{\max} = 45$ Å. The technique discussed above could be extended using a better force constant model with more parameters, but does not seem necessary at this time.

The contributions from static displacements and thermal motion to the widths of the individual peaks in the reduced PDF act independently as expected and as confirmed by our supercell calculations described in the

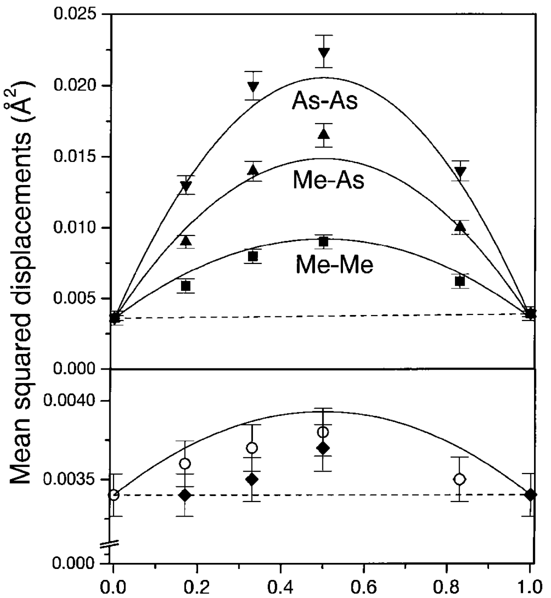

FIG. 4. Square of the PDF peak widths for far neighbors (top panel) and nearest neighbors (lower panel) separated by sublattice type. Symbols: values from the data. In the lower panel the open symbols are for the Ga-As bond and the closed symbols for the In-As bond. Solid lines: theory. See text for details. The mean-square static and thermal distortions are added. Here Me represents both the metals Ga and In, which behave in the same way. Note that the scale in the lower panel is expanded by a factor of 10 compared to the upper panel.

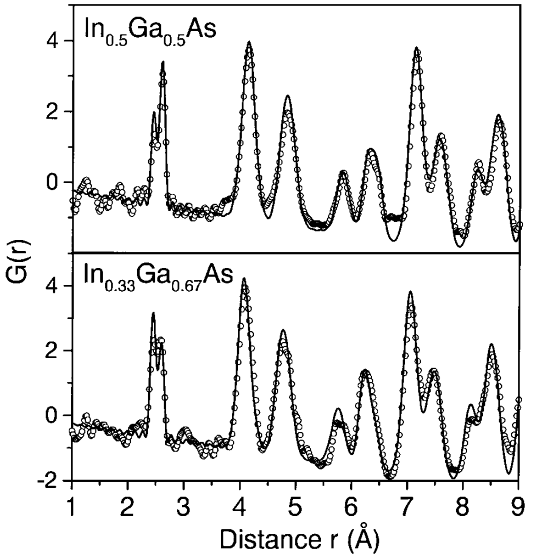

FIG. 5. Experimental (open circles) and theoretical (solid line) PDFs for $Ga_{1-x}In_xAs$ for concentrations $x = 0.5$ and $x = 0.33$.

previous paragraph. We therefore expect the squared width Δ to be a sum of the two parts. The thermal part σ is almost independent of the concentration, and we fit σ^2 by a linear function of the composition x between the two end points in Fig. 4. To better understand the strain, it is convenient to assume that all the force constants are the same and independent of chemical species. Then it can be shown [16] for any such model that

$$\Delta_{ij}^2 = \sigma_{ij}^2 + A_{ij}x(1 - x)(L_{\text{In-As}}^0 - L_{\text{Ga-As}}^0)^2, \qquad (2)$$

where the subscripts ij refer to the two atoms that lead to a given peak in the reduced PDF. For the Kirkwood model the A_{ij} are functions of the ratio of force constants β/α only. It further turns out that the A_{ij} are independent of whether a site in one sublattice is Ga or In, so we will just refer to that as the metal site. By taking mean values from the force constants used in the simulation we find that $\beta/\alpha = 0.83$, and that for nearest neighbor pairs $A_{ij} = 0.0712$. For more distant pairs the motion of the two atoms becomes uncoupled so that $A_{ij} = A_i + A_j$, and we find that for the metal site $A_i = 0.375$ and for the As site $A_i = 1.134$. The validity of the approximation of using mean values for the force constants was shown to be accurate by calculating the model PDF for all compositions as described above and comparing to the prediction of Eq. (2) [16]. Equation (2) shows good agreement with the data for near and far neighbor PDF peaks, and for the different sublattices, over the whole alloy range, as shown in Fig. 4, using only parameters taken from fits to the end members. There is a considerably larger width associated with the As-As peak in Fig. 4 when compared to the Me-Me peak, because the As atom is surrounded by four metal cations, providing five distinct first-neighbor environments [4,5]. The theoretical curve in the lower panel of Fig. 4 is predicted to be the same for the Ga-As and the In-As bond length distribution, using the simplified approach. The Kirkwood model seems adequate to describe the experimental data at this time, although further refinement of the error bars may require the use of a better potential containing more parameters.

We would like to thank Rosa Barabash for discussions and help with the analysis of the static atom displacements, and Andrea Perez and the support staff at CHESS for help with data collection and analysis. This work was supported by DOE through Grant No. DE FG02 97ER45651. CHESS is operated by NSF through Grant No. DMR97-13424.

[1] R. W. G. Wyckoff, *Crystal Structures* (Wiley, New York, 1967), Vol. 1, 2nd ed.
[2] J. C. Mikkelson and J. B. Boyce, Phys. Rev. Lett. **49**, 1412 (1982); J. C. Mikkelsen and J. B. Boyce, Phys. Rev. B **28**, 7130 (1983).
[3] Y. Cai and M. F. Thorpe, Phys. Rev. B **46**, 15 879 (1992).
[4] J. L. Martins and A. Zunger, Phys. Rev. B **30**, 6217 (1984); M. C. Schabel and J. L. Martins, Phys. Rev. B **43**, 11 873 (1991).
[5] A. Balzarotti *et al.*, Phys. Rev. B **31**, 7526 (1985); H. Oyanagi *et al.*, Solid State Commun. **67**, 453 (1988).
[6] A. Zunger *et al.*, Phys. Rev. Lett. **65**, 353 (1990).
[7] B. E. Warren, *X-Ray Diffraction* (Dover, New York, 1990).
[8] Y. Waseda, *The Structure of Non-Crystalline Materials* (McGraw-Hill, New York, 1980).
[9] T. Egami, Mater. Trans. **31**, 163 (1990); T. Egami, in *Local Structure from Diffraction*, edited by S. J. L. Billinge and M. F. Thorpe (Plenum, New York, 1998), p. 1.
[10] I-K. Jeong, F. Mohiuddin-Jacobs, V. Petkov, and S. J. L. Billinge (unpublished).
[11] H. P. Klug and L. E. Alexander, *X-ray Diffraction Proceedures for Polycrystalline Materials* (Wiley, New York, 1974), 2nd ed.
[12] V. Petkov, J. Appl. Crystallogr. **22**, 387 (1989).
[13] Th. Proffen and S. J. L. Billinge, J. Appl. Crystallogr. **32**, 572 (1999).
[14] J. G. Kirkwood, J. Chem. Phys. **7**, 506 (1939).
[15] Jean S. Chung and M. F. Thorpe, Phys. Rev. B **55**, 1545 (1997); **59**, 4807 (1999); M. F. Thorpe *et al.*, in *Local Structure from Diffraction*, edited by S. J. L. Billinge and M. F. Thorpe (Plenum, New York, 1998), p. 157.
[16] J. S. Chung, R. I. Barabash, and M. F. Thorpe (unpublished).

Another recent application of RAD...

814 *Chem. Mater.* **2006,** *18,* 814−821

Atomic-Scale Structure of Nanocrystalline $Ba_xSr_{1-x}TiO_3$ ($x = 1, 0.5, 0$) by X-ray Diffraction and the Atomic Pair Distribution Function Technique

Valeri Petkov,*,† Milen Gateshki,† Markus Niederberger,‡ and Yang Ren§

Department of Physics, Central Michigan University, Mt. Pleasant, Michigan 48859,
Max-Planck Institute of Colloids and Interfaces, Potsdam D-14424, Germany, and
Advanced Photon Source, Argonne National Laboratory, Argonne, Illinois 60439

Received September 23, 2005. Revised Manuscript Received November 13, 2005

The atomic-scale structure of nanocrystalline $Ba_xSr_{1-x}TiO_3$ ($x = 1, 0.5, 0$) powders has been studied using high-energy X-ray diffraction, Rietveld refinement, and the atomic pair distribution function technique. The studies show that the materials are well-ordered at nanometer length distances. The three-dimensional atomic ordering in $Ba_{0.5}Sr_{0.5}TiO_3$ and $SrTiO_3$ nanopowders may well be described by a cubic structure of the perovskite type, similar to that occurring in the corresponding bulk crystals. The three-dimensional atomic ordering in $BaTiO_3$ is more complex. It is cubic-like on average, but locally shows slight distortions of a tetragonal-type. The new structural information helps one to understand better the dielectric properties of these nanomaterials.

1. Introduction

Crystalline perovskite-type oxides show many useful properties and are widely used as catalysts and in piezoelectrics and ferroelectrics.[1,2] A prime example is the family of $Ba_xSr_{1-x}TiO_3$ oxides, in particular, $BaTiO_3$. The material exists in several crystallographic modifications, each showing a particular dielectric behavior. At high temperature $BaTiO_3$ has a centrosymmetric cubic structure and is paraelectric. Between room temperature and 393 K the material possesses a tetragonal-type structure, below 278 K the structure is orthorhombic, and below 183 K it is rhombohedral.[3] Fragments of the four polymorphs occurring with $BaTiO_3$ are presented in Figure 1. The picture is characteristic of perovskites: all crystalline modifications of (Ba/Sr)TiO_3 feature a three-dimensional network of $Ti-O_6$ octahedra with Ba/Sr atoms occupying the network channels. The asymmetry of the low-temperature crystallographic modifications arises from a displacement of the Ti cations with respect to the oxygen octahedra (as depicted in Figures 1b−1d) and gives rise to spontaneous polarization. As a result, $BaTiO_3$ becomes ferroelectric below 393 K. The high permittivity of the tetragonal modification of $BaTiO_3$ and the ability to switch the direction of polarization in response to external electric fields have found application in commercially available devices such as thin film and multilayer capacitors.[4,5]

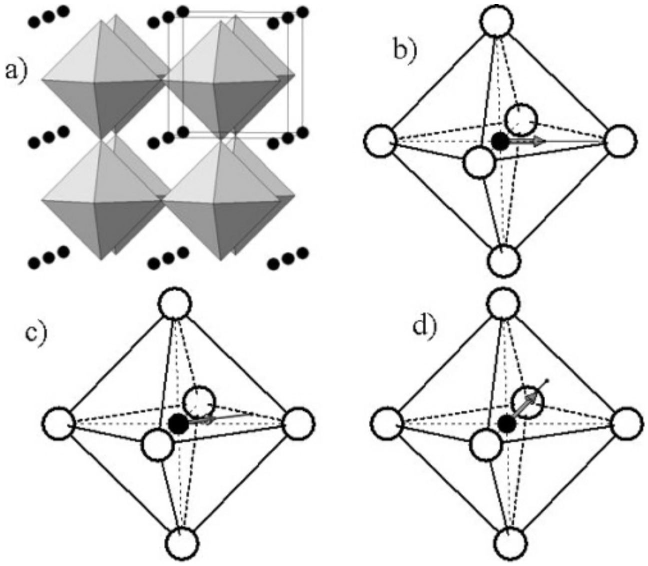

Figure 1. Fragments of the cubic- (a), tetragonal- (b), orthorhombic- (c), and rhombohedral-type (d) structures occurring with bulk $BaTiO_3$ crystals. All structure types feature a 3D network of corner-sharing $Ti-O_6$ octahedra with Ba atoms (solid circles) occupying the open space between them as shown in (a). Note the octahedral units are perfect in the cubic-type structure. The $Ti-O_6$ octahedra shown are somewhat distorted with the non-cubic-type structure types due to the off-center displacement (directions shown with arrows) of Ti atoms (solid circles at the center of the octahedra) as depicted in (b), (c), and (d). The octahedra are centered by Ti atoms (small solid circles) and coordinated by oxygens (open cicles). The unit cell in the case of the cubic-type perovskite structure is outlined with thin solid lines.

$SrTiO_3$ is a typical perovskite possessing a cubic structure (see Figure 1a) at room temperature. Although $BaTiO_3$ and $SrTiO_3$ have structures of a similar (perovskite) type, they show very different transition behavior. It is not until $SrTiO_3$ is cooled to 110 K when its cubic structure distorts and

---

[*] To whom correspondence should be addressed. E-mail: petkov@phy.cmich.edu.

[†] Central Michigan University.

[‡] Max-Planck Institute of Colloids and Interfaces.

[§] Argonne National Laboratory.

(1) Chandler, C. D.; Roger C.; Hampden-Smith, M. J. *Chem. Rev.* **1993**, *93*, 1205.

(2) Bhalla, A. S.; Gou, R.; Roy, R. *Mater. Res. Innovations* **2000**, *4*, 3.

(3) Kwei, G.; Billinge, S. J. L.; Cheong, S.-W.; Saxton, J. G. *Ferroelectrics* **1995**, *164*, 57.

(4) Hennings, D.; Klee, M.; Waser, R. *Adv. Mater.* **1991**, *3*, 334.

(5) Frey, M. H.; Payne, D. A. *Appl. Phys. Lett.* **1993**, *63*, 2753.

10.1021/cm052145g CCC: \$33.50

becomes tetragonal.[6,7] Thus, $SrTiO_3$ exhibits paraelectric behavior at room temperature, although recent studies suggest that the material is indeed an incipient ferroelectric whose ferroelectricity is suppressed by quantum fluctuations.[8]

Barium-based mixed oxides have also attracted much attention.[9] In particular, $Ba_xSr_{1-x}TiO_3$ has shown excellent dielectric properties, especially as thin films. At room temperature and low concentrations of Sr ($x < 0.5$) these mixed oxides adopt a tetragonal-type structure[10] featuring slightly distorted $Ti-O_6$ octahedra (see Figure 1b). At higher concentrations of Sr the structure is of the cubic type shown in Figure 1a.[11]

It has been discovered that many of the useful properties of perovskite materials are critically dependent on the crystallite size. For example, it has been found that at room temperature the structure of $BaTiO_3$ transforms to cubic-like when the crystallite size becomes smaller than 100 nm.[12,13] On the other hand, high-resolution synchrotron radiation studies and Raman scattering experiments have shown that fine $BaTiO_3$ powders with crystallite size as small as 40 nm show a structure with tetragonal distortions and exhibit somewhat reduced but still measurable spontaneous polarization.[14] Recently, the attention has shifted to even finer powders with crystallites as small as only a few nanometers. The reason is that having $Ba_xSr_{1-x}TiO_3$ in a nanocrystalline state is a key requirement for producing defect-free thin films.[15,16] Furthermore, nanosize powders provide good sinterability, which is an essential property for the fabrication of advanced ceramic materials.[2,4]

When in a nanocrystalline state $Ba_xSr_{1-x}TiO_3$ ceramics are non-ferroelectric, resulting in stable dielectric properties.[17,18] Several explanations for the disappearance of ferroelectricity have been put forward. They point to the absence of long-range cooperative structural distortions as one of the main reasons that could lead to a suppression of the thermodynamically stable tetragonal phase and the related to it ferroelectric behavior in nanostructured $Ba_xSr_{1-x}TiO_3$.[19] A thorough understanding of this so-called size effect and the properties of nanocrystalline barium/strontium-based materials obviously requires a detailed knowledge of their atomic-scale structure. Usually the structure of materials is determined from the Bragg peaks in their diffraction patterns. However, nanocrystalline materials lack the extended order of the usual crystals and show diffraction patterns with a pronounced diffuse component and a few broad Bragg-like features. This renders the traditional diffraction techniques for structure determination very difficult to apply. That is why structural studies on nanocrystals are scarce and the atomic arrangement in $Ba_xSr_{1-x}TiO_3$ nanopowders has not been determined in detail yet. Recently, it has been shown that the three-dimensional (3D) structure of materials with reduced structural coherence, including nanocrystals, can be determined using the so-called atomic pair distribution function (PDF) technique.[20-23] Here, we employ the traditional Rietveld and the nontraditional PDF technique to determine the 3D structure of $Ba_xSr_{1-x}TiO_3$ ($x = 1, 0.5, 0$) nanoparticles with crystallites having size as small as 5 nm. We find that these nanostructured materials possess a well-defined atomic arrangement that may be described in terms of the perovskite-type structure depicted in Figure 1. The new structural information helps one understand better the dielectric properties of the nanomaterials.

2. Experimental Section

2.1. Sample Preparation. Nanocrystalline $Ba_xSr_{1-x}TiO_3$ samples were obtained through a recently discovered approach employing a nonhydrolytic and halide-free procedure.[24] In the first step of the procedure metallic barium and/or strontium were dissolved in anhydrous benzyl alcohol at elevated temperatures (343−373 K). Generally, Sr needed a higher temperature to dissolve than Ba. The resulted solutions were mixed with 1 molar equiv of titanium isopropoxide, and the reaction mixture was transferred to a steel autoclave and heated at 574 K for 48 h. The heating took place under subsolvothermal conditions since the boiling point of benzyl alcohol is about 478 K. Representative TEM images of thus-obtained nanocrystalline materials are shown in Figures 2, 3, and 4 in ref 24. The TEM images reveal that the samples consist of individual particles with an average size of about 5 nm. Analyses based on the width of the peaks in the X-ray diffraction patterns of $Ba_xSr_{1-x}TiO_3$ performed by us yielded very similar estimates for the average nanocrystallites' size. The TEM studies also show that the nanocrystals are uniform in size and mostly spherical. No large particles or agglomerates are observed. Thus-obtained nanocrystalline $Ba_xSr_{1-x}TiO_3$ ($x = 1, 0.5, 0$) powders were loaded into glass capillaries and subjected to synchrotron radiation scattering experiments.

2.2. Synchrotron Radiation Scattering Experiments. Synchrotron radiation scattering experiments were carried out at the beamline 11-ID-C (Advanced Photon Source, Argonne National Laboratory) using X-rays of energy 115.232 keV ($\lambda = 0.1076$ Å) at room temperature. X-rays of higher energy were used to obtain diffraction data to higher values of the wave vector, Q, which is important for the success of PDF analysis ($Q_{max} = 28$ Å^{-1} with

---

(6) Lytle, F. W. *J. Appl. Phys.* **1964**, *35*, 2212.
(7) Salje, E. K.; Gallardo, M. C.; Jimenes, J.; Cerro, J. *J. Phys.: Condens. Matter* **1998**, *10*, 5535.
(8) Wang, Y. X. *Solid State Commun.* **2005**, *135*, 290.
(9) Thongrueng, J.; Nishio, K.; Watanable, Y.; Nagata, K.; Tsuchiya, T. *J. Aust. Ceram. Soc.* **2001**, *37*, 51.
(10) Josef, J.; Vimala, T. M.; Raju, J.; Murthy, V. R. K. *J. Appl. Phys.* **1999**, *32*, 1049.
(11) Liu, R. S.; Cheng, Y. C.; Chen, J. M.; Liu, R. G.; Wang, J. L.; Tsai, J. C.; Hsu, M. Y. *Mater. Lett.* **1998**, *37*, 285.
(12) Uchino, K.; Sadanaga, E.; Hirose, T. *J. Am. Ceram. Soc.* **1989**, *72*, 1151.
(13) Begg, B. D.; Vance, E. R.; Nowotny, J. *J. Am. Ceram. Soc.* **1994**, *77*, 3186.
(14) Yashimura, M.; Hoshina, T.; Ishimura, D.; Kobayashi, S.; Nakamura, W.; Tsurumi, T.; Wada, S. *J. Appl. Phys.* **2005**, *98*, 014313.
(15) Matsuda, H.; Kobayashi, N.; Kobayashi, T.; Miyazawa, K.; Kuwabara, N. *J. Non-Cryst. Solids* **2000**, *271*, 162.
(16) Zhang, J.; Yin, Z.; Zhang, M.-S. *Phys. Lett. A* **2003**, *310*, 479.
(17) Takeuchi, T.; Tabuchi, M.; Ado, K.; Honjo, K.; Nakamura, O.; Kageyama, H.; Suyama, Y.; Ohtori, N.; Nagasawa, M. *J. Mater. Sci.* **1997**, *32*, 4053.
(18) Soten, I.; Miguez, H.; Yang, S. M.; Petrov, S.; Coombs, N.; Tetreault, N.; Matsuura, N.; Ruda, H. E.; Ozin, G. *Adv. Funct. Mater.* **2002**, 12.
(19) Frey, M. H.; Payne, D. A. *Phys. Rev. B* **1996**, *54*, 3158.
(20) Toby, B. H.; Egami T. *Acta Crystallogr. A* **1992**, *48*, 336.
(21) Gateshki, M.; Hwang, S.-J.; Park, D. H.; Ren, Y.; Petkov, V. *J. Phys. Chem. B* **2004**, *108*, 14956.
(22) Billinge, S. J. L.; Kanatzidis, M. G. *Chem. Commun.* **2004**, *7*, 749.
(23) Petkov, V.; Trikalitis, P. N.; Bozin, E. S.; Billinge, S. J. L.; Vogt, T.; Kanatzidis, M. G. *J. Am. Chem. Soc.* **2002**, *124*, 10157.
(24) (a) Niederberger, M.; Pinna, N.; Polleux, J.; Antonietti, M. *Angew. Chem., Int. Ed.* **2004**, *43*, 2270. (b) Niederberger, M.; Garnweitner, G.; Pinna, N.; Antoneitti, M. *J. Am. Chem. Soc.* **2004**, *126*, 9120.

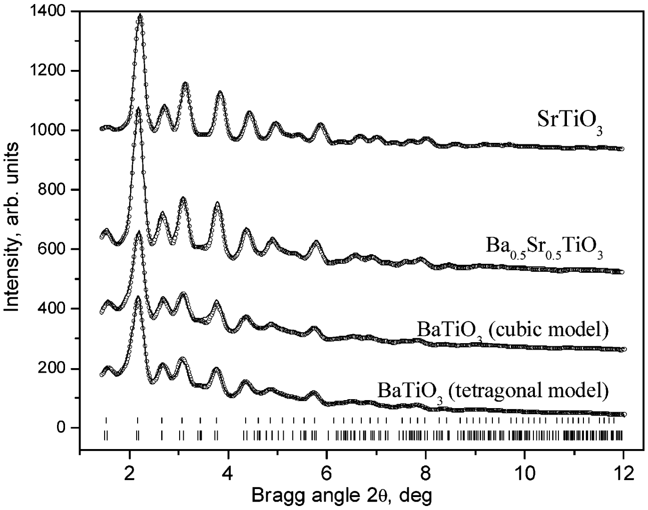

Figure 2. Experimental powder diffraction patterns for nanocrystalline $Ba_xSr_{1-x}TiO_3$ (symbols) and calculated patterns (solid lines) obtained through Rietveld refinements. The positions of the Bragg peaks of the cubic (upper set of bars) and tetragonal (lower set of bars) structures that were fitted to the diffraction pattern of $BaTiO_3$ are given in the lower part of the plot. Note the diffraction data for $SrTiO_3$ and $Ba_{0.5}Sr_{0.5}TiO_3$ are approximated with a cubic-type structure only. The corresponding goodness-of-fit factors, R_w, for each of the refinements are reported in Table 1.

the present experiments). The scattered radiation was collected with an imaging plate detector (mar345). The use of an imaging plate detector greatly reduces the data collection time and improves the statistical accuracy of the diffraction data as demonstrated by recent experiments on materials with reduced structural coherence.[25] Up to 10 images were taken for each of the samples. The exposure time was 10 s/image. The corresponding images were combined, subjected to geometrical corrections, integrated, and reduced to one-dimensional X-ray diffraction (XRD) patterns using the computer program FIT2D.[26] Thus-obtained XRD patterns for the three samples studied are presented in Figure 2.

3. Results

As can be seen in Figure 2, the experimental XRD patterns of nanocrystalline $Ba_xSr_{1-x}TiO_3$ powders show only a few broad, Bragg-like peaks that merge into a slowly oscillating diffuse component already at Bragg angles as low as 6°. As our subsequent analyses show, the diffraction patterns of $SrTiO_3$ and $Ba_{0.5}Sr_{0.5}TiO_3$ can be indexed in a cubic unit cell while that of $BaTiO_3$ can be indexed in both cubic and tetragonal unit cells of the perovsike-type structure type shown in Figure 1. Such diffraction patterns are typical for materials of limited structural coherence and are obviously difficult to be tackled by traditional techniques for structure determination. However, when reduced to the corresponding atomic PDFs, they become a structure-sensitive quantity lending itself to structure determination.

The frequently used atomic Pair Distribution Function, $G(r)$, is defined as

$$G(r) = 4\pi r[\rho(r) - \rho_0] \tag{1}$$

where $\rho(r)$ and ρ_0 are the local and average atomic number densities, respectively, and r is the radial distance. It peaks at characteristic distances separating pairs of atoms and thus reflects the atomic-scale structure. The PDF $G(r)$ is the Fourier transform of the experimentally observable total structure function, $S(Q)$, i.e.,

$$G(r) = (2/\pi)\int_{Q=0}^{Q_{\max}} Q[S(Q) - 1]\sin(Qr)\,\mathrm{d}Q \tag{2}$$

where Q is the magnitude of the wave vector ($Q = 4\pi \sin \theta/\lambda$), 2θ is the angle between the incoming and outgoing radiation beams, and λ is the wavelength of the radiation used. The structure function is related to the coherent part of the total scattered intensity as

$$S(Q) = 1 + [I^{\mathrm{coh}}(Q) - \sum c_i|f_i(Q)|^2]/|\sum c_i\, f_i(Q)|^2 \tag{3}$$

where $I^{\mathrm{coh}}(Q)$ is the coherent scattering intensity per atom in electron units and c_i and f_i are the atomic concentration and X-ray scattering factor, respectively, for the atomic species of type i.[27] As can be seen from eqs 1−3, the PDF is simply another representation of the powder XRD data. However, exploring the diffraction data in real space is advantageous, especially in the case of materials of limited structural coherence. First, as eqs 2 and 3 imply, the *total* scattering, including Bragg scattering as well as diffuse scattering, contributes to the PDF. In this way both the average, longer range atomic structure, manifested in the Bragg peaks, and the local structural distortions, manifested in the diffuse component of the diffraction pattern, are reflected in the PDF. And second, the atomic PDFs do not imply any periodicity and can be used to study the atomic ordering in materials showing any degree of structural coherence, ranging from crystals[28] to glasses[29] and even liquids.[30] Recently, the atomic PDF approach has been successfully applied to nanocrystalline materials[31−33] as well.

Experimental PDFs for the samples studied were obtained as follows. First, the coherently scattered intensities were extracted from the corresponding XRD patterns by applying appropriate corrections for flux, background, Compton scattering, and sample absorption. The intensities were normalized in absolute electron units, reduced to structure functions $Q[S(Q) - 1]$, and Fourier-transformed to atomic PDFs. Thus-obtained experimental atomic PDFs are shown in Figure 3. All data processing was done with the help of the program RAD.[34] As can be seen in Figure 3, the experimental PDFs are rich in structural features but they vanish at interatomic distances of 2−2.5 nm which are much shorter than the average size of the nanocrystals (∼5 nm).

---

(25) (a) Chupas, P. J.; Qiu, X.; Lee, P.; Grey C. P.; Billinge, S. J. L. *J. Appl. Crystallogr.* **2003**, *36*, 1342. (b) Petkov, V.; Qadir, D.; Shastri, S. D. *Solid State Commun.* **2004**, *129*, 239.

(26) Hammersley, A. P.; Hanfland, M.; Hausermann, D. *High-Pressure Res.* **1996**, *14*, 235.

(27) Klug, H. P.; Alexander, L. E. In *X-ray Diffraction Procedures for Polycrystalline Materials*; Wiley: New York, 1974.

(28) Petkov, V.; Jeong, I.-K.; Chung, J. S.; Thorpe, M. F.; Kycia, S.; Billinge, S. J. L. *Phys. Rev. Lett.* **1999**, *83*, 4089.

(29) Petkov, V.; Billinge, S. J. L.; Sashtri, S. D.; Himmel, B. *Phys. Rev. Lett.* **2000**, *85*, 3436.

(30) Petkov, V.; Yunchov, G. *J. Phys.: Condens. Matter* **1996**, *8*, 6145.

(31) Petkov, V.; Zavalij, P. Y.; Lutta, S.; Whittingham, M. S.; Parvanov, V.; Shastri, S. D. *Phys. Rev. B* **2004**, *69*, 085410.

(32) Dmowski, W.; Egami, T.; Swider-Lyons, K. E.; Love, C. T.; Rolison, D. R. *J. Phys. Chem. B* **2002**, *106*, 12677.

(33) Gateshki, M.; Petkov, V.; Williams, G.; Pradhan S. K.; Ren, Y. *Phys. Rev. B* **2005**, *71*, 224107.

(34) Petkov, V. *J. Appl. Crystallogr.* **1989**, *22*, 387.

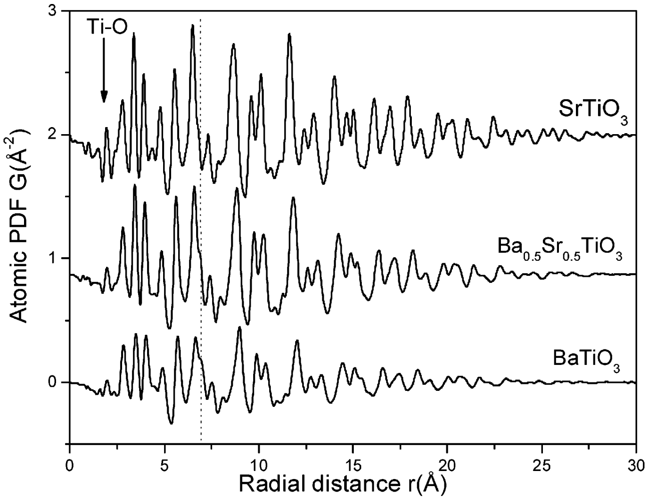

Figure 3. Experimental PDFs for nanocrystalline $Ba_xSr_{1-x}TiO_3$ extracted from the corresponding powder diffraction patterns using data extending to wave vectors as high as 28 Å^{-1}. The position of the first PDF peak, reflecting Ti−O first neighbor atomic pairs, is marked with an arrow. Note the intensity of the first PDF peak changes with the relative Sr/Ba content due to the different scattering power for X-rays of Ba and Sr. A broken line runs, as a guide to the eye, through the shoulder of the PDF peak centered at approximately 6.7 Å. The shoulder diminishes with Sr content.

Table 1. Structure Data for Nanocrystalline $Ba_xSr_{1-x}TiO_3$ (x = 1, 0.5, 0) as Obtained by the Present Rietveld and PDF Refinements[a]

	$BaTiO_3$		$Ba_{0.5}Sr_{0.5}TiO_3$		$SrTiO_3$	
	Rietveld	PDF	Rietveld	PDF	Rietveld	PDF
a, Å	4.016(6)	4.021(5)	3.985(4)	3.979(6)	3.930(3)	3.927(5)
$U_{Ba/Sr}$ (Å^2)	0.022(2)	0.009(2)	0.014(2)	0.016(2)	0.013(2)	0.009(2)
U_{Ti} (Å^2)	0.016(2)	0.015(2)	0.013(2)	0.006(2)	0.008(2)	0.010(2)
U_O (Å^2)	−0.001(2)	0.022(2)	0.001(2)	0.030(2)	0.012(2)	0.031(2)
Rw, %	2.81	25	2.37	19	2.34	18

[a] The refinements are based on the cubic-type structure presented in Figure 1a. The goodness-of-fit (Rietveld, see eq 4) and reliability (PDF, see eq 5) factors R_w are reported for each of the refinements.

This observation shows that the nanocrystalline $Ba_xSr_{1-x}TiO_3$ not only lacks the extended order of usual crystals but shows some structural distortions that further reduce their structural coherence. Such structural distortions are frequently observed with nanoparticles of sizes from 5−10 nm and are often ascribed to surface relaxation effects.[35] The distortions are more pronounced with nanocrystalline $BaTiO_3$ than with the samples containing Sr since its PDF decays to zero faster than those of the other two materials (see Figure 3). The first peak in the three experimental PDFs shown in Figure 3 is positioned at approximately 1.98(2) Å, which is close to the average Ti−O first neighbor distance observed in the corresponding crystalline bulk perovskites. The area under the peak yields 5.8(2) oxygen neighbors for each titanium atom, reflecting the presence of $Ti-O_6$ octahedral units in the nanomaterials. The peak is quite sharp and appears with almost the same shape and full-width at half-maximum (∼0.18 Å) in the PDFs for the three samples showing that they all are built of well-defined $Ti-O_6$ octahedra. Also, the three experimental PDFs exhibit a similar oscillatory behavior at longer interatomic distances, indicating that nanocrystalline $Ba_xSr_{1-x}TiO_3$ (x = 1, 0.5, 0) share common structural features, those of an extended network of $Ti-O_6$ octahedra. However, some fine but clearly noticeable differences in the experimental PDFs are also observed. For example, the peak at approximately 6.7 Å appears with a well-pronounced shoulder in the PDF for $BaTiO_3$. The same peak in the PDF for $SrTiO_3$ has no such pronounced shoulder. In general, the initial analysis of the experimental PDFs suggests that the atomic ordering in $Ba_xSr_{1-x}TiO_3$ nanopowders is likely to be of the same type but differ in some fine details for different concentrations of Ba and Sr. To reveal the fine features in the atomic ordering in nanocrystalline $Ba_xSr_{1-x}TiO_3$, we tested several structural models analyzing the experimental diffraction data both in reciprocal and real space employing the Rietveld and PDF techniques, respectively.

4. Discussion

At first, we approached the experimental XRD patterns with the widely employed Rietveld technique. The Rietveld technique[36] is used for crystal structure determination and refinement from powder diffraction data. The method employs a least-squares procedure to compare experimental Bragg intensities with those calculated from a plausible structural model. The parameters of the model are then adjusted until the best fit to the experimental diffraction data is achieved. The progress of the fit is assessed by computing various goodness-of-fit factors with the most frequently used being[37]

$$R_w = \left\{\frac{\sum w_i(y_i^{obs} - y_i^{calc})^2}{\sum w_i(y_i^{obs})^2}\right\}^{1/2} \qquad (4)$$

where y_i^{obs} and y_i^{calc} are the observed and calculated data points and w_i are weighting factors taking into account the statistical accuracy of the diffraction experiment. The Rietveld analyses were carried out with the help of the program FullProf.[38] The XRD patterns of nanocrystalline $SrTiO_3$ and $Ba_{0.5}Sr_{0.5}TiO_3$ were fit with a cubic structure of a perovskite type[39,11] that is found with the corresponding bulk crystals at room temperature. The XRD pattern of $BaTiO_3$ was approached with both the cubic and tetragonal structures (see Figures 1a and 1b) occurring with the corresponding bulk crystal. Results from the Rietveld refinements are presented in Figure 2 and the values of the refined structural parameters in Tables 1 and 2. As can be seen in Figure 2, the XRD pattern of $SrTiO_3$ and $Ba_{0.5}Sr_{0.5}TiO_3$ are very well reproduced by a model based on the cubic structure of a perovskite type shown in Figure 1a. The results show that even when in the nanocrystalline state, $SrTiO_3$ and $Ba_{0.5}Sr_{0.5}TiO_3$ adopt the structure type of the corresponding bulk crystals. The XRD pattern for nanocrystalline $BaTiO_3$ is almost equally well reproduced by the cubic and tetragonal perovskite-type structure as the data presented in Figure 2 shows. The values of the corresponding goodness-of-fit factors R_w, see Tables

---

(35) Gilbert, B.; Huang, F.; Zhang, H. Z.; Waychunas G. A.; Banfield, J. F. *Science* **2004**, *305*, 65.

(36) Rietveld, H. M. *J Appl. Crystallogr.* **1969**, *2*, 65.

(37) Young, R. A. In *The Rietveld Method*; Oxford University Press: New York, 1996.

(38) Rodríguez-Carvajal, J. *Physica B* **1993**, *192*, 55.

(39) Abramov, Y. A.; Tsirel'son, V. G.; Zavodnik, V. E.; Ivanov, S. A.; Brown, I. D. *Acta Crystallogr. B* **1983**, *39*, 942.

Table 2. Structure Data for Nanocrystalline $BaTiO_3$ as Obtained by the Present Rietveld and PDF Refinements[a]

	Rietveld	PDF
a, Å	3.987(6)	3.997(6)
c, Å	4.091(7)	4.0851(7)
z(Ti)	0.467(5)	0.470(3)
z(O1)	−0.138(5)	−0.130(7)
z(O2)	0.495(6)	0.490(3)
U_{Ba} (Å^2)	0.027(2)	0.010(2)
U_{Ti} (Å^2)	0.006(2)	0.018(2)
U_O (Å^2)	−0.020(2)	0.021(2)
R_w, %	2.47	21

[a] The refinements are based on the tetragonal-type structure presented in Figure 1b. The goodness-of-fit (Rietveld, see eq 4) and reliability (PDF, see eq 5) factors R_w are reported for each of the refinements.

1 and 2, does not allow one to draw a definitive conclusion in favor of either of the two different structure models attempted either. Moreover, the Rietveld analysis of the XRD data for the nanocrystalline $BaTiO_3$ yielded negative values for the mean-square atomic displacements of oxygen atoms (also known as thermal factors; see Tables 1 and 2). Such unphysical results are often obtained with Rietveld analyses of powder diffraction patterns for materials with considerably reduced structural coherence. The problems stem from the inability of the Rietveld analysis to handle properly diffraction patterns showing both broad Bragg peaks and pronounced diffuse scattering. As we demonstrate below, the difficulties are greatly reduced when the diffraction data are analyzed in terms of the corresponding atomic PDFs. Similarly to the Rietveld technique, the PDF technique employs a least-squares procedure to compare experimental and model data (PDF) calculated from a plausible structural model. The structural parameters of the model (unit cell constants, atomic coordinates, and thermal factors) are adjusted until the best possible fit to the experimental data is achieved. The progress of the refinement is assessed by computing a reliability factor, R_w:

$$R_w = \left\{ \frac{\sum w_i (G_i^{\text{exp.}} - G_i^{\text{calc.}})^2}{\sum w_i (G_i^{\text{exp.}})^2} \right\}^{1/2} \qquad (5)$$

where $G^{\text{exp.}}$ and $G^{\text{calc.}}$ are the experimental and calculated PDFs, respectively, and w_i are weighting factors reflecting the statistical quality of the individual data points.

Results from the PDF analyses of the experimental data for $Ba_xSr_{1-x}TiO_3$ (x = 1, 0.5, 0) in terms of the cubic structure are presented in Figures 4 , 5, and 6. Structure data from literature sources[3,40−42] were used as initial values in the PDF refinements. The PDF refinements were done with the help of the program PDFFIT.[43] To mimic the presence of limited structural disorder in the nanocrystalline materials, we multiplied the model PDF data with a decaying exponent of the type exp(−αr) as originally suggested by Ergun and later on implemented in a similar manner by Gilbert et al.[44] Typical values for α used were of the order of 0.1 Å^{-1}. The refined values of the structural parameters from the analysis are summarized in Table 1. In the case of $SrTiO_3$ and $Ba_{0.5}Sr_{0.5}TiO_3$ the PDF-based fit yielded structural parameters that are in good agreement with the present Rietveld results (see Table 1). The agreement documents well the fact that the atomic PDF provides a firm quantitative basis for structure determination. The reliability factors (defined by eq 5) also reported in Table 1 are as low (∼18%) as could be achieved with a PDF refinement.[45] These results support the findings of the Rietveld refinements that the atomic ordering in nanocrystalline $SrTiO_3$ and $Ba_{0.5}Sr_{0.5}TiO_3$ can be well-described in terms of the perovskite, cubic-type structure (space group $Pm\bar{3}m$) depicted in Figure 1a. Models based on the perovskite, tetragonal-type structure (space group $P4mm$) were also attempted with the PDF data for $SrTiO_3$ and $Ba_{0.5}Sr_{0.5}TiO_3$. These models, although having more internal degrees of freedom, did not give any significant

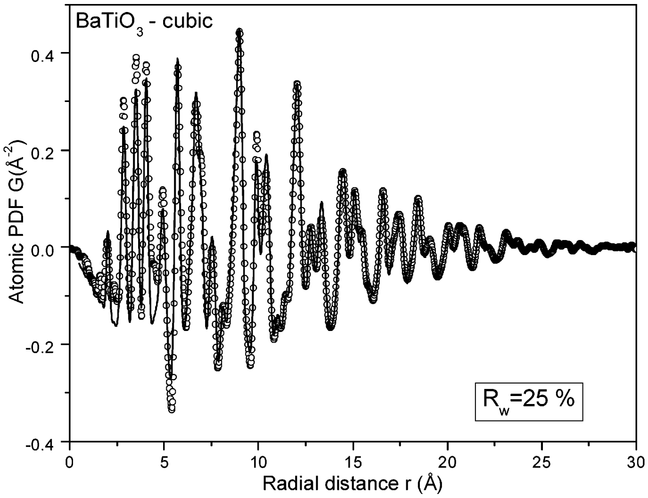

Figure 4. Experimental (symbols) and model (solid line) PDFs for $BaTiO_3$. The model PDF is based on the cubic-type structure shown in Figure 1a. The parameters of the model are given in Table 1. The reliability factor R_w is reported in the lower part of the figure.

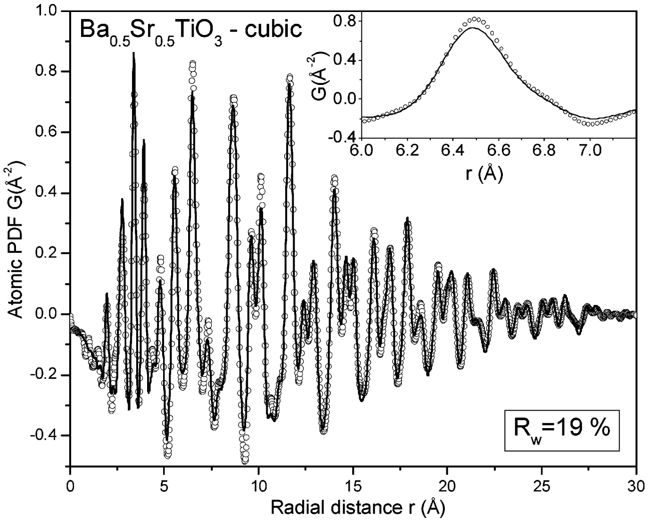

Figure 5. Experimental (symbols) and model (solid line) PDFs for $Ba_{0.5}Sr_{0.5}TiO_3$. The model PDF is based on a structure of the cubic type shown in Figure 1a. The parameters of the model are given in Table 1. The reliability factor R_w is reported in the lower part of the figure. The peak at 6.7 Å is given an enlarged scale in the inset. Its shape is well-reproduced by a cubic-type model.

---

(40) Buttner, R. H.; Maslen, E. N. *Acta Crystallogr.* **1983**, *39*, 7764.
(41) Evans, H. T. *Acta Crystallogr.* **1967**, *1*, 1948.
(42) Hewat, A. W. *Ferroelectrics* **1974**, *6*, 215.
(43) Proffen, T.; Billinge, S. J. L. *J. Appl. Crystallogr.* **1999**, *32*, 572.
(44) Ergun, S.; Schehl, R. R. *Carbon* **1973**, *11*, 127. Gilbert, B.; Huang, F.; Zhang, H. Z.; Waychunas, G. A.; Banfield, J. F. *Science* **2004**, *305*, 65.

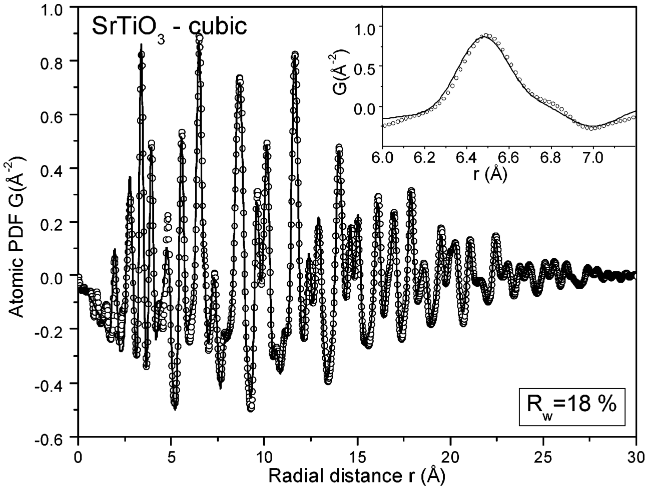

Figure 6. Experimental (symbols) and model (solid line) PDFs for $SrTiO_3$. The model PDF is based on a structure of the cubic type shown in Figure 1a. The parameters of the model are given in Table 1. The reliability factor R_w is reported in the lower part of the figure. The peak at 6.7 Å is given an enlarged scale in the inset. Its shape is well-reproduced by a cubic-type model.

improvement in the reliability factors nor in reproducing the important details in the experimental data. This observation reinforced our conclusion that nanocrystalline $SrTiO_3$ and $Ba_{0.5}Sr_{0.5}TiO_3$ studied by us possess a cubic-type structure at room temperature as their crystalline analogues do.

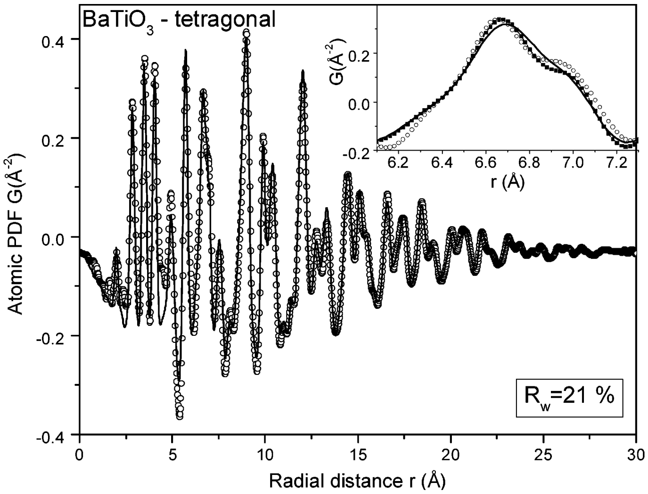

Figure 7. Experimental (symbols) and model (solid line) PDFs for $BaTiO_3$. The model PDF is based on the tetragonal-type structure shown in Figure 1b. The parameters of the model are given in Table 2. The reliability factor R_w is reported in the lower part of the figure. A portion of the experimental data (open circles) is compared to model ones based on cubic-type (solid line) and tetragonal-type structures (solid symbols) in the inset on an enlarged scale. The experimental data are better reproduced by the tetragonal-type model.

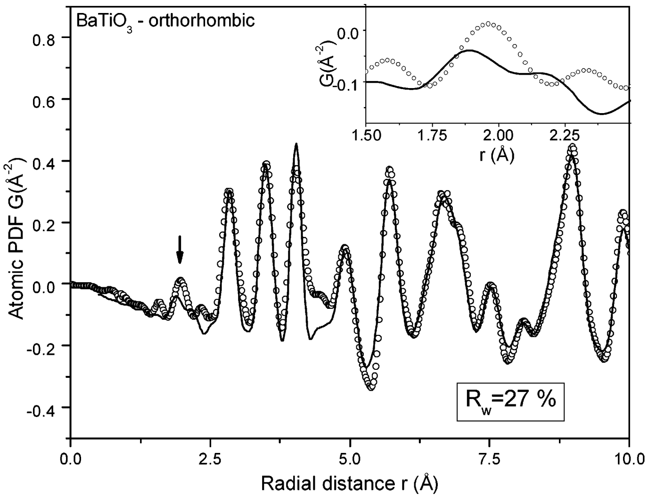

Figure 8. Experimental (symbols) and model (solid line) PDFs for $BaTiO_3$. The model PDF is based on the orthorhombic-type structure shown in Figure 1c. The reliability factor R_w is reported in the lower part of the figure. An arrow marks the position of the first PDF peak where the model and experimental data show a strong disagreement. The same peak is given in the inset on an enlarged scale.

The atomic ordering in $BaTiO_3$, however, is not so well-described in terms of the perovskite, cubic-type structure as the relatively high value (~25%, see Table 1) of the corresponding reliability factor R_w shows. That is why we attempted three more structural models based on the other three structural modifications: tetragonal (space group *P*4*mm*), orthorhombic (space group *Amm*2), and rhombohedral (space group *R*3*m*), occurring with bulk crystalline $BaTiO_3$. Results from PDF analyses of the experimental data in terms of these three structural models are presented in Figures 7, 8, and 9, respectively. As the results in Figures 8 and 9 show, the orthorhombic- and rhombohedral-type models (see Figures 1c and 1d) may be unambiguously ruled out because they feature substantially distorted Ti−O_6 octahedral units, i.e., a broad distribution of first neighbor Ti−O distances (2 Ti−O distances at 1.86 Å, two Ti−O distances of 2.0 Å, and two Ti−O distances of 2.16 Å with the orthorhombic model; three Ti−O distances of 1.87 Å and three Ti−O distances of 2.13 Å with the rhombohedral model) resulting in a split first PDF peak, a feature the experimental data do not show. On the other hand, the model based on the tetragonal-type structure considerably improves the reliability factor (compare the PDF-based R_w values reported in Tables 1 and 2 calculated over the whole range of PDF data from 1 to 28 Å) and better describes the fine features in the experimental PDF data appearing at low-*r* values, in particular, the intensity distribution of the two subcomponents of the split PDF peak at 10 Å and the position and intensity of the shoulder of the peak at 6.9 Å (see the inset in Figure 7). The shoulder reflects mostly correlations between oxygen atoms from neighboring Ti−O_6 octahedra and its pronounced presence in the PDF for $BaTiO_3$ and

---

(45) Here it may be noted that the agreement factors achieved with the PDF refinements appear somewhat higher when compared to those resulted from the Rietveld refinement of diffraction data in reciprocal space (see Tables 1 and 2). This reflects the fact that an atomic PDF differs from the corresponding XRD pattern and is a quantity much more sensitive to the local atomic ordering in materials. Furthermore, the PDF *G*(*r*) is very sensitive to the effects of imperfect data correction and systematic errors. As a result, R_w's close to 20% are common for PDF refinements even of well-crystallized materials.[21,23,31] The inherently higher absolute value of the reliability factors resulting from PDF-based refinements does not affect their functional purpose as a residuals quantity that must be minimized to find the best fit and as a quantity allowing differentiation between competing structural models. It may also be noted that when the atomic pair correlation function, *g*(*r*), defined as $g(r) = \rho(r)/\rho_0$, is used to guide a refinement of a structural model, the resulting reliability factors R_w are significantly lower than those reported from a refinement based on the corresponding PDF *G*(*r*), and very close to the values of the goodness-of-fit indicators reported from Rietveld analyses. We, however, prefer to work with the PDF *G*(*r*) and not *g*(*r*) since the former scales with the radial distance *r* (see the multiplicative factor in the definition of *G*(*r*); eq 1) and is thus more sensitive to the longer range atomic correlations.

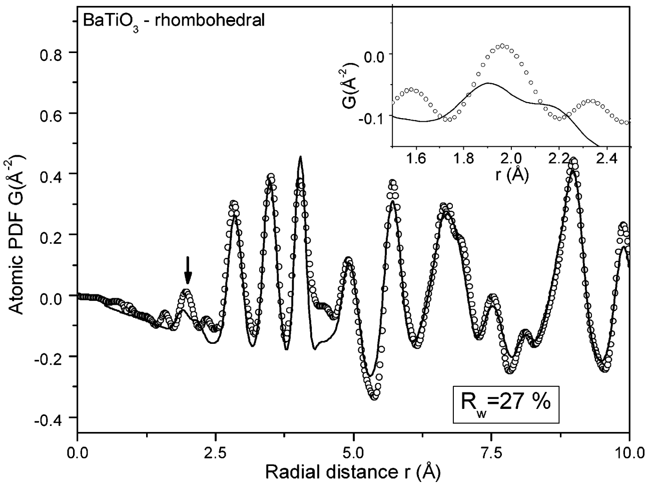

Figure 9. Experimental (symbols) and model (solid line) PDFs for $BaTiO_3$. The model PDF is based on the rhombohedral-type structure shown in Figure 1d. The reliability factor R_w is reported in the lower part of the figure. An arrow marks the position of the first PDF peak where the model and experimental data show a strong disagreement. The same peak is given in the inset on an enlarged scale.

almost disappearance in the PDFs for $SrTiO_3$ and $Ba_{05}Sr_{0.5}TiO_3$ (see Figure 3) indicates that those octahedral units are somewhat distorted/rotated in the former material and almost perfectly lined up in the materials containing Sr. The results suggest that the atomic ordering in nanocrystalline $BaTiO_3$ studied by us is likely to exhibit slight distortions similar to those occurring in bulk tetragonal $BaTiO_3$ crystal.

The tetragonal structure too features somewhat distorted Ti−O_6 octahedra (one Ti−O distance of approximately 1.9 Å, four Ti−O distances of 2.0 Å, and one Ti−O distance of 2.15 Å). The first peak in the PDF for nanocrystalline $BaTiO_3$, however, is very well reproduced by the tetragonal-based model, indicating that a model featuring slightly distorted Ti−O_6 octahedra is compatible with the experimental diffraction data. Interestingly, the tetragonal-based model is superior over the cubic one mostly at low-*r* distances (0−15 Å) as the data in Figure 10 a show. It also agrees reasonably well with the PDF data at higher *r* distances and yields a better overall reliability factor R_w (see Figure 7). A closer look at the behavior of the model data at higher *r* distances, however, shows (see Figure 10b) that the cubic-based model somewhat outperforms the tetragonal-based one as the corresponding reliability factors R_w (this time calculated over a range of real space distances from 15 to 28 Å) shows. For longer range distances the tetragonal-structure-based model does not reproduce the intensities of the experimental PDF peaks as good as the cubic-type models do and, furthermore, seems to produce a PDF that is not perfectly lined up with the experimental data for distances longer than 24 Å. The fact that the tetragonal-type model is superior over the cubic-type one mostly at distances shorter than 10−15 Å shows that the fine tetragonal distortions in nanocrystalline $BaTiO_3$ are very likely to be local in nature (up to 10−15 Å) and coexist with a cubic-type arrangement at longer range interatomic distances. The coexistence of a lower symmetry local and a higher symmetry average atomic arrangements is not an unusual picture and has even been observed with perfectly crystalline materials such as In−Ga−As semiconductors for example. These are single-phase materials possessing a long-range cubic structure and substantially distorted local atomic ordering.[29] Nanocrystalline ZrO_2 has also shown a distorted local and cubic-type, longer range atomic structure.[33] Furthermore, recent NMR studies[46] have suggested that even bulk cubic $BaTiO_3$ crystal may be viewed as an assembly of a large number of small and randomly oriented “tetragonal” nanosize domains with dynamically elongated unit cells which transform into a phase with macroscopic tetragonal structure only when cooled below 393 K. With nanocrystalline $BaTiO_3$ such a transformation of the local tetragonal-type distortions into a macroscopic tetragonal-type structure that is thermodynamically stable at room temperature may not occur because of the very limited structural coherence length (∼2 nm) in the material.

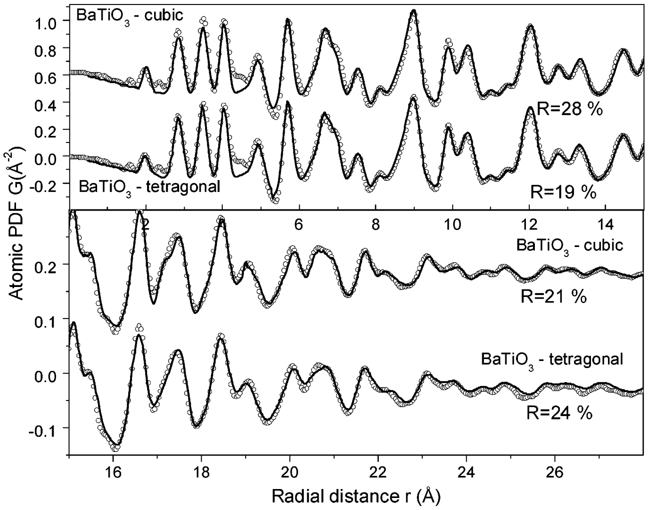

Figure 10. Low *r* (0−15 Å; upper panel) and higher *r* part (15−28 Å; lower panel) of the experimental (symbols) and model (solid line) PDFs for $BaTiO_3$. The model PDFs are based on the cubic- and tetragonal-type structures shown in Figure 1a and 1b, respectively. The corresponding structural parameters are summarized in Table 1 and Table 2, respectively. The reported in the figure reliability factors R_w are calculated over the corresponding range of distances.

In summary, the results of our structural studies show that nanocrystalline $SrTiO_3$ and $Ba_{0.5}Sr_{0.5}TiO_3$ possess a structure of a perovskite type exhibiting almost perfect Ti−O_6 units arranged in a long-range pattern with cubic symmetry. The atomic arrangement in nanocrystalline $BaTiO_3$ is also of a perovskite type but exhibits slight tetragonal distortions that show up at short-range interatomic distances only.

This new structural information helps one understand the dielectric properties of $Ba_xSr_{1-x}TiO_3$ ($x = 1, 0.5, 0$) nanoceramics as follows: The longer range cubic (centrosymmetric structures) of $SrTiO_3$ and $Ba_{0.5}Sr_{0.5}TiO_3$ are incompatible with the appearance of ferroelectricity and the materials do not show spontaneous polarization as experimentally observed.[12−16] The situation with $BaTiO_3$ is more complex. The material shows local tetragonal distortions but they seem to be confined to distances as short as 10−15 Å only. As the theoretical estimates of Lines and Glass suggest,[47] the correlation length between polar units in

---

(46) Zalar, B.; Lebar, A.; Selinger, J.; Blinc, R. *Phys. Rev. B.* **2005**, *71*, 064107.

(47) Lines, M. E.; Glass, A. M. In *Principles and Applications of Ferroelectrics and Related Materials*; Clarendon: Oxford, 1977.

ferroelectric materials are of the order of at least 10 and 2 nm in directions parallel and perpendicular to the polarization vector, respectively. With nanocrystalline $BaTiO_3$ the polar units (slightly distorted/rotated $Ti-O_6$ octahedra) are correlated over distances of about 1.5 nm only and may not become a driving force strong enough to transform the longer range structure into an asymmetric (tetragonal) one even at room temperature. As a result, the material does not show macroscopic spontaneous polarization as observed in practice.[12−16]

5. Conclusions

The atomic arrangement in nanocrystalline $Ba_xSr_{1-x}TiO_3$ (x = 1, 0.5, 0) has been studied by synchrotron radiation scattering experiments and Rietveld and atomic PDF techniques. The materials have been found to possess an atomic arrangement well-defined over 2−2.5 nm distances and resembling the one occurring in the crystalline perovskites. Although the structural coherence length in the nanostructured materials is greatly reduced, their structure still may be described in terms of a repetitive unit cell containing only a few atoms as the data summarized in Tables 1 and 2 show. $SrTiO_3$ and $Ba_{0.5}Sr_{0.5}TiO_3$ possess an atomic arrangement that is cubic type at both short and longer range interatomic distances. The local symmetry with nanocrystalline $BaTiO_3$ is tetragonal but the slight tetragonal distortions seem to average out and the structure of the material is better described in terms of a cubic-like ordering at longer range distances. That is presumably the reason nanocrystalline $BaTiO_3$, similarly to $SrTiO_3$ and $Ba_{0.5}Sr_{0.5}TiO_3$, does not show spontaneous polarization at room temperature.

This study is another demonstration of the ability of the PDF technique to yield three-dimensional structural information for materials of limited structural coherence, including nanocrystalline materials. The technique succeeds because it relies on total scattering data obtained from the material and, as a result, is sensitive to its essential structural features regardless of crystalline periodicity and size.

Acknowledgment. Thanks are due to M. Beno from APS, Argonne National Laboratory, for the help with the synchrotron experiments. The work was supported by NSF through grant DMR 0304391(NIRT). The Advanced Photon Source is supported by DOE under Contract W-31-109-Eng-38.

CM052145G